Study on *in vitro* culture model of cancer cells using magnetite nanoparticles and its applications for cancer research

磁性ナノ粒子を用いた がん細胞の *in vitro* 培養モデルとその応用研究

YAMAMOTO Shuhei

山本 修平

Department of Biotechnology, School of Engineering,

Nagoya University, Japan

名古屋大学大学院 工学研究科 化学・生物工学専攻

Contents

Chapter 1

General introduction

1.1. Cancer and the treatment approaches

Cancer, also known as a malignant tumor or malignant neoplasm, is a group of diseases involving abnormal cell growth with the potential to invade or spread to other organs of the body. Cancer is still difficult to cure, and the morbidity and mortality continue to increase in the world [1]. The incidence rates of cancer have increased during recent decades, and it caused about 8.2 million deaths which was comparable to 14.6% of all human deaths [2, 3]. Therefore, fundamental research of cancer and establishment of cancer treatment are one of important challenges in life science area.

Although many researchers have developed numerous treatment methods, including surgical resection, anticancer agent therapy, or radiotherapy, it has not still been able to cure the diseases completely [4]. As one of the main reasons, cancer invasion and metastasis have attracted much attention. They transform a locally growing tumor into a systemic, metastatic, and life-threatening disease [5]. In the metastatic process, cancer cells accumulate malignant mutations including invasiveness or drug-resistance in the primary focus, become circulating tumor cells (CTCs) by migrating out to blood vessels, spread to distant organs leading to metastatic focus [5, 6]. Almost all cancers with metastasis have poor prognosis comparing to

non-metastatic cancer. Detection or treatment of metastatic focuses is technically difficult because of its small size, while large tumors are easily detected and can be removed by surgery or radiation therapy generally [7]. Also, since the remaining CTCs after tumor removing have a high risk of recurrence [8], an exhaustive treatment with whole body administration of anti-cancer agents is most effective way to suppress metastatic tumors including CTCs. Considering to these backgrounds, there is an urgent need to clarify the fundamental mechanisms of malignant progressions in cancer cells and the clarified mechanism of malignant progressions would give the hint for design and development of novel anti-cancer agents.

1.2. Culture methods of cancer cells for cancer researches

For fundamental researches of malignant progressions in cancer cells and development of anti-cancer agents, *in vitro* two-dimensional (2D) cancer cell culture models or animal models in which cultured cancer cells are implanted *in vivo* have been commonly used to evaluate the cancer behaviors or to examine the pharmacologic responses. The 2D culture provides a well-controlled homogeneous cell environment. However, it is not representative of the *in vivo* environment, such as intercellular interactions with fibroblasts and vascular endothelial cells [9, 10] or cell-to-extracellular matrix (ECM) interactions [11, 12]. It has been reported that growth kinetics and chemosensitivity in 2D cultures differ from those in *in vivo* [13, 14], causing to delay the fundamental cancer researches and drug developments. On the other hands, although the animal models can replicate similar *in vivo* physiological conditions [15], they have inevitable problems such as the low reproducibility due to individual differences and the oversight of the unexpected side effects in human [16].

In response, *in vitro* three-dimensional (3D) cancer cell culture models are more accurate in observing the malignant behavior and evaluating chemosensitivity of cancer cells. The *in*

vitro 3D culture models can be provided by cell spheroid which has *in vivo* phenotype of tumor cells [17]. The concentration gradient of oxygen and metabolic products will be formed in cell spheroid [18-20] and it is fairly mimic to *in vivo* microenvironment.

From these features, the conventional 3D culture systems have profoundly revolutionized fundamental cancer research. However, they still have several experimental limitations. In 3D cell cultures using soft agar or ECM-mimetic gel, since cells or cell spheroids exist at random in 3 dimensions [14], they are not suitable for understanding the actual behavior of target cells or for the accurate analysis of cell dynamics or drug effects. In other 3D methods such as liquid overlay, microwell hanging drop, micropatterned agarose wells, microfluidic spheroid formation, and scaffold-based culture [21, 22] have complex cultivation procedures, leading them costly, time consuming, and low throughput. Therefore, these conventional 3D models are currently not widely used for cancer research.

To overcome these issues of conventional 3D models, 3D cellular micropatterning methods have attracted much attention to observe easily and to provide biomimetic microenvironment [23-26]. Many 3D micropatterning models have been developed using microfluidic technology. These provide useful culture models to investigate the invasive behaviors and the drug response under reproducible biochemical and biophysical microenvironments with high-resolution real-time imaging [23-26]. However, the microfluidics-based models are largely limited in single cell manipulation. In these models, the target cells are embedding in “closed” chamber and the situation obstructs the subsequent analysis. Therefore, further improvements of the 3D cellular micropatterning methods have been required.

1.3. Magnetic cell patterning method and its applications for culture model

To solve some of the problems of conventional *in vitro* 3D cell culture systems, we

developed a technique for the construction of a 3D cell array that utilizes magnetite cationic liposomes (MCLs) and a pin holder device made of soft magnetic iron [27, 28]. This model allows the distribution of cells on a planar surface in 3D using magnetic force, and can prepare multi-cellular spheroids rapidly with reproducible number of cells. The changes in behavior of the cells of interest or cell spheroids can be easily observed using a conventional phase-contrast microscope. In addition, since this model is an "open" system, the cultured spheroids in this model can be accessed easily to pick-up for the subsequent analysis. We had successfully constructed an angiogenesis model and observation model of cellular dynamics using somatic cells by this patterning method [27, 28]. Although 3D magnetic cell patterning method would be a crucial research tool for the cellular analysis, we have not applied it to evaluate cellular dynamics and drug responses of cancer cells. There are some issues for its application to anti-cancer research: i) construction of *in vitro* culture environment to observe malignant behavior of cancer cells, ii) development of a high-throughput method to evaluate anti-proliferative effects of anti-cancer treatment, iii) construction of co-culture model to evaluate the malignant interaction of cancer cells with somatic cells, and iv) development of a high-throughput evaluation method for cancer invasive behavior.

1.4. Aim of this thesis

In this thesis, I aimed to construct an *in vitro* 3D bio-mimetic culture model of cancer cells by a magnetic cell patterning method to solve the issues as mentioned above, and to evaluate its potentials for applications to anti-cancer research.

In the **Chapter 2**, 3D spheroids culture arrays using melanoma cell were developed to construct the culture environment, and to evaluate the combined effect of a melanogenesis-targeting drug (NPrCAP) and heat treatment, as models of anti-cancer treatment. As a result, melanoma cells showed spheroid formation and enhanced melanin

production, which has *in vivo* phenotype of melanin cells, in 3D spheroids culture arrays. In addition, I confirmed that the spheroid size was linearly correlated with the cell number within a spheroid to construct a rapid and non-destructive evaluation method of these anti-proliferative effects.

In the **Chapter 3 and 4**, 3D co-culture models of cancer with stromal cells were developed to evaluate the interaction among these cells using the 3D culture environment in Chapter 2. In the **Chapter 3**, 3D co-culture arrays of melanoma cell spheroids and stromal fibroblasts were constructed to analyze the interaction of fibroblast on the invasive capacity of melanoma. The effect on the invasion of melanoma was investigated using three types of cell interaction models: (i) fibroblasts were patterned together in array with melanoma spheroids (direct-interaction model), (ii) fibroblasts coexisting in the upper space (indirect-interaction model) of melanoma spheroids, and (iii) a fibroblast layer coexisting under melanoma spheroids (fibroblast-sheet model).

In the **Chapter 4**, 3D co-culture arrays of invasive melanoma cell spheroids were developed to evaluate the invasive capacity of melanoma cells to co-cultured vascular-formed endothelial cell network. I found the spatial interaction of the network on melanoma invasion using this co-culture model, and compared its malignant behavior than that of fibroblast. Also, I confirmed that the spheroid length and perimeter were correlated with the cell invasiveness to construct a non-destructive and automatic evaluation method of these malignant invasions.

In the **Chapter 5 and 6**, to apply our culture method using MCL for preclinical cancer sample, I aimed to develop an *ex vivo* culture method of CTCs, and analyzed the malignant phenotypes. In the **Chapter 5**, to isolate CTCs rapidly and efficiently, I constructed the combined method of a size-selective capture filter and a magnetic capture column which captured magnetically labeled with MCLs. Also, I evaluated its capturing performance at a high flow rate to reduce the capturing time from large volumes of blood containing CTCs.

In the **Chapter 6**, I developed an *ex vivo* culture method of CTCs using a fibroblast-sheet model (Chapter 3) as a feeder to perform the phenotype-based analysis. I isolated CTCs by the combined method shown in Chapter 5 from the blood of metastatic model mice, and obtained three CTC-derived cells. Then, I analyzed malignant-related phenotypes, proliferative, invasive- and drug resistant-abilities.

1.5. References

1. Ho WJ, Pham EA, Kim JW, *et al*. Incorporation of multicellular spheroids into 3-D polymeric scaffolds provides an improved tumor model for screening anticancer drugs. Cancer Sci 101:2637-2643, 2010.
2. World Cancer Report 2014. World Health Organization. ISBN 9283204298, Chapter 1.1, 2014.
3. The top 10 causes of death Fact sheet N°310". WHO, 2014.
4. Yang W, Zou L, Huang C, *et al*. Redox regulation of cancer metastasis: molecular signaling and therapeutic opportunities. Drug Dev Res 75: 331-341, 2014.
5. Friedl P, Alexander S. Cancer invasion and the microenvironment: Plasticity and reciprocity. Cell 147: 992-1009, 2011.
6. Quigley JP, Armstrong PB. Tumor cell intravasation alucidated: The chick embryo opens the window. Cell 94: 281-284, 1998.
7. Tilki D, Hu B, Nguyen HG, *et al*. Impact of synchronous metastasis distribution on cancer specific survival in renal cell carcinoma after radical nephrectomy with tumor thrombectomy. J Urol 193: 436-442, 2015.
8. Zhang Y, Shi ZL, Yang X, *et al*. Targeting of circulating hepatocellular carcinoma cells to prevent postoperative recurrence and metastasis. World J Gastroenterol 20: 142-147, 2014.
9. Wang YH, Dong YY, Wang WM, *et al*. Vascular endothelial cells facilitated HCC invasion and metastasis through the Akt and NF-κB pathways induced by paracrine cytokines. J Exp Clin Cancer Res 32: 51, 2013.
10. Bäuerle T, Komljenovic D, Berger MR, *et al*. Multi-modal imaging of angiogenesis in a nude rat model of breast cancer bone metastasis using magnetic resonance imaging, volumetric computed tomography and ultrasound. J Vis Exp 14: e4178, 2012.

11. Birgersdotter A, Sandberg R, Ernberg I. Gene expression perturbation *in vitro*—a growing case for three-dimensional (3D) culture systems. Seminars in Cancer Biology 15: 405-412, 2005.
12. Petersen OW, R´ønnov-Jessen L, Howlett AR, *et al*. Interaction with basement membrane serves to rapidly distinguish growth and differentiation pattern of normal and malignant human breast epithelial cells. Proc Natl Acad Sci USA 89: 9064-9068, 1992.
13. Ohmori T, Yang JL, Price JO, *et al*. Blockade of tumour cell transforming growth factor-betas enhances cell cycle progression and sensitizes human breast carcinoma cells to cytotoxic chemotherapy. Exp Cell Res 245: 350-359, 1998.
14. Flach EH, Rebecca VW, Herlyn M, *et al*. Fibroblasts contribute to melanoma tumor growth and drug resistance. Mol Pharmaceutics 8:2039-2049, 2011.
15. Al-Mehdi AB, Tozawa K, Fisher AB, *et al*. Intravascular origin of metastasis from the proliferation of endothelium-attached tumor cells: a new model for metastasis. Nat Med 6: 100-102, 2000.
16. Bersini S, Jeon JS, Dubini G, *et al*. A microfluidic 3D *in vitro* model for specificity of breast cancer metastasis to bone. Biomaterials 35: 2454-2461, 2014.
17. Becker JL, Prewett TL, Spaulding GF, *et al*. Three dimensional growth and differentiation of ovarian tumor cell line in high aspect rotating-wall vessel: morphologic and embryologic considerations. J Cell Biochem 51: 283-289, 1993.
18. Håkanso M, Textor M, Charnley M. Engineered 3D environments to elucidate the effect of environmental parameters on drug response in cancer. Integr Biol 3: 31-38, 2011.
19. Sodunke TR, Turner KK, Caldwell SA, *et al*. Micropatterns of Matrigel for three-dimensional epithelial cultures. Biomaterials 28: 4006-4016, 2007.
20. Fukuda J, Khademhosseini A, Yeo Y, *et al*. Micromolding of photocrosslinkable chitosan hydrogel for spheroid microarray and co-cultures. Biomaterials 27: 5259-5267, 2006.

21. Kim JB. Three-dimensional tissue culture models in cancer biology. Cancer Biol 15: 365-377, 2005.
22. Gallagher PG, Bao Y, Prorock A, *et al*. Gene expression profiling reveals cross-talk between melanoma and fibroblasts: implications for host-tumor interactions in metastasis. Cancer Res 65: 4134-4146, 2005.
23. Wu LY, Di Carlo D, Lee LP. Microfluidic self-assembly of tumor spheroids for anticancer drug discovery. Biomed Microdevices 10: 197-202.
24. Aref AR, Huang RY, Yu W, *et al*. Screening therapeutic EMT blocking agents in a three-dimensional microenvironment. Integr Biol 5: 381-389, 2013.
25. Shin MK, Kim SK, Jung H. Integration of intra- and extravasation in one cell-based microfluidic chip for the study of cancer metastasis. Lab Chip 11: 3880-3887, 2011.
26. Kim BJ, Hannanta-anan P, Chau M, *et al*. Cooperative roles of SDF-1a and EGF gradients on tumor cell migration revealed by a robust 3D microfluidic model. Pros One 8: e68422, 2013.
27. Ino K, Okochi M, Konishi N, *et al*. Cell culture arrays using magnetic force-based cell patterning for dynamic single cell analysis. Lab Chip 8: 134-142, 2008.
28. Ino K, Okochi M, Honda H. Application of magnetic force-based cell patterning for controlling cell-cell interactions in angiogenesis. Biotechnol Bioeng 102: 882-890, 2009.

Chapter 2

Three-dimensional magnetic cell array for evaluation of anti-proliferative effects of chemo-thermo treatment on cancer spheroids

2.1. Introduction

In vitro cellular assay models are gaining momentum as powerful tools to study cellular events for medical applications and tissue engineering. In the field of cancer therapy, discovery of key factors that affect cancer proliferation and malignancy is easier using *in vitro* cellular assay models compared with *in vivo* models. Traditional two-dimensional (2D) monolayer culture models provide a well-controlled homogeneous culture environment. However, 2D culture is not representative of the *in vivo* environment such as the formation of cell spheroids via intercellular and cell-extracellular matrix (ECM) interactions [1, 2]. Because these interactions can lead to drug resistance in cancer cells [3, 4], 2D culture is not suitable to evaluate the effects of drug treatments on cancer cells.

In vitro three-dimensional (3D) culture platforms, in which cells are placed randomly in an ECM-mimetic gel, can support cell spheroid formation and the distribution of oxygen and metabolic products [5, 6]. However, accurate visualization of cell dynamics and drug

responses in target cells in real-time is difficult in such models [7, 8]. Although invasive procedures using 3D microfluidic models have been developed to facilitate visualization, these procedures are largely limited to counting methods for cells within spheroids to evaluate the anti-proliferative effects of drugs on target cells enclosed within a chamber [9]. Additionally, these types of counting methods are inherently destructive to the cells and lead to a decrease in drug-screening throughput. Therefore, biomimetic cell culture models are needed for analysis of drug responses and anti-cancer drug screening, which facilitate visualization of drug responses in cells and allow evaluation of anti-proliferative effects easily and non-destructively.

The 3D cellular micropatterning method provides useful model systems to investigate the response of target cells to drugs under a combination of multiple controllable biochemical and biophysical microenvironments, together with high-resolution real-time imaging. To provide an effective and practical technique, we developed a 3D cell spheroid culture array (3D array) using a magnetic force and magnetic cationic liposomes (MCLs) containing magnetite nanoparticles [10-12]. MCLs have been used for magnetic cell labeling via electrostatic interactions between the positively charged liposomes and target cell membrane. Magnetite content in magnetically labeled cells can be as high as 100 pg magnetite/cell [13], corresponding to one million particles per cell. An advantage of this labeling method is that magnetically labeled cells can be arranged to promote rapid formation of multicellular spheroids [14]. In addition, labeling cells with MCLs has little effect on cell viability, growth, and differentiation [15, 16]. Using a pin-holder device, the magnetic field of a neodymium magnet is concentrated at the head of each pin, thus allowing allocation of a specific number of cells in a planar fashion according to the seeding density in the ECM. This method has the benefits of both conventional 3D and 2D cell culture methods, such as the ability to observe cell dynamics and allowing single cell manipulation to evaluate gene expression in target

cells [10]. Recently, 3D arrays were successfully used to demonstrate the ability of an anti-cancer drug to inhibit the invasive capacity of cancer cells, which was evaluated based on cell elongation within the 3D ECM [15]. Therefore, 3D arrays have potential as an experimental model to analyze cellular dynamics and evaluate anti-cancer drugs.

Among the various forms of neoplasms, melanoma is one of the most malignant tumors, is difficult to treat, and continues to have poor prognoses, leading to increases in morbidity and mortality [17]. Melanoma cells possess a unique biosynthetic pathway (melanogenesis) located in specialized cytoplasmic organelles called melanosomes where tyrosinase catalyzes the oxidative conversion of L-tyrosine via dopaquinone into melanin pigments [18]. The sulfur-amine analog of tyrosine, N-propionyl-4-cysteaminylphenol (NPrCAP), is a tyrosinase substrate and melanoma-specific targeting drug that has been shown to induce selective cytotoxicity in melanocytes and melanoma cells [19, 20]. NPrCAP has both cytostatic and cytocidal effects on melanomas *in vitro* and *in vivo* owing to the production of cytotoxic N-propyl-4-S-cysteaminyl-1,2-benzoquinone (NPrCAQ), which results in oxidative stress and the generation of cytotoxic free radicals such as hydroxyl radicals [21-25]. Therefore, NPrCAP is an attractive candidate to study anti-melanoma chemotherapies.

The exploitation of biological properties unique to melanoma cells may provide a novel approach to improve the efficacy of hyperthermia cancer therapy [26]. The hyperthermia generated by alternating magnetic fields with magnetite nanoparticles as heating mediators appears to be a promising method that specifically heats tumors without damaging surrounding healthy tissue [27, 28]. We previously evaluated a melanoma-targeting therapy by conjugating NPrCAP and MCLs, which produced intracellular hyperthermia *in vivo* [29-31], suggesting that an anti-cancer drug coupled with hyperthermia may provide a novel cancer treatment. However, there are no reports of *in vitro* evaluation models that can quantify the combined effect of chemical and physical treatments such as NPrCAP coupled

with hyperthermic treatment based on melanoma proliferation in a biomimetic environment.

In the present study, we aimed to construct an *in vitro* evaluation model to examine the sensitivity to chemical treatment coupled with heat treatment in melanoma cells based on their proliferation in a 3D array using a magnetic cell-patterning method. Although it is important that screening models are able to evaluate anti-proliferative effects on cancer cells, we have not applied our magnetic 3D array to evaluate the effect of anti-cancer treatment based on cancer cell proliferation. The mouse melanoma cell line B16F1 was used as a model cancer cell, and NPrCAP coupled with heat treatment (42°C for 1 h) was used as a model of anti-cancer treatment. A 3D magnetic cell-patterning method was used to form arrays of magnetically labeled B16F1 cell spheroids in type I collagen gels. The interaction between type I collagen and melanoma cells enhances melanogenesis in 3D culture *in vitro* as well as *in vivo* [32, 33], and intercellular adhesion and cell-ECM interactions lead to drug resistance of the cells [3, 4]. The evaluation model with these interactions would be suitable to evaluate the anti-proliferative effects of a melanogenesis-targeting anti-cancer agent such as NPrCAP. Importantly, we evaluated the proliferation of B16F1 cells within spheroids in 3D arrays based on the spheroid size. Considering the ability to perform drug and physical assays of malignant cancer cells in a simple and non-destructive manner, this system provides a promising approach for effective screening of combined chemical and physical cancer therapy.

2.2. Materials and methods

2.2.1 Cell culture in 2D monolayers

The mouse melanoma cell line B16F1 (CRL-6323; ATCC, Manassas, VA, USA) was cultured on 10-cm dishes in high-glucose Dulbecco's Modified Eagle's Medium (DMEM; Invitrogen, Gaithersburg, MD, USA) supplemented with 10% fetal bovine serum (Invitrogen),

0.1 μg/mL streptomycin sulfate, and 100 U/mL potassium penicillin G (Invitrogen) at 37°C in a humidified atmosphere containing 5% CO_2.

2.2.2. Preparation of MCLs and the pin-holder device

MCLs were prepared and the pin-holder device was constructed as described previously [10] using magnetite nanoparticles (Fe_3O_4, mean diameter: 10 nm; Toda Kogyo Co., Hiroshima, Japan) and a lipid mixture of N-(a-trimethylammonioacetyl) didodecyl-D-glutamate chloride (TMAG), dilauroyl phosphatidylcholine (DLPC), and dioleoylphosphatidylethanolamine (DOPE) at a molar ratio of 1:2:2. For magnetic labeling, B16F1 cells were cultured to sub-confluence. The medium was then replaced with fresh medium containing finely dispersed MCLs at a final concentration of 100 pg magnetite per cell. After 2 h of incubation with MCLs, the cells were washed to remove residual MCLs. The magnetically labeled cells were harvested using 0.25% trypsin ethylenediaminetetraacetic acid (EDTA) (Life Technologies, Carlsbad, CA, USA).

The pin-holder device was fabricated to allocate magnetically labeled cells by the profile of their magnetic distribution [10] The device has a base of magnetic soft iron, measuring 20 mm wide × 20 mm long × 10 mm high. A wire electrical discharge machine (DIAX-FX10; Mitsubishi Electric Co., Tokyo, Japan) was used with a cutting wire (diameter: 0.1 mm; Sumitomo Electric Industries, Osaka, Japan) to construct the array of square-pole type pillars with dimensions of 100 μm wide × 100 μm long × 320 μm high at intervals of 150 μm with center-to-center spacing of 250 μm or at intervals of 900 μm with center-to-center spacing of 1000 μm. The magnetic field was concentrated on the pillars using an external neodymium disc magnet (50 mm in diameter and 10 mm in height with a surface magnetic induction of 0.38 T; Niruko Factories Co., Shiga, Japan).

2.2.3. Preparation of B16F1 melanoma spheroid 3D culture arrays

3D arrays were constructed as reported previously [10]. A 0.21% type I collagen mixture was prepared by mixing a 7:2:1 volumetric ratio of ice-cold collagen solution, 0.3% Cellmatrix Type I-A (Nitta Gelatin, Osaka, Japan) with 5× DMEM, and 10× sterile reconstitution buffer (2.2 g $NaHCO_3$ in 100 mL of 0.05 M NaOH and 0.2 nM 2-[4-(2-hydroxyethyl)-1-piperazinyl]ethane sulfonic acid). A gas-permeable tissue culture dish (35 mm, hydrophilic lumox dish; Sarstedt, Nümbrecht-Rommelsdorf, Germany) was thinly covered with 50 μL of the collagen gel using a cell scraper. After the pin-holder device was mounted on the neodymium disc magnet, the collagen-coated culture dish was placed on the pin holder and magnet. Magnetically labeled cells (7.2×10^4 cells/mL, 2.5 mL, average 7 cells/spot) were seeded into the dish and incubated at 37°C for 30 min. After formation of the cell array, 1 mL of the 0.21% collagen mixture was pipetted over the array. The dish was then removed from the pin-holder device and magnet, and incubated at 37°C for 30 min. After solidification of the collagen, 1 mL DMEM containing NPrCAP was added to the cell array. Final concentrations of NPrCAP were 0.1-5 mM.

2.2.4. Melanin assay

Melanin secreted from B16F1 melanoma cells was measured in the supernatants of 2D and 3D array cultures. Aliquots of culture supernatants (500 μL) were collected from 2D and 3D array cultures during 5 days of cultivation. Melanin was measured based on the absorbance at 405 nm using a standard curve generated from serial dilutions of synthetic melanin (Wako Pure Chemical Industries, Osaka, Japan) in 2 N NaOH. Melanin production is expressed as ng per cell. To evaluate the effect of NPrCAP on melanin production, B16F1 cells were cultured in a 3D array with 0.1 mM NPrCAP. NPrCAP was prepared as described previously [19]. The culture supernatant was sampled after 3 days of cultivation, and melanin

production was assessed as described above.

Viable cells in 2D cultures were identified by the trypan blue exclusion method, and cell counting was performed using a hemocytometer. To determine the number of viable cells in 3D arrays, the cells were treated with 0.24% collagenase, washed in PBS, and then counted by the trypan blue exclusion method.

2.2.5. Combined NPrCAP and heat treatment of 2D and 3D array cultures

For 2D cultures, B16F1 cells were seeded in 24-well plates at a density of 3.6×10^4 cells/well with 1 mL medium containing NPrCAP at concentrations ranging from 0.1 to 5 mM. For 3D array cultures, 1 mL medium containing NPrCAP was added to magnetically patterned cell arrays after collagen solidification. Following the addition of NPrCAP, heat treatment was applied to the cultures using a temperature-controlled water bath. Briefly, the cells were heated at 42°C for 60 min by directly immersing the cell culture dishes in the water bath. The temperature of the medium increased rapidly and reached the intended temperature within 5 min. The temperature of the medium was monitored using a fiber optic thermometer probe (FX-9020; Anritsu Meter, Tokyo, Japan). After heat treatment, the cells were placed in an incubator at 37°C, and the effect of NPrCAP and heat treatment on cell proliferation was determined after 3 days of culture.

2.2.6. Measurement of B16F1 cell proliferation within spheroids in 3D arrays based on the spheroid size

To evaluate the anti-proliferative effect of NPrCAP and heat treatment on the cell spheroids in 3D arrays, we performed time-lapse monitoring using phase-contrast microscopy (Model IX81; Olympus, Tokyo, Japan) during 8 days of culture. The areas of each cell spheroid were measured in phase-contrast images using image analysis software

(MetaMorph; Universal Imaging, Downingtown, PA, USA). In addition, we generated a standard curve from the spheroid areas and average cell number within spheroids, which was counted after collagenase digestion of the collagen gel by trypan blue exclusion every 2 days to evaluate the relationship between cell proliferation within a spheroid and the spheroid area.

2.2.7. Evaluation of the combined treatment

The effect of combined treatment on 2D and 3D array cultures was calculated using Valeriote's method [34] as follows.

The relative number of 2D cells (%) = (number of experimental cells/number of control cells) × 100. Relative number of 3D cells (%) = (area of experimental cell spheroids/area of control cell spheroids) × 100.

The effects of NPrCAP plus heat treatment were defined as follows: synergistic, [*A*+*B*] < [*C*]; additive, [*A*+*B*] ≒ [*C*]; subadditive, [*C*] < [*A*+*B*] < [*A*] or [*C*] < [*A*+*B*] < [*B*]; interference, [*B*] > [*A*+*B*] > [*A*]; where [*A*], [*B*], and [*A*+*B*] were relative cell numbers in the case of heat treatment alone, NPrCAP treatment alone, and the combination, respectively. [*C*] = ([*A*]×[*B*]/100), which is the expected relative cell number or relative spheroid size in the case of the combination.

2.3. Results

2.3.1 Cultivation of melanoma cells in 3D array cultures using a magnetic pin-holder device

To observe the morphological behavior of B16F1 melanoma cells in 3D arrays, magnetic

labeling and patterning was conducted using MCLs and the magnetic pin-holder device in type I collagen. **Fig. 2-1** shows phase-contrast photomicrographs of magnetically labeled B16F1 melanoma cells in 2D and 3D array cultures. Changes in B16F1 cell growth were not observed in cultures with or without MCL labeling (data not shown). Spindle-shaped cell morphology was observed in 2D cultures with little production of melanin (**Fig. 2-1A, 2-1B**). In contrast, cells in 3D arrays formed spheroids via intercellular adhesion after 1 day of culture (**Fig. 2-1D**). The size of the spheroids increased continuously during culture (**Fig. 2-1E, 2-1F**). All spheroids were allocated in a planar fashion on the grid, which corresponded to the top of the pin, allowing simultaneous observation of target cell behavior under a conventional microscope. The B16F1 cells proliferated within spheroids, and the spheroids became black as a result of melanin production (**Fig. 2-1E, 2-1F**).

Next, because melanin production was accelerated in 3D array cultures, we measured the amount of melanin in the supernatants of 2D and 3D array cultures. **Fig. 2-2** shows images of the harvested culture supernatants (**Fig. 2-2A**-**2-2D**) and melanin production (**Fig. 2-2E, 2-2F**). The supernatants of 3D array cultures were darker (**Fig. 2-2C**) than those of 2D cultures (**Fig. 2-2B**), and the concentration of melanin in the culture supernatants was significantly higher in 3D array cultures compared with 2D cultures (**Fig. 2-2E**). The concentration of melanin in the 3D array on day 3 of incubation was 29-fold higher (2.12 ng/cell) than that in the 2D culture (0.073 ng/cell). The addition of NPrCAP as a melanogenesis inhibitor to B16F1 cells in 3D array cultures led to a decrease in the production of melanin (0.41 ng/cell, **Fig. 2-2D, 2-2F**), suggesting that the black spheroids and supernatants of 3D array cultures were caused by accelerated melanogenesis.

2.3.2 Evaluation of cell proliferation within a spheroid based on the spheroid area

Because the size of B16F1 spheroids in 3D arrays had increased continuously during

culture, we evaluated the proliferation of B16F1 cells within spheroids in a non-destructive manner. To evaluate the correlation between the cell number within a spheroid and the spheroid size, we obtained phase-contrast images of B16F1 spheroids at various time points during culture (0-8 days), and calculated the spheroid areas in the images using image analysis software. The areas of the spheroids were then compared with the average cell numbers including spheroids from 3D arrays, which were counted after collagenase digestion every 2 days during the 8 days of culture. The average cell number was defined as the total cell number in a culture dish divided by the total spheroid number (6400 spheroids).

The B16F1 cells had proliferated from 7 to 100 cells/spheroid in 3D arrays during 8 days of culture (data not shown), and the spheroid area was correlated linearly with the cell number within a spheroid (**Fig. 2-3**). These data suggest that the proliferation of B16F1 cells within spheroids can be non-destructively evaluated based on the spheroid area.

2.3.3 Evaluation of the combined effect of NPrCAP and heat treatments on melanoma cells

To assess the combined effect of NPrCAP and heat treatments on B16F1 spheroids, we compared the proliferation of B16F1 cells with or without heat treatment at various concentrations of NPrCAP. **Fig. 2-4** shows the morphological changes and growth curves of B16F1 cells that were treated with NPrCAP and heat in 2D cultures (**Fig. 2-4A, 2-4B**) and 3D array cultures (**Fig. 2-4C, 2-4D**). The cell numbers in 3D arrays were calculated from photomicrographs using the spheroid size-cell number correlation (**Fig. 2-4**). The vertical axis in **Figs. 2-4B and 2-4D** shows the relative cell numbers compared with the untreated group. **Fig. 2-4E** shows the half-maximal inhibitory concentrations (IC_{50}s) of NPrCAP with or without heat treatment in 2D and 3D array cultures, which were calculated from **Figs. 2-4B and 2-4D**.

As shown in **Fig. 2-4A-2-4D**, NPrCAP exerted a dose-dependent anti-proliferative effect on both 2D and 3D array cultures. The B16F1 cells in 3D array cultures showed an approximately 2-fold higher IC_{50} than those in 2D culture (**Fig. 2-4**). The IC_{50}s of heat-treated groups were almost 40% lower than those of unheated groups. **Table 2-1** summarizes the combined effects of NPrCAP and heat treatments, which were determined using Valeriote's method [34]. An additive effect was observed for these treatments. Furthermore, heat treatment and the pharmacologic activity of NPrCAP were independent.

2.4. Discussion

In the present study, we developed a 3D cellular assay model based on the proliferation of melanoma cells in a 3D array using magnetic cell assembly, and demonstrated its applicability to evaluate the combined effect of the melanoma-targeting drug NPrCAP and heat treatment. The developed model allowed evaluation of cellular proliferation within spheroids in a non-destructive and continuous manner. The spheroid area in phase-contrast images was linearly correlated with the number of mouse B16F1 melanoma, human GCIY gastric cancer, and human MDA-MB-231 breast cancer cells in the spheroid (**Fig. 2-3 and Fig. 2-5**). The magnetic cell patterning method could allocate a specific number of magnetically labeled cells (average 7 cells/spot, 3-9 cells/spot at a seeding density of 7.2×10^4 cells/mL). Because the ratio of the spheroid area and standard deviation value shown in **Fig. 2-3** decreased according to the culture time (data not shown), the cell allocation had a small effect on the spheroid area compared with the effects of proliferation within the spheroid. In conventional 3D culture assays, non-destructive and continuous visualization and evaluation of target cell proliferation within a spheroid are difficult, which are some of the reasons why these assays have not been widely used for drug screening [8, 9]. Therefore, the developed model in which cell proliferation was evaluated based on spheroid area in

phase-contrast images may be a powerful tool for drug screening.

In the field of cancer therapies, metastasis is a hallmark that transforms a locally growing tumor into a systematic and life-threatening disease [35], and *in vitro* 3D culture models using cellular micropatterning techniques provide useful assays to discover key factors that affect cell invasion and screen anti-metastasis drugs. Previously, we investigated the anti-invasive effects of genistein (5,7,40-trihydroxyisoflavone), which is a natural tyrosine kinase inhibitor isolated from soy beans, on invasive cells in a 3D array [15]. However, we only evaluated the invasive capacity based on morphological changes as determined by the spheroid area in phase-contrast images. We did not evaluate the anti-proliferative or cytocidal effects of genistein within spheroids using viability tests. The non-invasive method to evaluate cancer cell proliferation developed in the present study could be applied to various types of cancer cells with different invasive potentials (**Fig. 2-5**). Measuring the area in phase-contrast images does not indicate dead cells in spheroids. However, by applying live-dead staining with confocal analysis, our 3D array could allow evaluation of both the cytocidal and anti-proliferative effects of anti-cancer agents on chemotactic invasive cancer cells. For example, an *in vitro* intravasation model could be evaluated during metastasis using 3D spatial information. Thus, the 3D array in combination with our evaluation method would be suitable to analyze both cancer cell invasion and proliferation in the anti-cancer drug assay.

The melanin production of B16F1 cells and IC_{50} of NPrCAP were higher in 3D arrays than in 2D cultures (**Figs. 2-1, 2-2, and 2-4**). Several studies have reported that mouse melanoma cell lines exhibit accelerated melanin production in both *in vitro* 3D culture [32] and *in vivo* [33] via intercellular and cell-ECM interactions. Although accelerated melanogenesis has been shown to potentiate the cytostatic and cytocidal effects of NPrCAP [21], the susceptibility of B16F1 to NPrCAP was decreased in the 3D array (**Fig. 2-4**). The lower drug sensitivities shown by our results were consistent with several studies of cancer

cells, which showed that sensitivity is lower in 3D cultures *in vitro* as well as *in vivo* than in 2D cultures [36]. Furukawa *et al* reported that tridimensional tumor cell culture systems allow observation of lower drug sensitivities and are highly predictive of the pattern of drug response by tumor cells *in vivo* [37]. Ho *et al* also reported that the IC_{50} of glioma cell lines against irinotecan in 3D spheroid culture is higher and closer to the IC_{50} *in vivo* than in 2D cultures [38]. Moreover, Ohmori *et al* reported that drug-resistant EMT-6 cells, which were generated *in vivo* by repeated exposure of EMT-6 tumor-bearing hosts to various anti-tumor agents, maintained or exhibited a resistant phenotype *ex vivo* when grown as tridimensional spheroids, but lost this phenotype in monolayer cultures [39]. We suggest two possible reasons for this low susceptibility in the 3D array. First, we postulate that drug efflux is increased in cancer cells within spheroids in the 3D array because of the increased expression of drug-efflux molecules. Intercellular and cell-ECM interactions have been shown to activate the expression of drug efflux transporters such as MDR1 via Akt and PKC signaling pathways, leading to drug resistance and increased malignancy [38-42]. Second, we hypothesize that drug penetration into the cells within spheroids in the 3D array decreases as a result of spheroid formation. Drug penetration into spheroids has been shown to be relatively inefficient, which partly accounts for the resistance of solid tumors to chemical treatments *in vivo* [36]. Although the diffusion limitation becomes greater according to the spheroid size, multicellular spheroids, which were less than 100 μm in diameter in the present study, form hypoxic core regions due to the diffusion limitation of oxygen [44]. Because the drug molecules had a greater diffusion limitation within spheroids than oxygen, the spheroids in our 3D array also contained a region with a low drug concentration. Therefore, the formation of spheroids and the decreased drug susceptibility in 3D arrays indicate that this culture method closely resembles an *in vivo* physiological microenvironment.

We showed that the developed model could be used to evaluate anti-proliferative effects

in 3D array assays using the melanoma-targeting drug NPrCAP coupled with heat treatment *in vitro*, and an additive effect was observed under most conditions (**Table 2-1**). This conclusion is reasonable because NPrCAP produces oxidative radicals in melanogenesis [21-25], and heat treatment similarly induces heat-mediated oxidative stress [31]. In contrast, our previous *in vivo* study showed that combined treatment with NPrCAP and hyperthermia results in a synergistic or additive effect on generating tumor-infiltrating lymphocytes that kill melanoma cells in distant metastases [29]. Considering the differences between the *in vitro* and *in vivo* studies, a 3D array with co-culture of cancer cells and lymphocytes would provide a more physiologically relevant model for combined effect analysis of drug treatments and inflammation. We previously constructed a co-culture model using 3D arrays to evaluate the accelerated invasiveness and gene expression related to cancer malignancy via the interaction between mouse melanoma and human vascular endothelial cells [10]. Therefore, the combination of the co-culture technique [10] and the evaluation technique developed in the present study will likely provide a highly applicable technique for analysis and drug screening in the future.

In conclusion, 3D cell spheroid culture array using magnetic cell patterning method may provide a more physiologically relevant format for drug screening or pharmacological analysis in cancer cells.

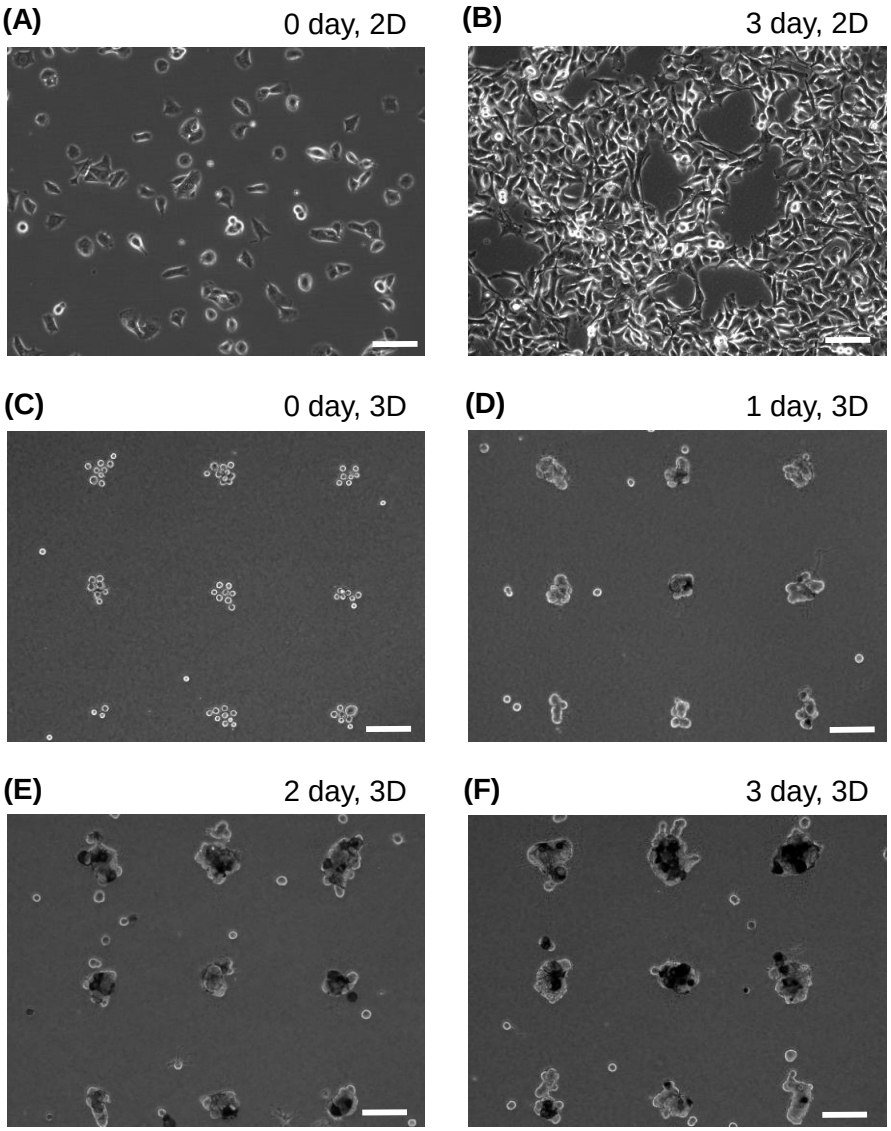

Fig. 2-1. Morphology of B16F1 melanoma cells in 3D arrays. B16F1 was cultivated in 3D arrays (A-D) and 2D cultures (E, F). Time-lapse images of mouse melanomas were obtained after 0 (A, E), 1 (B), 2 (C), and 3 days (D, F) of cultivation. *Scale bar*: 100 μm.

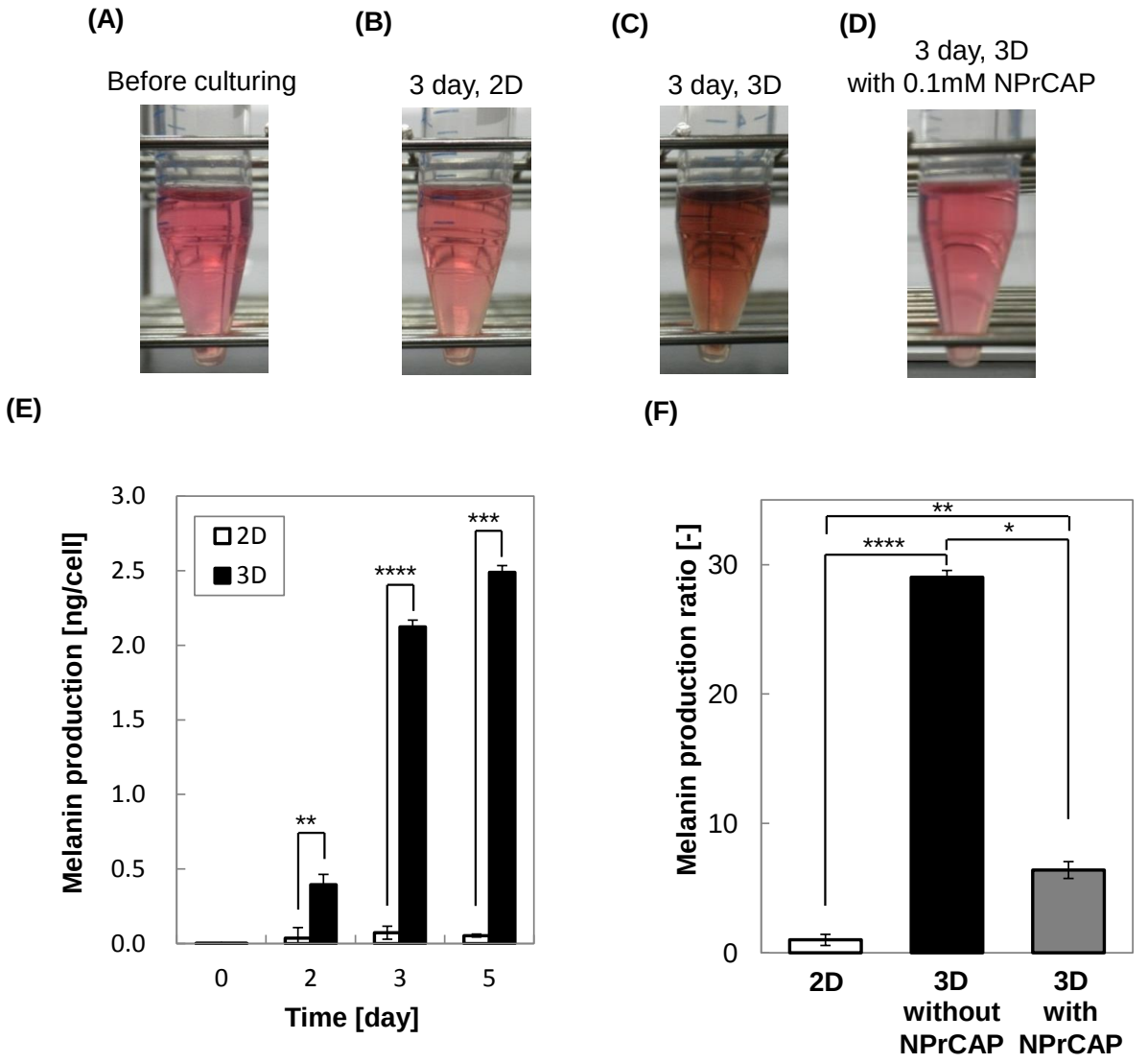

Fig. 2-2. Melanin production of B16F1 melanoma cells in 2D cultures and 3D arrays. Images show the culture supernatant before (A) and after 3 days of cultivation (B-D) in 2D (B) and 3D array (C, D) cultures. Treatment with 0.1 mM N-propionyl-4-cysteaminylphenol (NPrCAP) inhibited melanin production in 3D cultures (D). Time course of melanin production (E) and the ratio compared with 2D culture after 3 days of cultivation (F). Data are presented as means ± SD, n = 3. *$p < 0.05$, **$p < 0.01$, ***$p < 0.001$, and ****$p < 5 \times 10^{-5}$ compared with the 2D group, paired two-tailed Student's t-test.

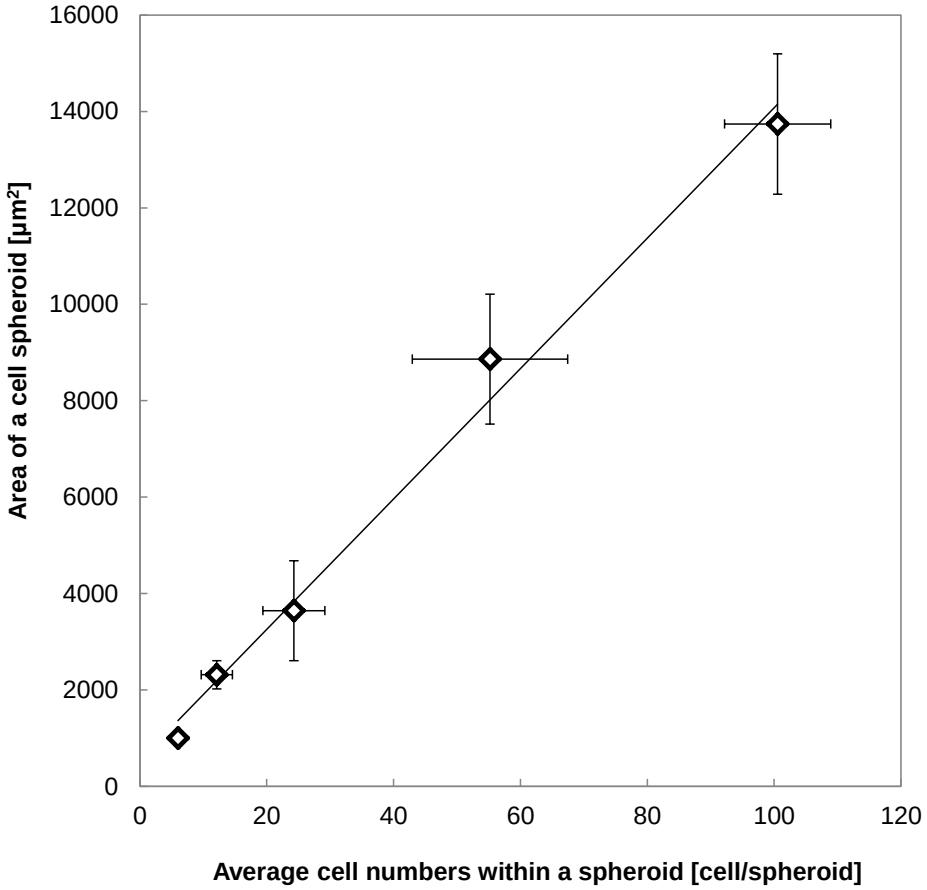

Fig. 2-3. Evaluation of B16F1 cell numbers within a spheroid using the B16F1 spheroid area in phase-contrast images. Phase-contrast images of B16F1 spheroids were obtained every 2 days during 10 days of culture in 3D arrays, and the area of each spheroid was calculated using image analysis software. B16F1 cells in 3D arrays were harvested by collagenase digestion, and the average cell number within a spheroid was calculated to evaluate the relationship between cell proliferation in a spheroid and the spheroid area.

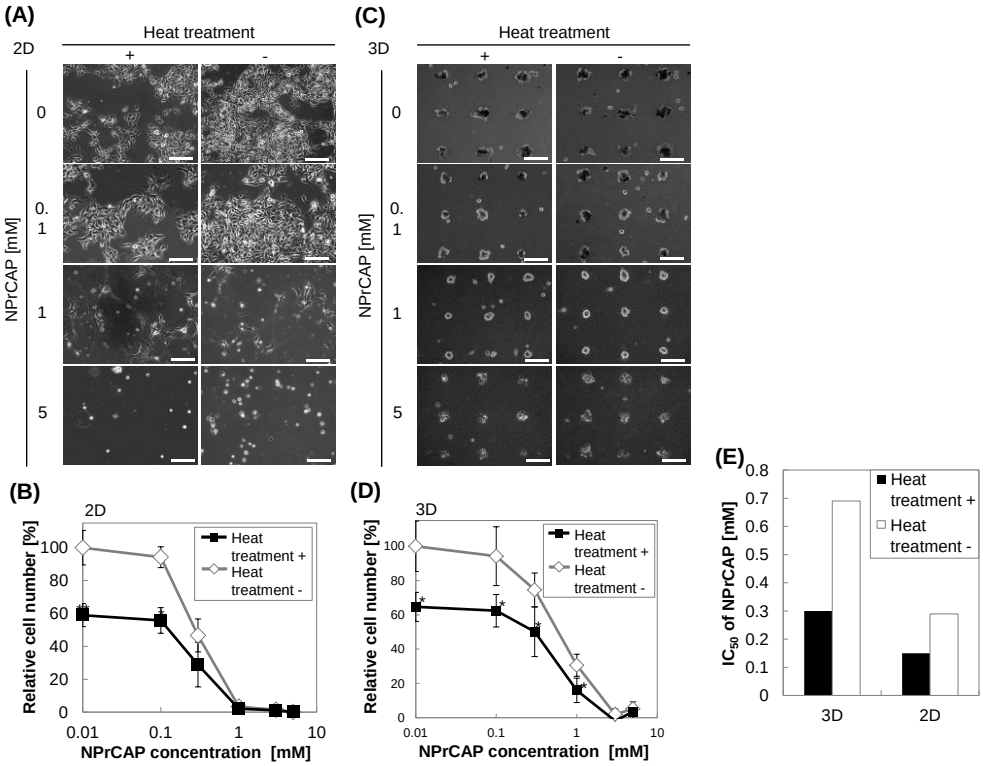

Fig. 2-4. Effect of NPrCAP and heat treatment on the proliferation of B16F1 cells in 2D cultures and 3D arrays. The morphological changes and growth curves of B16F1 cells after 3 days of cultivation in 2D culture (A, B) or 3D arrays (C, D) at various concentrations of NPrCAP with or without heat treatment. The relative cell numbers in 2D culture (B) were based on measuring the cell numbers in a destructive manner. The relative cell numbers in 3D arrays (D) were evaluated based on the relative spheroid area (C) in a non-destructive manner using the correlation shown in Fig. 2-3. Data are presented as means ± SD, n = 30. *$p < 0.05$ and **$p < 0.01$ compared with the non-heated group at the same NPrCAP concentration, paired two-tailed Student's t-test. (E) Half-maximal concentrations (IC_{50}s) of NPrCAP with (closed column) or without (open column) heat treatment in 2D and 3D array cultures. The IC_{50} values were obtained from the growth curves in (B) and (D). Data are presented as means ± SD, n = 5. **$p < 0.01$ compared with the 2D group, paired two-tailed Student's t-test. *Scale bar*: 100 μm.

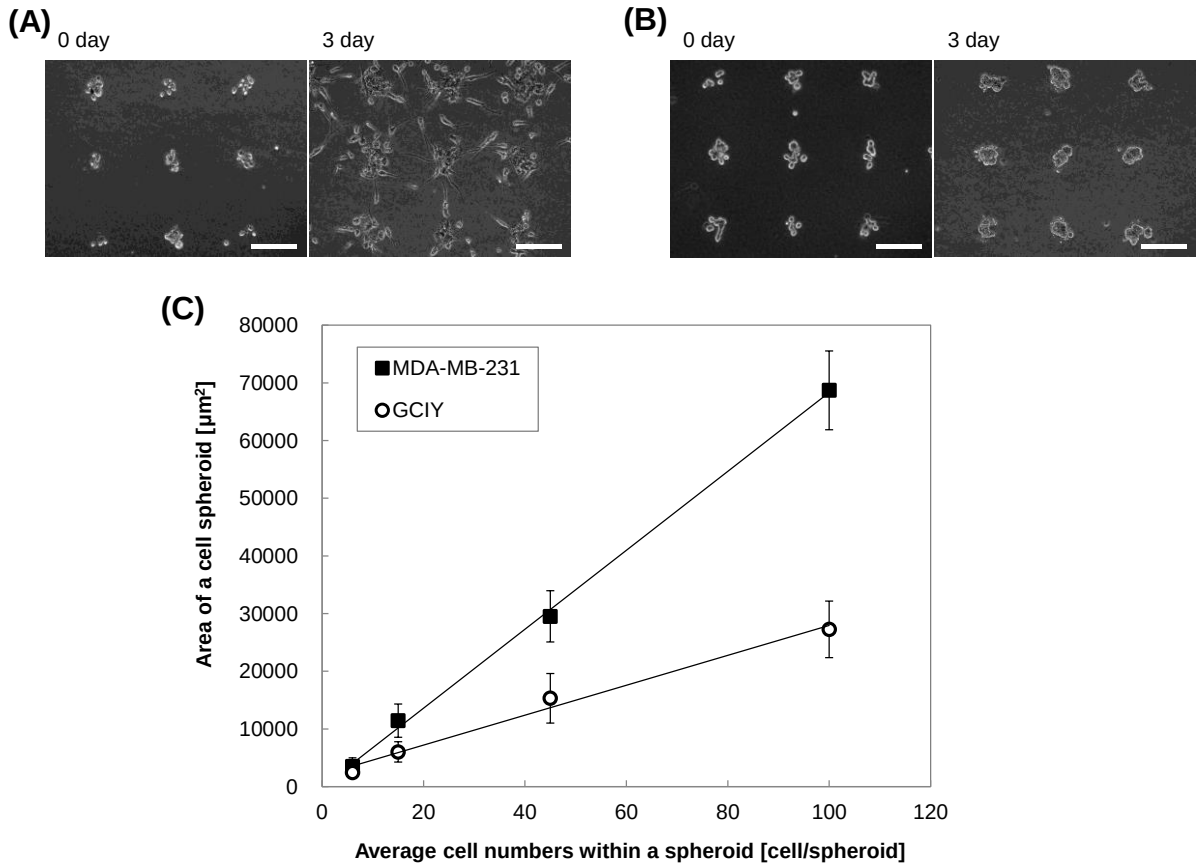

Fig. 2-5. Evaluation of cancer cell numbers within a spheroid calculated from the spheroid area in phase-contrast images. Phase-contrast images of two types of cancer spheroids formed by the human breast cancer cell line MDA-MB-231 (A) and human gastric cell line GCIY (B) were obtained before and after 3 days of culture. (C) Correlation between the spheroid area and average cell number within a spheroid. Phase-contrast images of the spheroids were obtained every 2 days for 10 days of culture in 3D arrays, and the area of each spheroid in the images was measured using image analysis software. The cells in 3D arrays were harvested by collagenase digestion, and the average cell number within a spheroid was calculated. Data are presented as means ± SD, n = 30. *Scale bar*: 100 μm.

Table 2-1. Evaluation of combined effect on difference in NPrCAP concentration and hyperthermic treatment.

Culture condition	NPrCAP concentration [mM]	Viability in single treatment [%]		Observed viability in combination [%]	Expected viability in combination [%]	Evaluation of Combined Effect
		Heat treatment [A]	NPrCAP [B]	[A+B]	[C]	
3D	0.1	64.6±8.5	94.2±17.2	62.4±9.4	60.9	Additive
	0.3		74.6±9.8	50.1±14.5	48.2	Additive
	1		30.6±6.4	15.9±7.1	19.8	Additive
	3		1.9±3.2	-1.9±3.7	1.2	Additive
	5		5.2±4.1	3.5±4.1	3.4	Additive
2D	0.1	58.9±5.6	94.2±6.4	55.8±5.3	55.5	Additive
	0.3		46.7±10.0	28.9±2.7	27.5	Additive
	1		3.3±1.1	2.1±0.2	2	Additive
	3		1.4±0.5	1.2±0.1	0.84	Sub-additive
	5		0.03±0.03	0.02±0.00	0.02	Additive

The heating time was 1 h.

All figures on [A], [B] and [A+B] show mean ± SD (n=3)

*:[C] = [A] × [B] / 100 where [A] and [B] are mean value

2.5. Summary

In this study, three-dimensional (3D) cell culture arrays of melanoma cell spheroids were assembled to evaluate the combined effect of a melanogenesis-targeting drug, N-propionyl-4-cysteaminylphenol (NPrCAP), and heat treatment. An array-like multicellular pattern of mouse melanoma B16F1 cells in a collagen gel was established by magnetic cell labeling using a pin-holder device to exert a magnetic force. The cellular spheroids were exposed to NPrCAP and heat (42°C for 1 h) as a model of anti-cancer treatment. As a result, melanogenesis of B16F1 cells was 29-fold higher in this 3D array than in conventional two-dimensional (2D) monolayer cultures. Because the spheroid size was linearly correlated with the cell number within a spheroid, the anti-proliferative effect could be evaluated in a non-destructive manner. Moreover, the half-maximal inhibitory concentration of NPrCAP coupled with heat treatment calculated from the spheroid size was 2-fold higher in the 3D array (0.30 mM) than in 2D culture (0.15 mM). These results indicate that spheroid formation decreases the chemosensitivity of cancer cells, and this model would be suitable as a susceptibility assay for melanogenesis-targeting drugs. Therefore, this 3D culture model provides a better screening format to evaluate drug and physical treatments for cancer therapy than 2D formats.

2.6. References

1. Birgersdotter A, Sandberg R, Ernberg I. Gene expression perturbation *in vitro* - A growing case for three-dimensional (3D) culture systems. Semin Cancer Biol 15: 405-412, 2005.
2. Petersen OW, Rønnov-Jessen L, Howlett AR, *et al*. Interaction with basement membrane serves to rapidly distinguish growth and differentiation pattern of normal and malignant human breast epithelial-cells. Proc Natl Acad Sci USA 89: 9064-9068, 1992.
3. Ivascu A, Kubbies M. Rapid generation of single-tumor spheroids for high-throughput cell function and toxicity analysis. J Biomol Screen 11: 922-932, 2006.
4. Kang HG, Jenabi JM, Zhang J, *et al*. E-cadherin cell-cell adhesion in ewing tumor cells mediates suppression of anoikis through activation of the ErbB4 tyrosine kinase. Cancer Res 67: 3094-3105, 2007.
5. Kunz-Schughart LA, Freyer JP, Hofstaedter F, *et al*. The use of 3-D cultures for high-throughput screening: The multicellular spheroid model. J Biomol Screen 9: 273-285, 2004.
6. Kim JB. Three-dimensional tissue culture models in cancer biology. Semin Cancer Biol 15: 365-377, 2005.
7. Kenny PA, Lee GY, Myers CA, *et al*. The morphologies of breast cancer cell lines in three-dimensional assays correlate with their profiles of gene expression. Mol Oncol 1: 84-96, 2007.
8. Fennema E, Rivron N, Rouwkema J, *et al*. Spheroid culture as a tool for creating 3D complex tissues. Trend Biotechnol 31: 108-115, 2013.
9. Aref AR, Huang RY, Yu W, *et al*. Screening therapeutic EMT blocking agents in a three-dimensional microenvironment. Integr Biol 5: 381-389, 2013.
10. Yamamoto S, Hotta MM, Okochi M, *et al*. Effect of vascular formed endothelial cell

network on the invasive capacity of melanoma using the *in vitro* 3D co-culture patterning model. PLoS One 9: e103502, 2014.

11. Okochi M, Matsumura T, Yamamoto S, *et al*. Cell behavior observation and gene expression analysis of melanoma associated with stromal fibroblasts in a three-dimensional magnetic cell culture array. Biotechnol Prog 29: 135-142, 2013.
12. Ino K, Okochi M, Honda H. Application of magnetic force-based cell patterning for controlling cell-cell interactions in angiogenesis. Biotechnol Bioeng 102: 882-890, 2009.
13. Okochi M, Matsumura T, Honda H. Magnetic force-based cell patterning for evaluation of the effect of stromal fibroblasts on invasive capacity in 3D cultures. Biosens Bioelectron 42: 300-307, 2013.
14. Ino K, Okochi M, Konishi N, *et al*. Cell culture arrays using magnetic force-based cell patterning for dynamic single cell analysis. Lab Chip 8: 134-142, 2008.
15. Okochi M, Takano S, Isaji Y, *et al*. Three-dimensional cell culture array using magnetic force-based cell patterning for analysis of invasive capacity of BALB/3T3/v-src. Lab Chip. 9: 3378-3384, 2009.
16. Shimizu K, Ito A, Yoshida T, *et al*. Bone tissue engineering with human mesenchymal stem cell sheets constructed using magnetite nanoparticles and magnetic force. J Biomed Mater Res B Appl Biomater 82B: 471-480, 2007.
17. Balch CM, Buzaid AC, Soong SJ, *et al*. Final version of the American Joint Committee on Cancer staging system for cutaneous melanoma. J Clin Oncol 19: 3635-3648, 2001.
18. Ito S, Wakamatsu K. Chemistry of mixed melanogenesis - Pivotal roles of dopaquinone. Photochem Photobiol 84: 582-592, 2008.
19. Ito Y, Jimbow K. Selective cytotoxicity of 4-S-cysteaminylphenol on follicular melanocytes of the black mouse - rational basis for its application to melanoma chemotherapy. Cancer Res 47: 3278-3284, 1987.

20. Thomas PD, Kishi H, Cao H, *et al*. Selective incorporation and specific cytocidal effect as the cellular basis for the antimelanoma action of sulphur containing tyrosine analogs. J Invest Dermatol 113: 928-934, 1999.
21. Ito S, Nishigaki A, Ishii-Osai Y, *et al*. Mechanism of putative neo-antigen formation from N-propionyl-4-S-cysteaminylphenol, a tyrosinase substrate, in melanoma models. Biochem Pharmacol 84: 646-653, 2012.
22. Alena F, Iwashina T, Gili A, *et al*. (1994) Selective *in-vivo* accumulation of N-acetyl-4-S-cysteaminylphenol in B16F10 murine melanoma and enhancement of its *in-vitro* and *in-vivo* antimelanoma effect by combination of buthionine sulfoximine. Cancer Res 54: 2661-2666, 1994.
23. Pankovich JM, Jimbow K. Tyrosine transport in a human-melanoma cell-line as a basis for Selective transport of cytotoxic analogs. Biochem J 280: 721-725, 1991.
24. Tandon M, Thomas PD, Shokravi M, *et al*. Synthesis and antitumour effect of the melanogenesis-based antimelanoma agent N-propionyl-4-S-cysteaminylphenol. Biochem Pharmacol 55: 2023-2029, 1998.
25. Miura S, Ueda T, Jimbow K, *et al*. Synthesis of cysteinylphenol, cysteaminylphenol, and related-compounds, and *in vivo* evaluation of antimelanoma effect. Arch Dermatol Res 279: 219-225, 1987.
26. Ito A, Fujioka M, Yoshida T, *et al*. 4-S-Cysteaminylphenol-loaded magnetite cationic liposomes for combination therapy of hyperthermia with chemotherapy against malignant melanoma. Cancer Sci 98: 424-430, 2007.
27. Shinkai M, Yanase M, Honda H, *et al*. Intracellular hyperthermia for cancer using magnetite cationic liposomes: *In vitro* study. Jpn J Cancer Res 87: 1179-1183, 1996.
28. Kawai N, Ito A, Nakahara Y, *et al*. Complete regression of experimental prostate cancer in nude mice by repeated hyperthermia using magnetite cationic liposomes and a newly

developed solenoid containing a ferrite core. Prostate 66: 718-727, 2006.

29. Jimbow K, Tamura Y, Yoneta A, *et al*. Conjugation of magnetite nanoparticles with melanogenesis substrate, NPrCAP provides melanoma targeted, in situ peptide vaccine immunotherapy through HSP production by chemo-thermotherapy. J Biomaterials Nanobiotechnol 3: 140-153, 2012.
30. Ito A, Yamaguchi M, Okamoto N, *et al*. T-cell receptor repertoires of tumor-infiltrating lymphocytes after hyperthermia using functionalized magnetite nanoparticles. Nanomedicine 8: 891-902, 2013.
31. Jimbow K, Ishii-Osai Y, Ito S, *et al*. Melanoma-targeted chemothermotherapy and in situ peptide immunotherapy through HSP production by using melanogenesis substrate, NPrCAP, and magnetite nanoparticles. J Skin Cancer 2013: 742925, 2013.
32. De Pauw-Gillet MC, Christiane YM, Foidart JM, *et al*. Analysis of tridimensional mixed cultures of mouse B16 melanoma cells and 3T3 fibroblasts. Anticancer Res 8: 153-160, 1988.
33. Tomihari M, Chung JS, Akiyoshi H, *et al*. DC-HIL/glycoprotein Nmb promotes growth of melanoma in mice by Inhibiting the activation of tumor-reactive T cells. Cancer Res 70: 5778-5787, 2010.
34. Valeriote F, Lin H. (1975) Synergistic interaction of anticancer agents: a cellular perspective. Cancer Chemother Rep 59: 895-900, 1975.
35. Friedl P, Alexander S. Cancer invasion and the microenvironment: Plasticity and reciprocity. Cell 147: 992-1009, 2011.
36. Ho WJ, Pham EA, Kim JW, *et al*. Incorporation of multicellular spheroids into 3-D polymeric scaffolds provides an improved tumor model for screening anticancer drugs. Cancer Sci 101: 2637-2643, 2010.
37. Furukawa T, Kubota T, Watanabe M, *et al*. High *in vitro-in vivo* correlation of drug

response using sponge-gel-supported 3-dimensional histoculture and the MTT end-point. Int J Cancer 51: 489-498, 1992.

38. Wartenberg M, Gronczynska S, Bekhite MM, *et al*. Regulation of the multidrug resistance transporter P-glycoprotein in multicellular prostate tumor spheroids by hyperthermia and reactive oxygen species. Int J Cancer 113: 229-240, 2005.
39. Ohmori T, Yang JL, Price JO, *et al*. Blockade of tumor cell transforming growth factor-beta s enhances cell cycle progression and sensitizes human breast carcinoma cells to cytotoxic chemotherapy. Exp Cell Res 245: 350-359, 1998.
40. Yeo EJ, Chun YS, Park JW. New anticancer strategies targeting HIF-1. Biochem Pharmacol 68: 1061-1069, 2004.
41. Viale M, Cordazzo C, Cosimelli B, *et al*. Inhibition of MDR1 activity *in vitro* by a novel class of diltiazem analogues: Toward new candidates. J Med Chem 52: 259-266, 2009.
42. Longati P, Jia X, Eimer J, *et al*. 3D pancreatic carcinoma spheroids induce a matrix-rich, chemoresistant phenotype offering a better model for drug testing. BMC Cancer. 13: 13, 2013.
43. Oshikata A, Matsushita T, Ueoka R. Enhancement of drug efflux activity via MDR1 protein by spheroid culture of human hepatic cancer cells. J Biosci Bioeng 111: 590-593, 2011.
44. Yoshii Y, Waki A, Yoshida K, *et al*. The use of nanoimprinted scaffolds as 3D culture models to facilitate spontaneous tumor cell migration and well-regulated spheroid formation. Biomaterials 32: 6052-6058, 2011.

Chapter 3

Cell Behavior observation and gene expression analysis of melanoma associated with stromal fibroblasts in a three-dimensional magnetic cell culture array

3.1. Introduction

Invasion and metastasis are the hallmarks of malignant tumors. Tumor cell behavior is regulated by its intrinsic properties as well as by its microenvironment, which comprises resident fibroblasts, endothelial cells, pericytes, leucocytes, and extracellular matrix (ECM). The complex interaction between invasive tumor cells and the tumor microenvironment is only beginning to be understood. The tumor stroma is increasingly appreciated as an integral part of cancer initiation, growth, and progression, by increasing the number of fibroblasts, enhancing capillary density, and promoting Type-I collagen and fibrin deposition. Fibroblasts are among the major stromal cells in the tumor microenvironment and its functions include the deposition of ECM, regulation of epithelial differentiation, regulation of inflammation, and involvement in wound healing [1-4]. The fibroblasts involved in primary tumor formation

and invasion are referred to as cancer associated fibroblasts (CAFs) [3-6]. The presence of invasive tumor cells stimulates resident stromal fibroblasts and alters gene and protein expression that promotes the invasive capacity of tumor cells [5-7]. Up-regulation of key chemokine and cytokine expression in stromal fibroblasts was reported in the presence of migrating melanoma, promoting conditions for infiltration of macrophages and neutrophils, which may in turn support the metastatic process as well as provide conditions favorable for tumor cell chemotaxis and invasion [8, 9]. Stromal fibroblasts have become recognized as a new target for cancer therapy, and organized 3D culture models have been developed to elucidate factors affecting tumor behaviors [7, 10, 11].

The advent of microengineering has provided biologists with unprecedented opportunities for cell handling and investigations on a cell-to-cell and cell-to-substrate basis [12-15] as well as soluble factors16 for precise analysis in controlled systems. Construction of multicellular spheroid-based functional assay platforms has been also established for screening and evaluation of anti-cancer drugs as well as tissue engineering [17-21]. These *in vitro* cell assay models provide controllable culturing and real-time measurements of large spheroid populations that would be useful in pharmaceutical industry, and the growth dynamics of multicellular spheroids could be modeled biophysically [22]. Cell micropatterning using microcontact printing has also become an important technology for development of spheroid microarray culture microsystem [23, 24]. A 3D micropatterning technique that rapidly arranges cells within hydrogels using dielectrophoretic (DEP) forces was reported to modulate tissue function through the control of microscale cellular architecture [25]. However, some culture media and culture biomaterials, such as collagen and Matrigel, might be less suitable for use with DEP electro-patterning since they may be more conductive, more viscous, and more difficult to gel in a closed chamber. Apart from the electrical techniques, optical [26, 27], ultrasound [28, 29], and magnetic techniques [30-32]

are also currently under development for their use in assembling cells for tissue engineering.

We have recently developed a three-dimensional cell culture array using magnetic force-based cell patterning for analyzing the invasive capacity of tumor cells [32-35]. The target tumor cells were magnetically labeled by magnetite cationic liposomes (MCLs) that contain 10 nm magnetite nanoparticles, and the magnetically labeled cells were allocated in an array platform using a pin-holder device fabricated by processing electromagnetic soft iron in which each pillar is aligned at equal micrometric intervals for magnetic convergence. Magnetically labeled cells were allocated at single [32, 34] and multiple [33, 35] cell levels by varying the cell-seeding density using this pin-holder device. This was applied to cell behavior analysis, for example, in the formation of cord-like structures in human umbilical vein endothelial cells [33] as well as in cancer invasion screens by formation of cancer-cell spheroids embedded in 3D-ECM [35]. Construction of cell arrays using magnetism have also been investigated in microfluidic systems producing spatially patterned magnetic fields and immunomagnetic cell labeling [30, 36-39]. Cell patterning enables control of cellular microenvironments; magnetic patterning using the pin-holder device would be suitable for 3D patterning such as in collagen and Matrigel.

In the present study, a 3D multicellular tumor spheroid culture array was fabricated for evaluating the effect of stromal fibroblast on the invasive capacity of melanoma. Formation of melanoma spheroid was developed using a pin-holder device and an external magnet, which enables the assembly of the magnetically labeled cells on the collagen gel-coated surface as array-like cell patterns. Stromal fibroblasts were arranged magnetically with cancer cells or mixed in upper collagen gel for morphological analysis of cancer invasion in direct- and indirect-interaction models, respectively. Given its ability to perform cell-based assays in the tumor microenvironment in a simple and objective manner, this system will give new possibilities in terms of identifying key mechanisms of tumor cell invasion and metastasis and

potentially therapeutic nodes for attenuating primary tumor metastasis.

3.2. Materials and methods

3.2.1. Cell culture

The human melanoma cell M-1 was cultured in RPMI1640 medium with 10% fetal bovine serum (FBS, Sigma-Aldrich, St. Louis, MO), to which was added penicillin G sodium salt (100 U/mL) and streptomycin sulfate (0.1 μg/mL). The cells were cultured in a humidified 5% carbon dioxide incubator at 37˚C. The mouse fibroblast NIH-3T3 was cultured in Dulbecco's Modified Eagle Medium (DMEM) medium, to which was added 10% FBS, penicillin G sodium salt (100 U/mL), and streptomycin sulfate (0.1μg/mL). The cells were cultured in a humidified 5% carbon dioxide incubator at 37˚C.

3.2.2. Preparation of MCL and magnetic cell labeling

MCL was prepared using magnetite nanoparticles (Fe_3O_4, mean diameter 10 nm, Toda Kogyo Co., Hiroshima, Japan) and a lipid mixture of TMAG, DLPC, and DOPE at a respective molar ratio of 1:2:2, as described in 2.2.2.. Magnetite concentration was measured using the potassium thiocyanate method [24].

For magnetic labeling, the cells were cultured until sub-confluent and placed in a fresh medium that contained finely dispersed MCL at 100 pg-magnetite per cell. After 2 h of incubation with MCL, the cells were washed to remove the non-introduced magnetite nanoparticles. The magnetically labeled cells were collected with 0.25% trypsin-EDTA (Gibco, Carlsbad, CA). The quantity of magnetite nanoparticles introduced was determined by iron concentration from the absorbance in colorimetric reaction. That is, the cell pellet contained MCL (2×10^5 cells) was completely dissolved by the addition of 12 M HCl (200 mL), and vortex mixing. Then, 5% trichloroacetic acid (1 mL) was added to the mixture and

incubated at 4˚C for 30 min, followed by centrifugation to remove the precipitated protein. The iron concentration was measured by colorimetric reaction using 1% potassium thiocyanate [40].

3.2.3. Preparation of 3D cell arrays using the pin-holder device

A pin-holder device was fabricated to allot magnetically labeled cells by the profile of their magnetic distribution, as described in 2.2.2. The device was constructed by magnetic soft iron using a wire electrical discharge machine (DIAX-FX10; Mitsubishi Electric Co., Tokyo, Japan) with a cutting wire (diameter: 0.1 mm; Sumitomo Electric Industries, Osaka, Japan) to construct the array of square-pole type pillars. The magnetic field was concentrated on the pillars using an external neodymium disc magnet (50 mm in diameter and 10 mm in height with a surface magnetic induction of 0.38 T; Niruko Factories Co., Shiga, Japan).

For construction of 3D cell arrays, the collagen mixture was prepared by mixing a 7:2:1 volume ratio of an ice-cold collagen solution, 0.3% Cellmatrix Type I-A (Nitta Gelatin, Osaka, Japan) with 5 × DMEM and 10 × sterile reconstitution buffer (2.2 g $NaHCO_3$ in 100 mL of 0.05 M NaOH and 0.2 nM 2-[4-(2-hydroxyethyl)-1-piperazinyl]ethane sulfonic acid (HEPES)) as described in the instruction. The culture dish (hydrophilic lummox dish, Assist, Tokyo, Japan) was covered with a thin layer of collagen gel and placed on the pin-holder device with the magnet facing downward, and the arrangement of magnetically labeled cells was carried out. Magnetically labeled cells were seeded in the dish and incubated at 37˚C for 30 min for cell arrangement. After formation of the 3D cell array, the 0.21% collagen mixture was overlaid and incubated at 37˚C for 30 min for gelation, and the culture medium was then subsequently added to the dish. The pin-holder device and the magnet were removed from the culture dish after cell arrangement. As a result, all the inoculated cells were arranged in the same cross-section, and behaviors of target cells such as growth and invasion were observed

simultaneously via microscopy.

3.2.4. Preparation of cell culture arrays for analysis of melanoma-stromal fibroblast interaction using the pin-holder device

The 3D cell culture array platform for evaluation of the effect of stromal fibroblasts on the invasive capacity of cancer cells was constructed using magnetic force-based cell patterning [35]. For fluorescent observation of cell behaviors, target M-1 cells were stained using CellTracker green (20 μM, molecular probes), and NIH-3T3 were stained with CellTracker orange (20 μM, molecular probes) before MCL labeling. For preparation of the fibroblast direct-interaction array, magnetically labeled cancer cells and stromal fibroblasts were harvested together in the dish (1.8×10^5 cells/dish of M-1 cells and 9.0×10^4 cells/dish of NIH-3T3), and the 0.21% collagen mixture was then overlaid (1 mL) and incubated at 37˚C for 30 min for gelation. The culture medium was then added to the dish for cultivation, and the pin-holder device and magnet were removed from the culture dish after cell arrangement (**Fig. 3-1A**, direct-interaction array).

As a result, all the inoculated cells were arranged in the same cross-section, and behaviors of target cells such as growth and invasion were observed simultaneously via microscopy. For preparation of the fibroblast indirect-interaction array, 1.8×10^5 cells/dish of M-1 cells was allocated in array, and NIH-3T3 (8.0×10^5 cells/mL-collagen gel) was mixed uniformly in the collagen gel (**Fig. 3-1B**). For preparation of the 3D cancer cell array on the fibroblast sheet, NIH-3T3 cells cultured until confluent was treated with 10 μg/mL mitomycin C (Wako, Tokyo, Japan) in the medium for 90 min, and washed by phosphate buffered saline (PBS). After preparation of the fibroblast sheet, 1.8×10^5 cells/dish of magnetically labeled M-1 cells were allocated in array on the fibroblast sheet, and then embedded with collagen I (**Fig. 3-1C**, fibroblast-sheet array).

3.2.5. Image analysis

Time-elapse monitoring of the cell in 3D cell array was performed using phase microscopy (model IX81, Olympus Co., Tokyo, Japan). The proliferation area of cells after cultivation was calculated by image analysis software (MetaMorph, Universal Imaging Co., Downingtown, PA) using three images at each condition.

3.2.6 Zymographic analysis

The culture media were analyzed by gelatin zymography as previously described [41]. Briefly, 15 μL of supernatants were mixed with 6 × loading buffer (50 mM Tris-HCl, pH6.5, 10% glycerol, 2% SDS, 0.1% bromophenol blue), and fractionated on 10% SDS-polyacrylamide gels containing 0.1% gelatin (Difco Laboratories). Gels were washed twice in 2.5% Triton X-100 for 30 min before reaction (1 h incubation at room temperature and 15 h incubation at 37˚C) in metalloproteinase substrate buffer (50 mM Tris-HCl, pH 7.5, 5 mM $CaCl_2$, 150 mM NaCl) and stained with Coomassie brilliant blue R-250. Bands corresponding to gelatinase activities appeared white against a blue background.

3.2.7 Gene expression analysis

M-1 cells cultured in 2D and 3D at random or in array were collected and treated with 0.033% collagenase. The cells were washed with PBS and lysed using lysis enhancer and resuspension buffer of CellsDirect One-step qRT-PCR kits (Invitrogen). Total RNA was extracted using the RNeasy mini kit according to its protocol (Qiagen, Basel, Switzerland). Real-time RT-PCR assays were conducted on an ABI StepOne Real Time PCR Systems, using SYBR Green RNA 1step kit (Applied Biosystems, Branchburg, NJ). The M-1 specific primers for human glyceraldehyde 3-phosphate dehydrogenase (GAPDH) (forward:

5’-CCTGACCTGCCGTCTAGAAA-3’, reverse: 5’-TGCTGTAGCCAAATTCG TTG-3’), interleukin-8 (IL-8) (forward: 5’-ATTAGCCACCATCTTACCTC ACAGT-3’, reverse: 5’-GTGCTTCCACATGTCCTCACA-3’), MMP-2 (forward: 5’-GCTGGCTGCCTT AGAACCTTTC-3’, reverse: 5’-GAACCATCACTATGTGGGCTGAGA-3’) were designed using the Primer3Plus and sequences from NCBI’s gene bank. To quantify gene expression in each sample, we used the comparative threshold cycle (Ct) method. Normalization of gene expression was performed using GAPDH as reference gene, and data were expressed as a ratio to a reference sample. The number of M-1 cells was counted by fluorescent microscopy with M-1 and 3T3 mixed cell samples.

3.3. Results

3.3.1. Magnetic labeling and cell patterning using the pin-holder device in 3D array

The effect of MCL uptake on cell growth was investigated with the malignant melanoma M-1. When MCL was added at a concentration of 100 pg/cell, the MCL uptake after 2 and 4 h incubation was 3.2 and 4.4 pg/cell, respectively. Change in cell growth was not observed when cultured with and without MCL labeling (data not shown), and uptake of MCL was confirmed to have little effect on cell growth as described in previous studies [32-35]. Since cell patterning was fully performed at 1 pg/cell, MCL labeling time was set to 2 h throughout this study.

Fig. 3-2 shows the phase micrographs of magnetically labeled melanoma cultured in 2D and 3D conditions. When the melanoma was cultured randomly in 3D, it showed spherical morphology, in contrast to spindle morphology observed when cultivated on dishes (**Figs. 3-2A, 3-2B**). The magnetic labeling by MCL did not change cell migration without attraction of magnet. When M-1 cells were patterned in array on a thin collagen gel layer, cell spreading and growth were observed in clusters after day 3 (**Fig. 3-2C**). In contrast, when M-1 cells

were patterned in array on a thin collagen layer and embedded again with collagen gel, formation of spheroids was observed (**Fig. 3-2D**). Although highly invasive melanoma of M-1 cells was cultured in the 3D array, the cells were clustered and did not show invasive behaviors. This indicates that a more biomimetic model, such as the addition of stromal cells, would be necessary to see the invasive characteristics of malignant melanoma.

3.3.2. Effect of stromal fibroblasts on cell behaviors of melanoma in direct- and indirect-interaction array

Fig. 3 shows the effect of stromal fibroblasts on cell behaviors of melanoma. The M-1 and NIH-3T3 cells were stained with CellTracker green and orange, respectively for fluorescent observation, and NIH-3T3 cells were allocated together with M-1 cells or harvested with collagen gel containing NIH-3T3. With the direct interaction array, M-1 and NIH-3T3 were magnetically labeled and patterned together on the collagen gel layer using the pin-holder device, and embedded again with the collagen gel. Approximately, 5-10 cells were allocated at various proportions on each locus. According to the cell spreading of fibroblasts, the melanoma cells showed slight movement and loose cell pattern, while the cells were compacted in spheroids when patterned without fibroblasts (**Figs. 3-3A, 3-3B**). With the indirect-interaction array, the red absent light of NIH-3T3 cells mixed in the collagen gel was observed, and slight spreading of melanoma cell clusters was observed (**Fig. 3-3C**). These results indicated that the invasive behavior of melanoma cells was affected by the direct interaction of fibroblasts as well as by the secreted soluble factors.

3.3.3. Cell behaviors of melanoma on the fibroblast-sheet array

The effect of cell behaviors of melanoma patterned on the fibroblast cell sheet was investigated (**Fig. 3-4**). The M-1 was stained with CellTracker green and NIH-3T3 was not

stained. In the fluorescent image, the spreading and invasion of M-1 cells was observed on Day 1 and further accelerated invasion was observed after Day 2 (**Fig. 3-4A**). This model represents both direct and indirect effects of fibroblast cells, and intensive cell movement indicating an invasive capacity of M-1 was observed in comparison to **Figs. 3-3B and 3-3C**. The cell area of M-1 patterned on collagen I gel and 3T3 fibroblast sheet was compared by image analysis (**Fig. 3-4B**), and 3-fold increase was observed after 2 days cultivation on 3T3-sheet array while it was below 2-fold on collagen I layer and embedded in collagen. Therefore, it was shown that the invasive cell behavior of melanoma was observed when patterned on a fibroblast-sheet array.

The matrix metalloproteinase (MMP) activity of culture supernatant with each condition was confirmed by a gelatin zymography (**Fig. 3-4C**). The activity of pro- and active MMP-9, MMP-2, and MMP-13 observed in the supernatant of M-1 array, 3T3-sheet, and co-culture of M-1 spheroids on 3T3-sheet, respectively. With M-1 spheroid array embedded in collagen, the activity of MMP-9 and MMP-2 was slightly low. In contrast, all bands were strongly observed with 3T3-sheet and co-culture of M-1 spheroids on 3T3-sheet. Therefore, comparable gene expression analysis between patterned M-1 cells cultured on 3T3-sheet arrays and on collagen layers with embedded collagen was performed to emphasize the fibroblast interaction. **Fig. 3-4D** shows the relative fold induction of IL-8 and MMP-2 of M-1 patterned on 3T3-sheet arrays using specific primers for human RNA. When M-1 was patterned in array on the fibroblast sheet, the expression of IL-8 and MMP-2 increased by 24-fold and 2-fold compared to without fibroblasts in real time RT-PCR, respectively. Since IL-8 and MMP-2 are the important metastasis-associated genes [9, 42], the increase in gene expression was comparable to the invasive cell behaviors displayed in **Fig. 3-4A**. These results indicate that the interaction between melanoma and fibroblast influence the gene expression levels of MMPs and cytokines related to tumor invasion in melanoma and

fibroblasts cells and enhanced melanoma migration. Therefore, the melanoma spheroid arrays on fibroblast-sheets with embedded collagen I demonstrate the importance of fibroblasts in invasive cell behaviors in bioengineered tumor microenvironments.

3.4 Discussion

Microengineering techniques for cellular analysis are emerging as the next revolution in tools to study tissue formation, function, disease development, and disease progression. Morphological and phenotypic typing of cancer cells is advancing due to the development of personalized medicine approaches and the discovery of key factors affecting cell invasion and metastasis. *In vitro* 3D cell culture systems mimicking tumor microenvironments have attracted attention since these models contain the structural architecture necessary for studying cellular interactions [6, 15, 19, 20, 43-46]. High-throughput spheroid culture was also reported for efficient anti-cancer drug screening [7, 17, 18, 20]. These microdevices possess advantages over conventional cell culture systems, including the ability to produce 3D architecture with controlled spatial relationships between the cells in ECM.

In the present study, we have investigated the effect of stromal fibroblasts on the invasive capacity of melanoma with three models: direct-interaction array, indirect-interaction array, and fibroblast-sheet array (**Fig. 3-1**). It has become increasingly clear that the stromal fibroblasts with cellular and ECM components play a crucial role in regulating the process of tumor development and progression. Since cancer cells directly or indirectly orchestrate the modification of the microenvironment by attracting or activating stromal cells, cell culture platforms for analysis of each effect have emerged. Drasdo and Hoehme reported the computer simulations from an individual-based model of tumor growth in monolayers and multi-cellular spheroids, and investigated how the growth dynamics of individual cells affect the macroscopic properties of a growing tumor [22]. This study suggests the importance of

small-scale *in vitro* processes for elucidation of parameters affecting tumor growth.

In the fibroblast-sheet array that includes both direct- and indirect-interaction of fibroblast cells, significant changes in cell morphology and invasion of M-1 was observed (**Fig. 3-4**). Since cell morphology changed only slightly in the direct and indirect interaction array, the fibroblast-sheet array appears to represent a sufficient microenvironment for invasion. The upregulation of metastasis-associated genes (IL-8 and MMP-2) in the fibroblast-sheet array also indicates the acceleration of invasive capacity in the presence of a fibroblast- sheet. The MMPs selectively degrade various components of the ECM and release growth factors, cytokines, and chemokines. It is also reported that interaction between melanoma cells and fibroblasts are mediated by ADAMs (a disintegrin and metalloproteinase) with both their proteolytic and adhesive functions involved in melanoma invasion and progression [47]. In a co-culture system, tumor cells interact with their surrounding ECM or stromal cells and enhance expression of MMPs, cytokines, and chemokines that orchestrate tumor growth and progression. These MMPs degrade ECM and enhance tumor cell migration and increase fibroblast cell interaction [48, 49]. Although this bioengineered tumor model is only a simple representation of the complex nature of a malignant tumor, the *in vitro* 3D spheroid array responded to the stimuli by fibroblast-sheet and invasion of melanoma was observed.

The array-like patterning would be also effective to see the effect of different variables. Using the 3D array-like patterning culture, it is possible to investigate the effect of spheroid size upon invasion in relation to anti-cancer drug evaluation by changing pin size or number of the pin-holder device. Also, this model would be effective to see cell heterogeneity since our 3D array-like cell patterning model enables analysis on a plane surface. The *in vitro* 3D spheroid culture array developed in this study represents a functional tumor model that will facilitate future evaluation of the invasive capacity of tumor cells as well as their

pharmacological responses.

In conclusion, *in vitro* 3D spheroid culture array using magnetic cell patterning is greatly advantageous for cell culture, analysis, and diagnostic application where biomimetic microenvironment by coexisting cells is important.

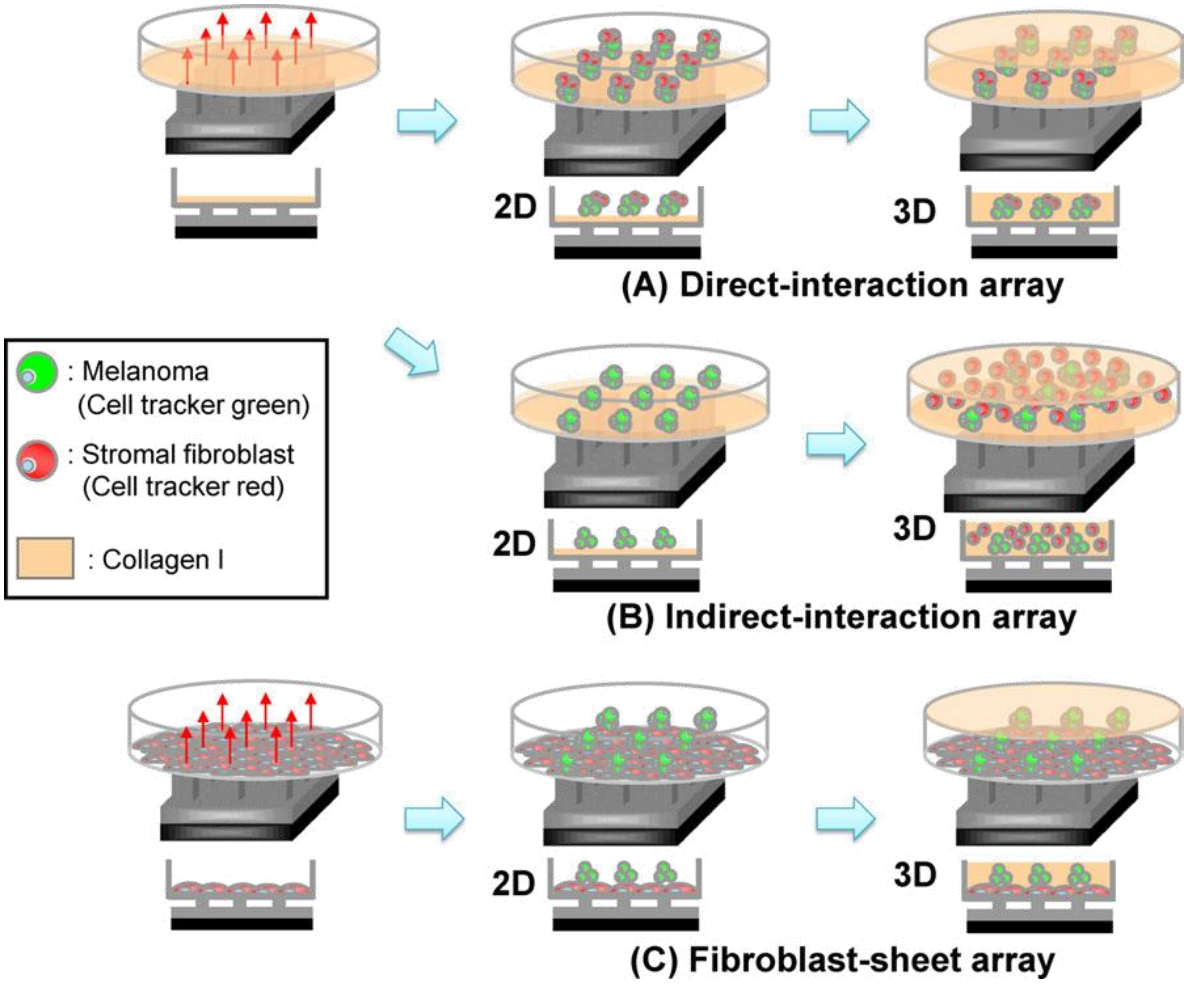

Fig. 3-1. Schematic diagram of magnetic force-based cell patterning using a pin-holder device for observation of melanoma associated with stromal fibroblast in a 3D microenvironment. (A) Direct interaction array model: fibroblasts were also magnetically labeled and patterned together in array with melanoma spheroids. (B) Indirect interaction array model: fibroblasts coexist in the upper collagen gel of melanoma spheroids. (C) Fibroblast-sheet array model: fibroblast-sheet coexists under melanoma spheroids.

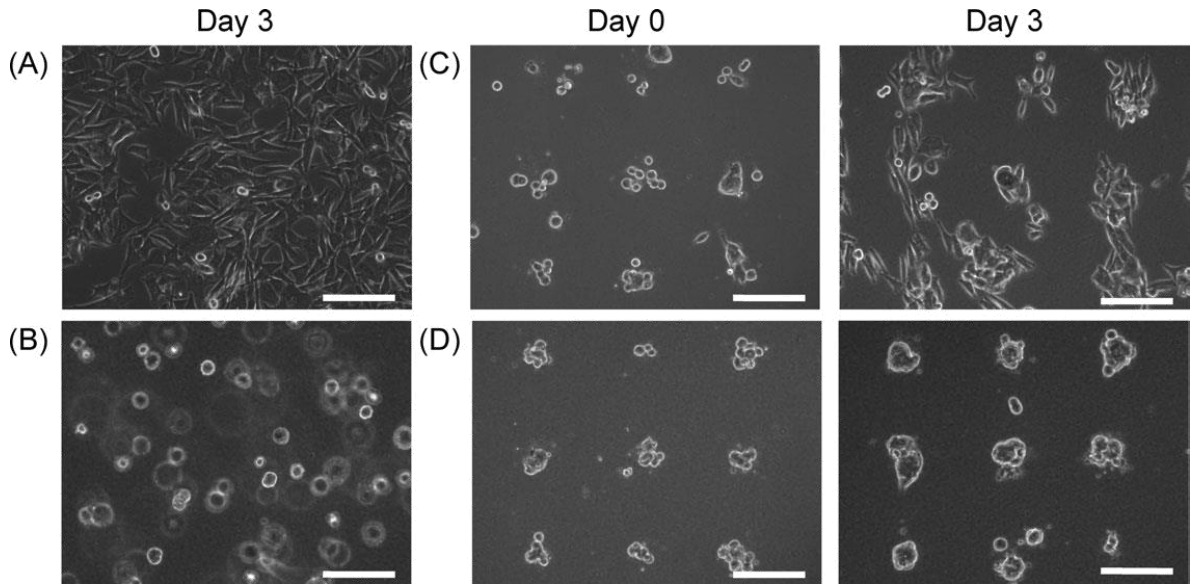

Fig. 3-2. Phase microscopy images of melanoma M-1 cells cultured in culture dish, 2D (A), in collagen I gel, 3D (B). Using a pin-holder device, the magnetically labeled M-1 cells were patterned on collagen I layer (C), and further embedded in collagen I gel (D). Melanoma spheroid was developed when magnetically patterned M-1 cells were cultured in a 3D microenvironment. Scale bar, 200 μm.

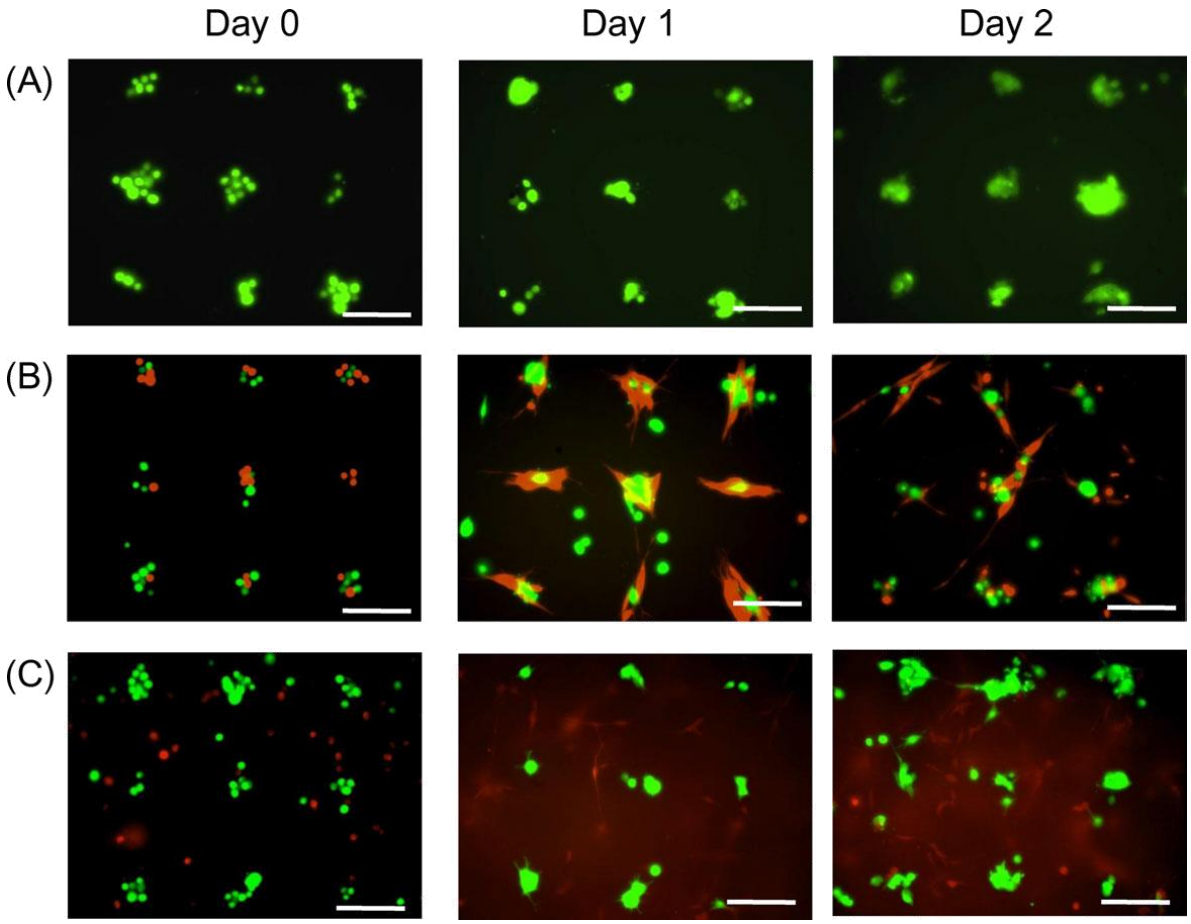

Fig. 3-3. Fluorescent micrographs of magnetically patterned melanoma M-1 embedded in collagen gel (A). The effect of associated fibroblasts on cell behaviors of M-1 was investigated with direct- (B) and indirect-interaction (C) array models. M-1 and NIH-3T3 were stained using CellTracker green and orange, respectively. Scale bar, 200 μm. *$p < 0.05$ (Student's t test, paired, two-tailed).

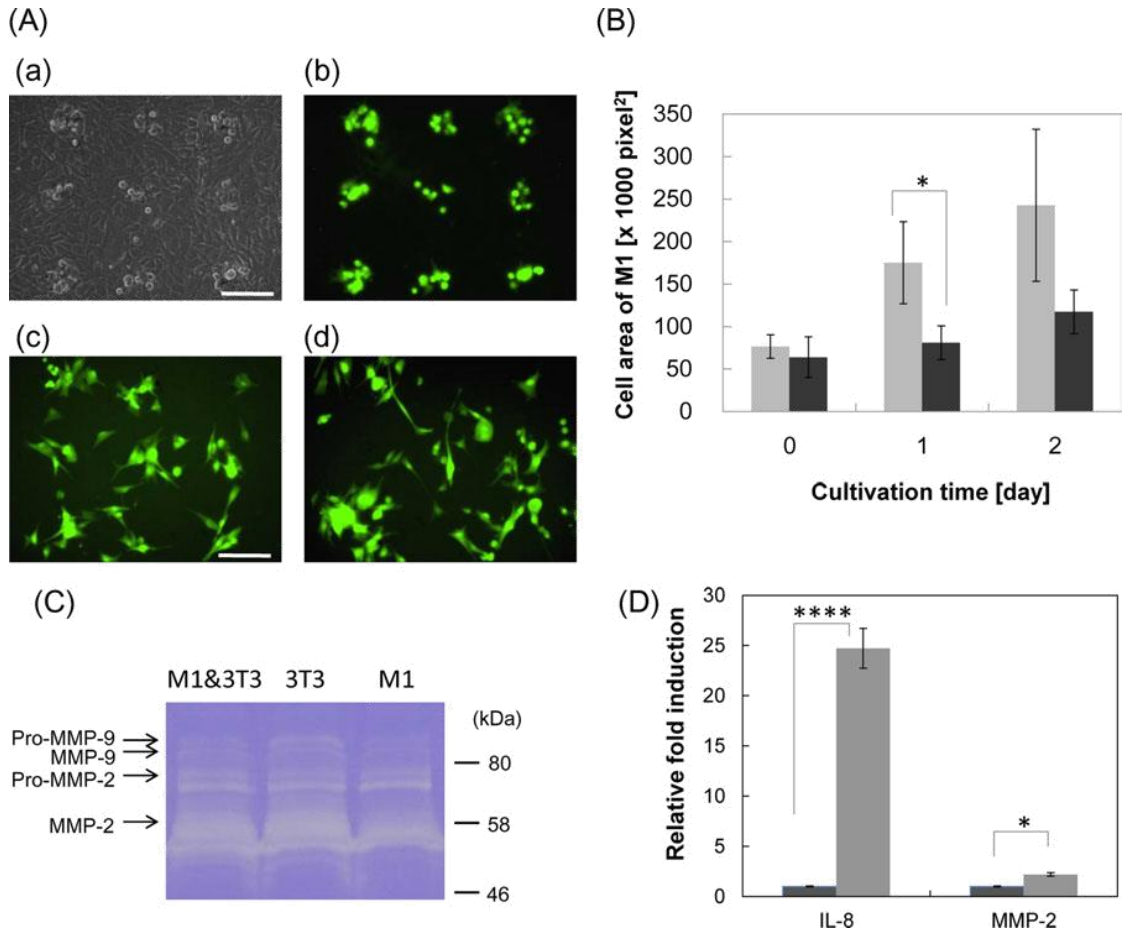

Fig. 3-4. Cell behavior observation and gene expression analysis of M-1 melanoma cultivated in 3D fibroblast-sheet array embedded in collagen. (A) Phase and fluorescent micrographs of magnetically patterned melanoma on the fibroblast-cell sheet. (a) Day 0, phase image; (b) day 0, fluorescent image; (c) day 1 fluorescent image; (d) day 2 fluorescent image. M-1 cells were stained using CellTracker green. Scale bar, 200 μm. (B) Cell area of M-1 magnetically patterned on 3T3-sheet (light gray) and collagen layer (dark gray). Enhanced cell migration observed with the fibroblast-sheet model. (C) Zymographic analysis of the culture supernatant of M-1 array, 3T3-sheet, and co-culture of M-1 patterned on 3T3-sheet with embedded collagen I. (D) IL-8 and MMP-2 gene expression were upregulated when M-1 cells were cultures in 3T3-sheet array (light gray) compared to without fibroblast (dark gray). Gene expression analysis was compared on day 3. $*p < 0.05$, $****p < 1 \times 10^{-4}$ (Student's t test, paired, two-tailed).

3.5. Summary

A three-dimensional (3D) multicellular tumor spheroid culture array has been fabricated using a magnetic force-based cell patterning method, analyzing the effect of stromal fibroblast on the invasive capacity of melanoma. Formation of spheroids was observed when array-like multicellular patterns of melanoma were developed using a pin-holder device made of magnetic soft iron and an external magnet, which enables the assembly of the magnetically labeled cells on the collagen gel-coated surface as array-like cell patterns. The interaction of fibroblast on the invasion of melanoma was investigated using three types of cell interaction models: (i) fibroblasts were magnetically labeled and patterned together in array with melanoma spheroids (direct-interaction model), (ii) fibroblasts coexisting in the upper collagen gel (indirect-interaction model) of melanoma spheroids, and (iii) fibroblast sheets coexisting under melanoma spheroids (fibroblast-sheet model). The fibroblast-sheet model has largely increased the invasive capacity of melanoma, and the promotion of adhesion, migration, and invasion were also observed. In the fibroblast-sheet model, the expression of IL-8 and MMP-2 increased by 24-fold and 2-fold, respectively, in real time RT-PCR compared to the absence of fibroblasts. The results presented in this study demonstrate the importance of fibroblast interaction to invasive capacity of melanoma in the 3D *in vitro* bioengineered tumor microenvironment.

3.6. References

1. Östman A, Augsten M. Cancer-associated fibroblasts and tumor growth-bystanders. Curr Opin Genet Dev 19:67-73, 2009.
2. Kalluri R, Zeisberg M. Fibroblasts in cancer. Nat Rev Cancer 6:392-401, 2006.
3. Pietras K, Östman A. Hallmarks of cancer: interactions with the tumor stroma. Exp Cell Res 316:1324-1331, 2010.
4. Cukierman E, Bassi DE. Physico-mechanical aspects of extracellular matrix influences on tumorigenic behaviors. Semin Cancer 20:139-145, 2010.
5. Wadlow RC, Wittner BS, Finley SA, *et al*. System-level modeling of cancer-fibroblast interaction. PLoS One 4: e6888, 2009.
6. Duyverman AMMJ, Steller EJA, Fukumura D, *et al*. Studying primary tumor-associated fibroblast involvement in cancer metastasis in mice. Nat Protoc 7:756-762, 2012.
7. Flach EH, Rebecca VW, Herlyn M, *et al*. Fibroblasts contribute to melanoma tumor growth and drug resistance. Mol Pharmaceutics 8:2039-2049, 2011.
8. Gallagher PG, Bao Y, Prorock A, *et al*. Gene expression profiling reveals cross-talk between melanoma and fibroblasts: implications for host-tumor interactions in metastasis. Cancer Res 65:4134-4146, 2005.
9. Li L, Dragulev B, Zigrino P, *et al*. The invasive potential of human melanoma cell lines correlates with their ability to alter fibroblast gene expression *in vitro* and the stromal microenvironment *in vivo*. Int J Cancer 125:1796-1804, 2009.
10. Goetz, JG, Minguet S, Navarro-Lerida I, *et al*. Biomechanical remodeling of the microenvironment by stromal caveolin-1 favors tumor invasion and metastasis. Cell 146:148-163, 2011.

11. Kaur P, Ward B, Saha B, *et al*. Human-breast cancer histoid: an *in vitro* 3-dimmensional co-culture model that mimics breast cancer tissue. J Histochem Cytochem 59: 1087-1100, 2011.
12. Khademhosseini A, Langer R, Borenstein J, *et al*. Microscale technologies for tissue engineering and biology. Proc Natl Acad Sci USA 103:2480-2487, 2006.
13. Khetani SR, Bhatia SN. Microscale human liver tissue for drug development. Nat Biotechnol 26:120-126, 2008.
14. Hsiao AM, Torisawa Y, Tung Y-C, *et al*. Microfluidic system for formation of PC-3 prostate cancer co-culture spheroids. Biomaterials 30:3020-3027, 2009.
15. Zervantonakis IK, Hughes-Alford SK, Charest JL, *et al*. Three-dimensional microfluidic model for tumor cell intravasation and endothelial barrier function. Proc Natl Acad Sci USA 109:13515-13520, 2012.
16. Hsu T-H, Xiao J-L, Tsao Y-W, *et al*. Analysis of the paracrine loop between cancer cells and fibroblasts using a microfluidic chip. Lab Chip 11:1808-1814, 2011.
17. Ho WJ, Pham EA, Kim JW, *et al*. Incorporation of multicellular spheoids into 3-D polymeric scaffolds provides an improved tumor model for screening anticancer drugs. Cancer Sci 101:2637-2643, 2010.
18. Markovitz-Bishitz Y, Tauber Y, Afrimzon E, *et al*. A polymer microstructure array for the formation, culturing, and high throughput drug screening of breast cancer spheroids. Biomaterials 31:8436-8444, 2010.
19. Tung Y-C, Hsiao AY, Allen SG, *et al*. High-throughput 3D spheroid culture and drug testing using a 384 hanging drop array. Analyst 136:473-478, 2011.
20. Vinci M, Gowan S, Boxall F, *et al*. Advances in establishment and analysis of three-dimensional tumor spheroid-based functional assays for target validation and drug evaluation. BMC Biol 10:29, 2012.

21. Szot CS, Buchanan CF, Freeman JW, *et al*. 3D *in vitro* bioengineered tumors based on collagen I hydrogels. Biomaterials 32:7905-7912, 2011.
22. Drasdo D, Hoehme S. A single-cell-based model of tumor growth *in vitro*: monolayers and spheroids. Phys Biol 2:133-147, 2005.
23. Fukuda J, Sakai Y, Nakazawa K. Novel hepatocyte culture system developed using microfabrication and collagen/polyethylene glycol microcontact printing. Biomaterials 27:1061-1070, 2006.
24. Sodunke TR, Turner KK, Caldwell SA, *et al*. Micropatterns of Matrigel for three-dimensional epithelial cultures. Biomaterials 28:4006-4016, 2007.
25. Albrecht DR, Underhill GH, Mendelson A, *et al*. Multiphase electropatterning of cells and biomaterials. Lab Chip 7:702-709, 2007.
26. Grier DG. A revolution in optical manipulation. Nature 424:810-816, 2003.
27. Birkbeck AL, Flynn RA, Ozkan M, *et al*. VCSEL arrays as micromanipulators in chip-based biosystems. Biomed Microdevices 5:47-54, 2003.
28. Gensel J, Borke T, Pérez NP, *et al*. Cavitation engineered 3D sponge networks and their application in active surface construction. Adv Mater 24:985-989, 2012.
29. Bazou D, Kearney R, Mansergh F, *et al*. Gene expression analysis of mouse embryonic stem cells following levitation in an ultrasound standing wave trap. Ultrasound Med Biol 37:321-330, 2011.
30. Tanase M, Felton EJ, Gray DS, *et al*. Assembly of multicellular constructs and microarrays of cells using magnetic nanowires. Lab Chip 5:598-605, 2005.
31. Ho VHB, Müller KH, Barcza A, *et al*. Generation and manipulation of magnetic multicellular spheroids. Biomaterials 31:3095-3102, 2010.

32. Ino K, Okochi M, Konishi N, *et al*. Three-dimensional cell culture array using magnetic force-based cell patterning for analysis of invasive capacity of BALB/3T3/v-src. Lab Chip 8:134-142, 2008.
33. Ino K, Okochi M, Honda H. Application of magnetic forcebased cell patterning for controlling cell-cell interactions in angiogenesis. Biotechnol Bioeng 102:882-890, 2009.
34. Koide H, Isaji Y, Okochi M, *et al*. Preparation of L929 cell array by magnetic cell labeling method with unmodified colloidal magnetite nanoparticles for single cell detection of cell response induced by TNF-a. J Chem Eng Jpn 42:290-297, 2009.
35. Okochi M, Takano S, Isaji Y, *et al*. Three-dimensional cell culture array using magnetic forcebased cell patterning for analysis of invasive capacity of BALB/3T3/v-src. Lab Chip 9:3378-3384, 2009.
36. Lee H, Liu Y, Westervelt RM, *et al*. IC/Microfluidic hybrid system for magnetic manipulation of biological cells. IEEE J Solid State Circuits 41:1471-1480, 2006.
37. Saliba A-E, Saias L, Psychari E, *et al*. Microfluidic sorting and multimodal typing of cancer cells in self-assembled magnetic arrays. Proc Natl Acad Sci USA 107:14524-14529, 2010.
38. Zhang K, Zhao L-B, Guo S-S, *et al*. A microfluidic system with surface modified piezoelectric sensor for trapping and detection of cancer cells. Biosens Bioelectron 26:935-939, 2010.
39. Shinkai M, Yanase M, Honda H, *et al*. Intracellular hyperthermia for cancer using magnetite cationic liposomes: *in vitro* study. Jpn J Cancer Res 87:1179-1183, 1996.
40. Owen CS, Sykes NL. Magnetic labeling and cell sorting. J Immunol Methods 73;41-48, 1984.

41. Bauvois B. New faces of matrix metalloproteinases MMP-2 and MMP-9 as cell surface transducers: outside-in signaling and relationship to tumor progression. Biochim Biophys Acta 1825:29-36, 2012.
42. Zigrino P, Kuhn I, Bäeuerle T, *et al*. Stromal expression of MMP-13 is required for melanoma invasion and metastasis. J Invest Dermatol 129:2694-2701, 2009.
43. Derda R, Laromaine A, Mammoto A, *et al*. Paper-supported 3D cell culture for tissue-based bioassays. Proc Natl Acad Sci USA 106: 18457-18462, 2009.
44. Hutmacher DW, Loessner D, Rizzi S, *et al*. Can tissue engineering concepts advance tumor biology research? Trends Biotechnol 28:125-133, 2010.
45. Fischbach C, Chen R, Matsumoto T, *et al*. Engineering tumors with 3D scaffolds. Nat Methods 4:855-860, 2007.
46. Nelson CM, Inman M, Bissel MJ. Three-dimensional lithographically defined organotypic tissue arrays for quantitative analysis of morphogenesis and neoplastic progression. Nat Protoc 3:674-678, 2008.
47. Zigrino P, Nischt R, Mauch C. The disintegrin-like and cysteine-rich domains of ADAM-9 mediate interactions between melanoma cells and fibroblasts. J Biol Chem 286:6801-6807, 2011.
48. Saad S, Gottlieb DJ, Bradstock KF, *et al*. Cancer cell-associated fibronectin induces release of matrix metalloproteinase-2 from normal fibroblasts. Cancer Res 62:283-289, 2002.
49. Koontongkaew S, Amornphimoltham P, Monthanpisut P, *et al*. Fibroblasts and extracellular matrix differently modulate MMP activation by primary head and neck cancer cells. Med Oncol 29:690-703, 2012.

Chapter 4

Effect of vascular formed endothelial cell network on the invasive capacity of melanoma using the *in vitro* 3D co-culture patterning model

4.1. Introduction

Cancer invasion and metastasis are the hallmarks that transform a locally growing tumor into a systematic, metastatic, and life-threatening disease [1]. Cancer metastasis includes multiple steps: tumor cell degradation of the extracellular matrix (ECM) by a family of matrix metalloproteinases (MMPs); migration out of the primary tumor; invasion into blood vessels; adhesion of circulating tumor cells to adhesion molecules of epithelial cells in blood vessels; and degradation of the basement membrane that causes extravasation at the secondary site [1, 2]. Intercellular communication and chemotaxis play key roles in the metastatic process and can occur via direct contact and paracrine signaling between different cell types during tumor cell invasion and metastasis [3]. In particular, vascular endothelial cells that constitute the capillary and blood vessel are deeply involved in adhesion and intravasation. Subcutaneous tumorigenicity of hepatocellular carcinoma cells in nude mice was promoted by vascular

endothelial cells and its invasion/metastasis associated genes were significantly up-regulated [3]. Also, since vascular endothelial cells release numerous cytokines, hormones, and growth factors such as TNF-α [4] and VEGF [5], cultured media of vascular endothelial cells including these secretory factors significantly enhanced proliferation, migration, and invasion of hepatocellular carcinoma cells *in vitro* via activation of PI3K/Akt and ERK1/2 pathways [3]. These pathways stimulate the overexpression of invasion/metastasis associated genes such as MMPs and interleukins (ILs), and these genes promote ECM degradation [6, 7], inflammation [8], angiogenesis [9], and proliferation [10]. Thus, these interactions of tumor cells with vascular endothelial cells via direct contact and paracrine signaling have been investigated.

To study the metastatic process, *in vivo* models have been developed by injection of cancer cells intravenously in mice. These experiments replicate physiological conditions [11]. However, these models are challenging for observation of all aspects of the interaction, and control of cell-cell distance and cross-talk between human cancer cells, human endothelial cells and human tissue parenchyma [12]. Traditional 2D cell culture, which is not representative of the *in vivo* environment, is thus not suitable to evaluate malignant capacity or metastasis-associated gene expression of cancer cell because it cannot mimic physiological factors that provide conditions conducive to cancer metastasis, such as ECM or intercellular interactions [13-15]. The *in vitro* 3D culture platforms in which cells are placed in an ECM for invasion can also provide cell spheroid formation [16] and the distribution of oxygen and metabolic products [17-19]; such models are difficult for visualization of intravasation events in real-time and precise control of cell-cell distance [20, 21]. Although current invasive studies using 3D microfluidic models have been developed to overcome these limitations [5, 22, 23], such studies are largely limited in single cell manipulation and the subsequent analysis of the target cell such as PCR in the closed chamber. Thus, biomimetic cell culture

systems that can control cell-cell distance and evaluate the accurate progression of cancer cells in cell-to-cell and cell-to-ECM interaction are necessary for analysis of genotypic and phenotypic changes.

In response, the cellular micropatterning method can provide useful model systems to investigate intercellular interaction under a combination of multiple controllable biochemical and biophysical microenvironments, coupled with high-resolution real time imaging. Seeking to provide an effective, organized, and practical technique, we have developed a methodology for cell patterning in 3D using magnetic force and magnetite nanoparticles [24-28]. Magnetite nanoparticles embedded in cationic liposomes are used for labeling cells via electrostatic interactions between magnetic cationic liposomes (MCLs) and the target cell membrane [29]. Magnetically labelled cells can then be arranged for observation. Labeling cells with MCL has little effect on cell viability, growth, and differentiation [26]. Utilizing a pin-holder device, the magnetic field of a neodymium magnet is concentrated at the peak of each pin, thus allocating a specific number of cells in a planar fashion according to seeding density, at each point of ECM (collagen or Matrigel). The arrangement of pins, cell seeding density, and cell types can be designed for the evaluation of various cell-cell interactions, and succeed in analyzing the invasion capacity of cancer cells [27, 28]. We have also succeeded in forming a vascular network of magnetically labeled HUVEC that was patterned on the Matrigel angiogenesis model [26], and in genetic analysis the effect of fibroblasts on cancer invasion in direct-interaction, indirect-interaction, and fibroblast sheet interaction models for invasion models [28]. This novel approach has the benefit of cost effectiveness, repeatability, and ease of observation for evaluation of the cell-to-cell interaction including the invasion capacity of cancer cells.

In the present study, the tumor microenvironment mimetic culture array was utilized to observe intercellular behavior of cancer cells in a 3D condition co-cultured with endothelial

cells. The highly metastatic mouse melanoma cell line B16F1 was used as the cancer model, while human umbilical vein endothelial cells (HUVEC) were used as the human endothelial cell model. B16F1 cells were arranged magnetically on vascular-formed HUVEC in ECM, forming cell spheroids (cell aggregates), with a magnetic force-based pin-holder device for observation of the cancer invasion. Since this patterning method was able to control the cell-cell distance between the cancer cell spheroid and HUVEC network, our model was suitable for observation of intercellular interaction via direct contact or paracrine signaling during cancer cell invasion. In addition, gene expression of IL-6, MDR-1, and MMP-9 in the picked-up B16F1 spheroids was used to evaluate the effect of spatial relationship to endothelial cells (HUVEC) on the invasive capacity of melanoma cells. B16F1 spheroids were picked up using a manipulator and analyzed at each distance from HUVEC. Given its ability to perform cell-based assays in the tumor mimetic microenvironment in a simple and objective manner, this system may be useful in understanding the key mechanisms of invasion and drug screening for attenuating metastasis.

4.2. Materials and methods

4.2.1. Cell culture

Mouse melanoma cell line B16F1 (ATCC CRL-6323), human breast cancer cell line MDA-MB-231 (ATCC HTB-26), human cervical cancer cell line Hela (ATCC CCL-2), green fluorescent protein- expressed human gastric carcinoma cell line GCIY-EGFP (RIKEN Cell Bank, Ibaraki, Japan), and human melanoma cell M-1, were grown on 10 cm dishes cultured in Dulbecco's Modified Eagle Medium high glucose (DMEM, Invitrogen, Gaithersburg, MD, USA) to which was added 10% fetal bovine serum (Invitrogen), 0.1 μg/mL streptomycin sulfate, and 100 U/mL potassium penicillin G (Invitrogen).

Human umbilical vein endothelial cells (HUVEC) were provided as frozen cells after primary culture by the supplier (Kurabo, Osaka, Japan). HUVEC were utilized as a model for human endothelial cells, and cultured on 10 cm dishes in HuMedia-EB2 (Kurabo, Osaka, Japan) consisting of 2% fetal bovine serum, 10 ng/ml human epidermal growth factor (hEGF), 1.34 µg/mL hydrocortisone hemisuccinate, 50 µg/mL Gentamicin, 50 ng/mL Amphotericin B, 5 ng/mL hEGF-B, and 10 µg/mL heparin, all supplied by Kurabo. Cells were cultured in a humidified 5% CO_2 incubator at 37 °C.

4.2.2. Preparation of MCL and a pin-holder device

MCL and a pin-holder device were prepared as described in 2.2.2. MCL were prepared using magnetite nanoparticles (Fe_3O_4, mean diameter 10 nm, Toda Kogyo Co., Hiroshima, Japan) and a lipid mixture of TMAG, DLPC, and DOPE at a respective molar ratio of 1:2:2. Magnetite concentration was measured using the potassium thiocyanate method [24].

The pin-holder device was constructed by magnetic soft iron using a wire electrical discharge machine (DIAX-FX10; Mitsubishi Electric Co., Tokyo, Japan) with a cutting wire (diameter: 0.1 mm; Sumitomo Electric Industries, Osaka, Japan) to construct the array of square-pole type pillars. The magnetic field was concentrated on the pillars using an external neodymium disc magnet (50 mm in diameter and 10 mm in height with a surface magnetic induction of 0.38 T; Niruko Factories Co., Shiga, Japan).

4.2.3. Magnetic cell labeling

For magnetic labeling, B16F1 cells were cultured until sub-confluent. DMEM was exchanged for fresh DMEM containing finely dispersed MCL at 100 pg-magnetite per cell for 2 h incubation. Cells were then washed twice with PBS to remove non-introduced residual

MCL. Magnetically labeled cells were then collected with 0.25% trypsin-EDTA (Gibco, Carlsbad, CA, USA). To evaluate the toxic effect on the cell growth of the magnetically labeling using MCL, B16F1 cells with or without magnetic labeling were grown on 10 cm dishes cultured in DMEM at seeding densities of 2×10^5 cells/dish, and the living cell numbers were counted by trypan blue exclusion every 24 hours.

4.2.4. Preparation of B16F1 melanoma spheroid 3D cell culture array with HUVEC network

Collagen mixture was prepared by mixing a 7:2:1 volume ratio of ice-cold collagen solution, 0.3% Cellmatrix Type I-A (Nitta Gelatin, Osaka, Japan) with 5× DMEM and 10× sterile reconstitution buffer (2.2 g $NaHCO_3$ in 100 mL of 0.05 M NaOH and 0.2 nM 2-[4-(2-hydroxyethyl)-1-piperazinyl]ethane sulfonic acid (HEPES)) as described in the instructions. Gas-permeable tissue culture dishes (hydrophilic lumox dish, 35mm, SARSTEDT, Nümbrecht-Rommelsdorf, Germany) were used for the 3D culture array.

First, a thin layer of Matrigel (100 μl) (Becton, Dickinson and Company, Cedex, France) was spread on each dish with a cell scraper. Then, HUVEC stained with CellTracker orange (CMTMR; Molecular Probes, Eugene, OR, USA) were plated on each dish at seeding density of 3×10^5 cells/dish, and incubated overnight for network formation. The cancer cells were magnetically labeled with MCL and stained with CellTracker green (CMFDA; Molecular Probes, Eugene, OR, USA) in DMEM. For cell arrangement, the neodymium disc magnet, the pin-holder device, and the gas-permeable tissue dish with networked HUVEC were arranged in order (**Fig. 4-1**), and 2.5 ml suspension of the cancer cells in DMEM at seeding densities of 7.2×10^4 cells/ml (average 10 cells/spot, 250 μm interval pin-holder); 2.16×10^4 cells/ml (average 1.5 cells/spot, 250 μm interval pin-holder), 2.16×10^4 cells/ml (average 50 cells/spot, 1000 μm interval pin-holder) were inoculated onto the dish, followed by 30 min incubation.

Then, after removing supernatant medium, 1 ml collagen mixture was overlaid, and the dish was removed from the pin-holder device and magnet. The dish was returned to the incubator for another 30 min for solidification of collagen, followed by the addition of 1 ml DMEM.

4.2.5. Cell observation

Cells in the 3D cell array were observed via time-lapse monitoring through phase microscopy (Model IX81, Olympus Co., Tokyo, Japan). Analysis of images was performed by image analysis software (MetaMorph, Universal Imaging Co., Downingtown, PA, USA) to calculate the length or perimeter of cancer cell spheroids and the distance between cancer cell spheroid and networked HUVEC. The invasion of B16F1 cells to HUVEC network were analyzed using a confocal microscope (A1Rsi-N, Nikon, Tokyo, Japan) and confocal image analysis software (NIS-Elements, Nikon, Tokyo, Japan).

4.2.6 Non-distractive and automatic analysis of cancer invasion of HUVEC network

The length, perimeters, and centroids of cancer cell spheroids, which were labeled with CellTracker green (CMFDA; Molecular Probes) and co-cultured with HUVEC, were calculated by image analysis software (MetaMorph) from the green-fluorescent images, as mentioned in 4.2.5. Similarly, the centroids of vascular-formed HUVECs, which were labeled with CellTracker orange (CMTMR; Molecular Probes), were calculated from the orange-fluorescent images. Then, we calculated the all distances among the spheroid-centroids and HUVEC-centroids, and compared length or perimeter of the spheroid and distance from the nearest HUVEC. The “distance of starting elongation” was calculated from intersection point of the one-phase decay curve and the average + 3SD of length or perimeter of mono-cultured cancer spheroid by GraphPad software (GraphPad Software Inc., San Diego, CA, USA).

4.2.7 Gene expression analysis

The B16F1 cells co-cultured with HUVEC and in isolation, were collected from the 3D cell array, and treated with 0.033% collagenase. Cells were washed with PBS, counted by fluorescent microscopy, and lysed using lysis enhancer and resuspension buffer from CellsDirect One-step qRT-PCR kits (Invitrogen). Real-time RT-PCR assays were conducted on an ABI StepOne Real Time PCR Systems, using SYBR Green RNA 1step kit (Applied Biosystems, Branchburg, NJ, USA). Primers were purchased from Greiner Bio One, Frickenhausen, Germany. The sequences of B16F1 specific primers for mouse mRNA are listed in **Table 4-1**. The comparative threshold cycle (Ct) method was used to quantify gene expression in each sample. Normalization of gene expression was performed using GAPDH as a reference gene, and all data was expressed as a ratio to the reference sample of B16F1 monoculture. In order to analyze the target cell expression, we collected the cells using a micromanipulator (CellTram vario 5176, Eppendorf, Humberg, Germany). One spheroid collected by a micro manipulator was suspended into a lysis buffer directly, and the expression ratio in each spheroid was analyzed as described above.

4.3. Results

4.3.1. Effects of ECM mimetic gels on cell morphology

To construct the *in vitro* 3D cell culture array to observe the invasive capacity of B16F1 melanoma cell spheroids co-cultured with the HUVEC network, cell morphological behaviors of HUVEC and B16F1 were investigated. **Fig. 4-2** displays images of B16F1 and HUVEC cultured using two types of ECM-mimetic gel containing collagen type-I and Matrigel. The B16F1 were plated in 3D cellular array monoculture in collagen gel, with or without a base layer of Matrigel, as well as images from 2D culture. B16F1 cells were magnetically labeled

using MCL, and then patterned in ECM mimetic gel. Since there was no significant difference regardless of MCL-labeling in B16F1 cell proliferation (**Fig. 4-2A**), MCL labeling has little effect on cell-to-cell interaction [27, 28]. After 48 h of culturing, B16F1 cells in monoculture, patterned in collagen gel at seeding densities of 7.2×10^4 cells/ml (10 cells/spot, 250 μm interval pin-holder), formed spheroids at each locus (**Fig. 4-2B**). Although, B16F1 was highly invasive melanoma cells, the cells remained in compact spheroids, and showed no signs of invasive behavior such as elongation and invadopodia. In contrast, B16F1 showed spindle formation in the traditional 2D culture, which vastly differ from the spheroid formation *in vivo*. Thus, a more biomimetic microenvironment would be necessary to observe the invasive characteristics of malignant melanoma.

When B16F1 cells were patterned in collagen gel with a Matrigel base layer, B16F1 formed multicellular spheroids with satellites of invadopodia. Invadopodia contain many type of proteases, stress fibers and adhesion proteins, indicating that their main function is to provide traction for invasive cancer cells [30]. Also, a Matrigel base layer induced the vascular-like networks of HUVEC which were plated at seeding density of 3×10^5 cells/dish, morphology indicative of angiogenesis.

However, HUVEC showed spindle formation on a collagen base layer and in 2D culture (**Fig.4-2C**). It was confirmed that Matrigel provides several angiogenesis factors such as VEGF or bFGF [31]. Hence, micropatterning in a collagen gel layer with Matrigel was suitable to observe invasive associated interaction of malignant melanoma cells with vascular endothelial cells.

4.3.2. Melanoma cell behavior in 3D co-culture array with HUVEC

Fig. 4-3 shows the effect of the HUVEC network on morphological behaviors of melanoma in a biomimetic 3D co-culture array that was constructed on a Matrigel base layer

in collagen type-I gel. HUVEC were plated on tissue culture dishes coated with Matrigel and allowed to network at 24 h, and then magnetically labeled B16F1 cells were arrayed over-top in networked HUVEC and set in collagen gel. We also have adjusted the patterning interval and the seeding B16F1 cell number in a spheroid for evaluation of the invasive capacity. **Fig. 4-3A**-**4-3E**, illustrate time-lapse images at varying B16F1 seeding densities and patterning interval: average 1.5 cells/spheroid with 250 μm patterning (**Fig. 4-3A**), average 10 cells/spheroid with 250 μm intervals (**Fig. 4-3B, 4-3E**), average 50 cells/spheroid with 1000 μm intervals (**Fig. 4-3C**), and 0 cells/spheroid (**Fig. 4-3D**), respectively.

From **Fig. 4-3A**-**4-3C** and **4-3E**, clear invasive behaviors of B16F1, such as cell elongation along to the HUVEC network, were observed in 3D co-culture with HUVEC in every seeding density and patterning interval. It seems that B16F1 that were close to HUVEC have aggressively elongated and invaded according to the HUVEC network, while B16F1 cells distant from HUVEC remain in compact spheroids (**Fig. 4-3A, 4-3B, 4-3E**). The white arrows indicate the B16F1 cells that have not only formed invadopodia but also completely invaded the HUVEC network. The B16F1 spheroids that were close to HUVEC migrated along to the pre-existing vascular network (yellow arrows).

In contrast, melanoma spheroids did not show such aggressive invasive behavior in monoculture (**Fig. 4-2B**). The intercellular junction of HUVEC network became more weak, and some networks were broken in the B16F1 invasion in co-culture array (**Fig.4-3A**-**4-3C**), compared with that in monoculture of HUVEC network (**Fig.4-3D**). The secretion factors of HUVEC had up-regulated the invasion/metastasis associated gene expressions in cancer cells, including MMP-9 [3]. It seemed that the intercellular adhesion and extracellular matrix was degraded by the cancer-produced proteases. It was shown that cancer cells close to vascular endothelial cell had invaded, and the malignancy progressed rapidly.

However, since the single cancer cell spots may not show the activation of migration to

the HUVEC network via cancer cell-to-cancer cell adhesion such as N-cadherin signaling [32], the single cell patterning would be not suitable to evaluate the aggressive invasion of cancer cell. Also, since two morphological changes within a spheroid, such as dispersion from the spheroid or cell elongation, was observed in the big melanoma spheroids of 50 cells, (**Fig. 4-3C**; middle), it was difficult to characterize the factors relating to such melanoma invasive capacity (direct contact or paracrine signaling). We adopted 10 cells for the cell number in a spheroid to observe invasive behavior. In addition, since the average spacing between strands in the HUVEC network was 350 μm in **Fig. 4-2C**, we adopted a 250 μm patterning interval, which can set variation in distance from HUVEC for co-culture array patterning.

To investigate the invasion of B16F1 cells to the HUVEC network, confocal image analysis of B16F1 cells surrounding the HUVEC network was obtained. **Fig. 4-4** shows the confocal images of HUVEC network before (**Fig. 4-4A**-**4-4C**) and after 24 h co-culture with B16F1 array at 10 cells/spheroid with 250 μm interval (**Fig. 4-4D**-**4-G**). In the sectional view, network formation of HUVEC was observed (**Fig. 4-4B, 4-4C**). In contrast, invasion of B16F1 cells along to the HUVEC network was observed after co-culture (**Fig. 4-4E**-**4-4G**). It was demonstrated that B16F1 that were close to HUVEC have–invaded the endothelial network, while B16F1 cells distant from HUVEC remain in compact spheroids.

To evaluate the invasion of the other cell lines to the HUVEC network, 4 another cancer cell lines were co-cultured with HUVEC network in average 10 cells/spheroid with 250 μm intervals (**Fig. 4-5A**). As a result, the cancer cell spheroids that were close to HUVEC have aggressively elongated and invaded according to the HUVEC network, than that of spheroids distant from HUVEC and mono-cultured spheroids. These results were demonstrated that HUVECs were affected the invasive behavior of the other cancer cell lines.

To evaluate these invasive elongations of cancer spheroids, the length of cancer cell spheroids was analyzed. Since the elongated cancer spheroid reflects the activation of

invasiveness or the high invasive capacity of the cancer cells, we calculated the length of a cancer spheroid from the time-lapse image to quantify the invasive capacity of the cancer cell. **Fig. 4-6** shows the length of B16F1 spheroids in each distance from the co-cultured HUVEC network, in which B16F1 cells were set to 10 cells/spheroid at 250 μm interval. A plot of distance 0 in **Fig. 4-6** represents a length of B16F1 spheroid adhered to HUVEC directly, and the others, which did not adhere to HUVEC. After culturing for 24 h, B16F1 spheroids were elongated in the proximity of the HUVEC network in co-culture conditions, and the length was clearly increased within an 80 μm distance from HUVEC regardless of B16F1-to-HUVEC adhesion, while the length of B16F1 spheroids was slightly changed in monoculture. On the other hand, the length of B16F1 80 μm far from HUVEC did not significantly differ from the monoculture. Therefore, it was shown that a vascular network of endothelial cells crucially affected invasive behavior of cancer cells according to the distance to cancer cells by the secreted soluble factors, as well as by direct interaction.

For high-throughput evaluation of these invasive behaviors, we constructed an image analysis-based analysis system to evaluate the invasive morphology of cancer spheroids automatically and non-destructively. We focused on the perimeter of cancer spheroids, which was one of invasive parameter, and calculated the parameter by the analysis system from the fluorescent images of co-cultured cancer spheroids with HUVEC network. As a result, we successfully evaluate the cancer elongation in 4.5 ± 3.6 % of error ratio (data not shown). The "distance of starting elongation", which were intersection point of the one-phase decay curve and the average + 3SD of the perimeter of mono-cultured cancer spheroid, was 100.6 μm in MDA-MB-231, 63.5 μm in Hela, 57.6 μm in M-1, and 37.0 μm in GCIY-EGFP, respectively (**Fig. 4-7**). Therefore, we could evaluate the affect from vascular network of endothelial cells on invasive behavior of cancer cells automatically and non-destructively, and showed that the affect endothelial cells was different among each cancer cell line.

4.3.3. Gene expression of melanoma cells in 3D co-culture array with HUVEC

To observe the effect on tumor associated gene expression of B16F1 melanoma (IL-6, MMP-9 and MDR-1) patterned on the HUVEC network, real-time PCR analysis was investigated. IL-6 and MMP-9 promote invasion and metastasis of cancer cells via accelerating ECM degradation, inflammation, angiogenesis and proliferation [6-10]. MDR-1 is a gene that leads to the production of ATP-driven efflux transporter Pgp-170, the most common cause of multidrug resistance in many types of solid and hematological human cancers [33]. It is known that these gene expressions are stimulated by paracrine signaling such as TNF-α [4] or direct contact [34]. **Fig. 4-8** shows that the relative expressions of IL-6, MMP-9 and MDR-1 in co-cultured B16F1 with HUVEC compared to that in B16F1 monoculture.

First, we compared the average expression of whole B16F1 cells co-cultured with HUVEC in a culture dish to that without HUVEC (**Fig. 4-8A**). To collect whole B16F1 cells, B16F1 were treated with collagenase after a 24 h culture with or without HUVEC. The mRNA expressions of collected B16F1 cells were analyzed by real time RT-PCR using specific primers for mouse mRNA to detect the B16F1 expression without any separation steps of B16F1 from co-existing HUVEC, and glyceraldehyde-3-phosphate-dehydrogenase (GAPDH) mRNA level was used as the reference. GAPDH levels in co-culture and in monoculture were relatively identical, and MMP-9 levels also did not significantly differ from B16F1 monoculture. In contrast, when B16F1 co-cultured with HUVEC, IL-6 and MDR-1 production was 7-fold and 4-fold higher, respectively. It was shown that the intracellular interaction with vascular endothelial cells was important for the progression of malignancy in cancer cells.

Next, since the invasive elongation of B16F1 spheroids was increased along to the

distance from HUVEC (**Figs. 4-3, 4-4, 4-6**), we picked up the B16F1 cell spheroids using a micromanipulator, and compared the gene expressions (**Figs. 4-8B, 4-8C**). We could collect 6-10 cells from a B16F1 spheroid, respectively, and analyzed the mRNA expressions of all collected cells. The distance between B16F1 and HUVEC was calculated from the fluorescence images after 24 h co-culturing. **Figs. 4-8B and 4-8C** showed that the relative expression levels of a co-cultured B16F1 spheroid in each distance from HUVEC, compared to that of B16F1 monoculture. The mRNA expression levels of IL-6, MDR-1 and MMP-9 in B16F1 increased in inverse proportion to the distance of the HUVEC network, and these expressions were increased by 5, 3, and 2-fold, respectively, in the B16F1 close to HUVEC (within 80 μm distance) compared to that far from HUVEC (over 80 μm distance) (**Fig. 4-8**). This 80 μm distance from HUVEC was the distance that increased invasive morphology of B16F1 cells in **Fig. 4-6**. Since IL-6 and MMP-9 are important for invasion [6-10], the increase of these gene expressions was comparable to the invasive cell behaviors that exist within 80 μm from HUVEC displayed in **Fig. 4-6**. These gene expression levels of cytokines related to tumor invasion, and the gene expression level of drug-efflux transporter related to drug resistance in melanoma, indicating that the proximity to vascular endothelial cell enhanced melanoma malignancy. Therefore, the melanoma spheroid arrays co-cultured with vascular endothelial network on the Matrigel base layer with embedded collagen type-I demonstrate the importance of vascular network in invasive cell behaviors in bioengineered tumor microenvironments.

4.4 Discussion

Microengineering techniques for cellular analysis are gaining momentum as powerful tools to study cellular events for tissue-engineering and medical applications. In the field of cancer treatment, discovery of key factors affecting cell invasion and metastasis would be

possible using *in vitro* 3D cell culture models. Recently, *in vitro* 3D cell culture systems that mimic tumor microenvironments have attracted much attention for deepening understanding and hastening the development of treatment, since these models contain the structural architecture necessary for studying cellular interactions. Such systems possess distinct advantages over conventional cell culture systems, including the ability to produce 3D architecture with controlled and repeatable spatial relationships between the cells in ECM. Therefore, applying tissue-engineering concepts and microengineering techniques in these systems would be expected to bridge the gap between two-dimensional studies and *in vivo* animal models [35].

In the present study, we have investigated the effect of a vascular formed endothelial cell network on the invasive capacity of melanoma in a biomimetic microenvironment using the *in vitro* 3D co-culture patterning model (**Fig. 4-1**). It was demonstrated that through interactions of various types of cancer cell lines with vascular endothelial cells, genetic expression orchestrating tumor invasion was enhanced (**Figs. 4-3-4-7, 4-8A**). Thus, a vascular endothelial network with cellular and ECM components plays a crucial role in regulating the process of tumor invasion. It can be deduced that traditional 2D cultures or even 3D monocultures without ECM or vascular endothelial cells give inaccurate representations of cancer invasion or genetic progression than that of the natural tumor microenvironment.

In individual cancer cell spheroids, it was clearly shown that the proximity to a vascular endothelial network accelerated the cancer invasive behavior and tumor-associated gene expression (**Fig. 4-3-4-7, 4-8B, 4-8C**). It is known that numerous kinds of cytokines including TNF-α secreted by HUVEC [4] have regulated malignant capacity and drug resistance of cancer cells [3, 34, 36-38]. However, since most cancer cells also overproduce various kinds of proteinase that promote digestion of ECMs and cytokines in the cancer microenvironment [39-41], the local concentration of these cytokines secreted by HUVEC should be decreased

according to the distance from the vascular network. Therefore, we considered that the malignant changes of invasive behavior and gene expression of B16F1 were caused by the difference in exposure amount of cytokines according to the distance from HUVEC.

Also, since intercellular adhesion regulates cell growth, motility, and angiogenesis via N-cadherin or PKC signals [32, 34], many researchers have been focused on adhesion-mediated malignancy within tumors to understand the mechanism of metastasis. In this research, MDR-1 expression in spheroids adhered to HUVEC was higher than that of non-adherent spheroids within 80 μm distance from HUVEC (**Fig. 4-9**), since MDR-1 expression has been stimulated via both paracrine signaling such as TNF-α and cell-to-cell adhesion [34, 37]. In contrast, there were no significant differences of IL-6 and MMP-9 expressions in the adhered spheroids to HUVEC were comparable to that in non-adherent spheroids within 80 μm distance from HUVEC (**Fig. 4-9**), since these expressions were stimulated by paracrine signaling such as TNF-α [3, 36-38]. Thus, applying genetic engineering techniques such as fluorescent protein linked with the adhesion molecule in these systems, the cellular micropatterning method can provide useful models to investigate paracrine signaling and intercellular adhesion with high resolution real time monitoring. Our micropatterning method could clearly detect the increases of IL-6 expressions in individual B16F1 melanoma spheroids in each distance from HUVEC (**Fig. 4-8B, 4-8C**), while the average expression of whole B16F1 cells co-cultured with HUVEC showed no significant increase with that without HUVEC (**Fig. 4-8A**). Our co-culture model enables the observation of local changes in cell morphology as well as their gene expressions and leads to understanding of the cancer microenvironment.

In addition, our automatically and non-destructive analysis system could observe the change of cancer spheroid elongation among various cell line, which had different invasive potentials. MDA-MB-231 was known as a highly metastatic cell line, and invased into

circulation within 30 days in mice model [42]. Hela and GCIY-EGFP also invased into circulation about 8weeks and 2-3 months in mice model, respectively [43, 44]. Although, the "distances of starting elongation" in this study were higher in order to this invasive potential of the cancer cell lines (MDA-MB-231 > Hela > GCIY-EGFP), this result would show that our co-culture model might have potential to observe the *in vivo* malignancy of cancer cells.

Tumor cell behavior is regulated by its intrinsic properties as well as by its microenvironment, which comprises resident endothelial cells, ECM, and fibroblasts [28]. The fibroblasts involved in primary tumor formation and invasion are referred to as cancer associated fibroblasts (CAFs), we had evaluated the morphological and genetic interactions of melanoma in co-culture patterning model with fibroblasts using pin-holder device in our previous paper [27, 28]. However, the elongation of the B16F1 melanoma spheroids was changed only slightly in co-culture array with line-patterned normal human dermal fibroblasts (NHDFs). Line patterning devise was newly fabricated (**Fig. 4-10A**). The magnetically labeled NHDF was inoculated on a thin layer of Matrigel for the line patterning at seeding density of 3×10^5 cells/dish (as same as the cell seeding density of HUVEC), and co-cultured with magnetically labeled B16F1 array at seeding density of 10 cells/spot (**Fig. 4-10**). Although we observed the active elongation and invasion of melanoma spheroids within an 80 μm distance from HUVEC, the B16F1 melanoma spheroids co-cultured with NHDF did not almost move. In addition, Cedric Gaggioli *et al*. had reported that the squamous cell carcinoma (SCC) moved in groups and SCCs were always close to fibroblasts, appearing to move 'along' them [45]. The SCCs was activated the invasive capacity by the adhesion signaling such as integrin α3 and α5, indicating that cancer cells were passively activated the invasive capacity by CAFs. Therefore, the activation of the B16F1 invasiveness in our report suggested that HUVEC played a crucial role in cancer invasion than the surrounding

fibroblast, and our co-culture model with HUVEC was suitable for the observation of cancer invasive capacities than other co-culture models using the fibroblasts.

Most conventional 3D invasion assays, such as microfluidic models or microwell platform analysis, have the complexity of building platforms, and those models have difficulty in cell manipulation for subsequent biological analysis. Therefore, many cancer and molecular biologists do not widely use 3D culture techniques for invasion assay and practical drug screening models [41]. On the other hand, our methodology is simple to construct, easy to handle and uses generally available cell culture dishes for cell patterning and culture. For analysis, manipulation of the target cell spheroids from the 3D spheroid array could be performed simply and directly using a micromanipulator. Thus, the 3D cell culture array has remarkable advantages for practical invasion model and several biological analysis of target cell. In addition, since 3D cell patterning can arbitrarily design spatial position of the target cells, it is effective to observe the various interactions of cancer cells with the co-existent somatic cells in the tumor environment. The spatial control of magnetically labeled HUVEC is also possible by magnetic patterning of HUVEC in network formation [26], which leads to the development of a vascular networking model in a larger spheroid. Also, the co-existence of stromal spheroids is possible by mixing with the collagen gel or laying the cellular sheet [28], which leads to further investigation of intercellular interactions, such as among cancer-vascular-stromal cells mimicking the progression of the tumor microenvironment. This *in vitro* 3D magnetic force-based cellular array technique is a functional tumor model that can be used in the future to elucidate the invasive capacity of tumor cells as well as their pharmacological responses.

In conclusion, *in vitro* 3D magnetic force-based cell patterning method is a highly applicable technique for analysis, diagnostics, and drug screening in a biomimetic microenvironment.

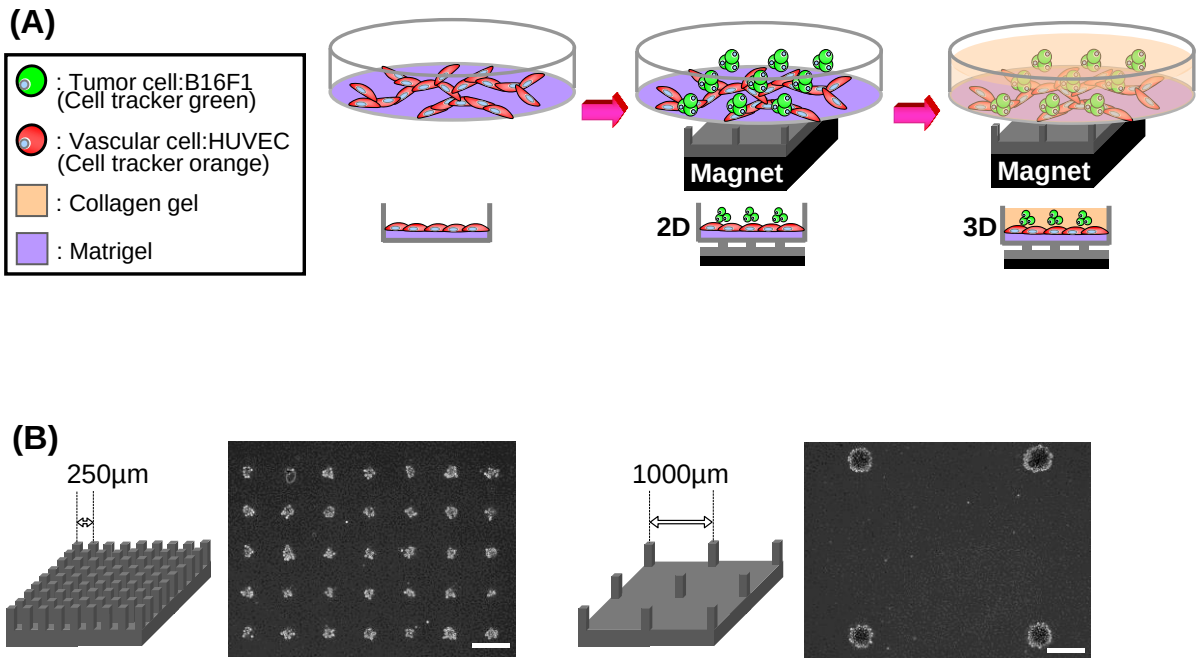

Fig. 4-1. Magnetic force-based cell patterning using the pin-holder device for observation of invasive capacity of B16F1 melanoma associated with HUVEC. (A) Schematic diagram for fabrication of the 3D cell culture array. HUVEC was inoculated on a thin layer of Matrigel for network formation. The cell culture dish was placed on the pin-holder device which is placed on the neodymium magnet. The B16F1, magnetically labeled with MCL, were patterned by magnetic force. The patterned cells were then embedded with collagen gel. (B) Phase microscopic images of magnetically patterned B16F1 melanoma cells using the pin-holder device with different spacing. The center-to-center distance of the pin-holder device was 250 μm (left) or 1000 μm (right) and the cells were arranged on pins according to magnetic force. Scale bars are 100 μm.

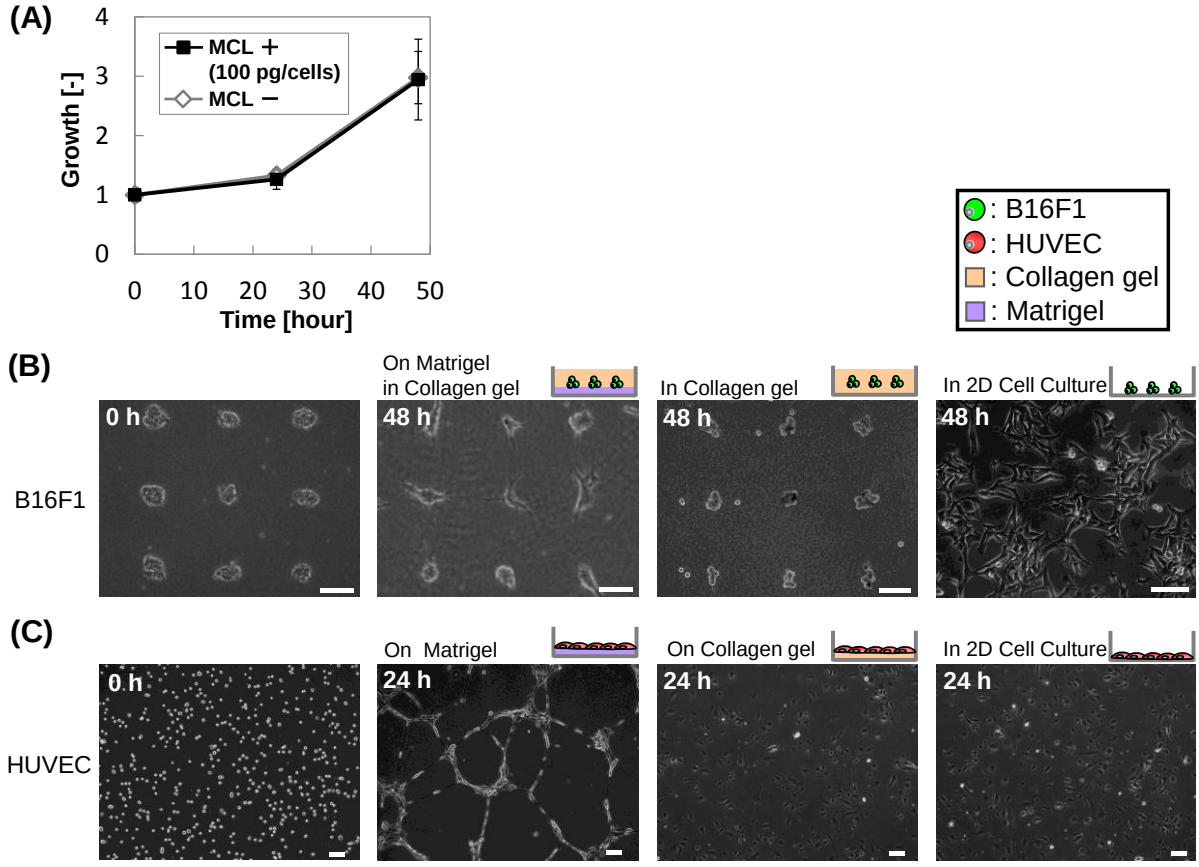

Fig. 4-2. Phase microscopic images of B16F1 melanoma and HUVEC monoculture in 3D and 2D. (A) Growth curve of B16F1 with or without magnetic cell labeling by MCL in 2D cell culture. B16F1 with or without magnetic cell labeling were grown on 10 cm dishes cultured in DMEM at seeding densities of 2×10^5 cells/dish, and the living cell numbers were counted by trypan blue exclusion at each time points. (B) Phase microscopic images of B16F1 cells. Magnetically pattered B16F1 at seeding densities of 7.2×10^4 cells/ml (10 cells/spheroid, 250 μm interval pin-holder) with or without a layer of Matrigel was embedded with overlaid collagen (3D culture). The 2D culture was performed in comparison. (C) Phase microscopic images of HUVEC cells plated on Matrigel with or without a layer of Matrigel were embedded with overlaid collagen (3D culture) at seeding density of 3×10^5 cells/dish. The 2D culture was performed in comparison. Scale bars are 100 μm.

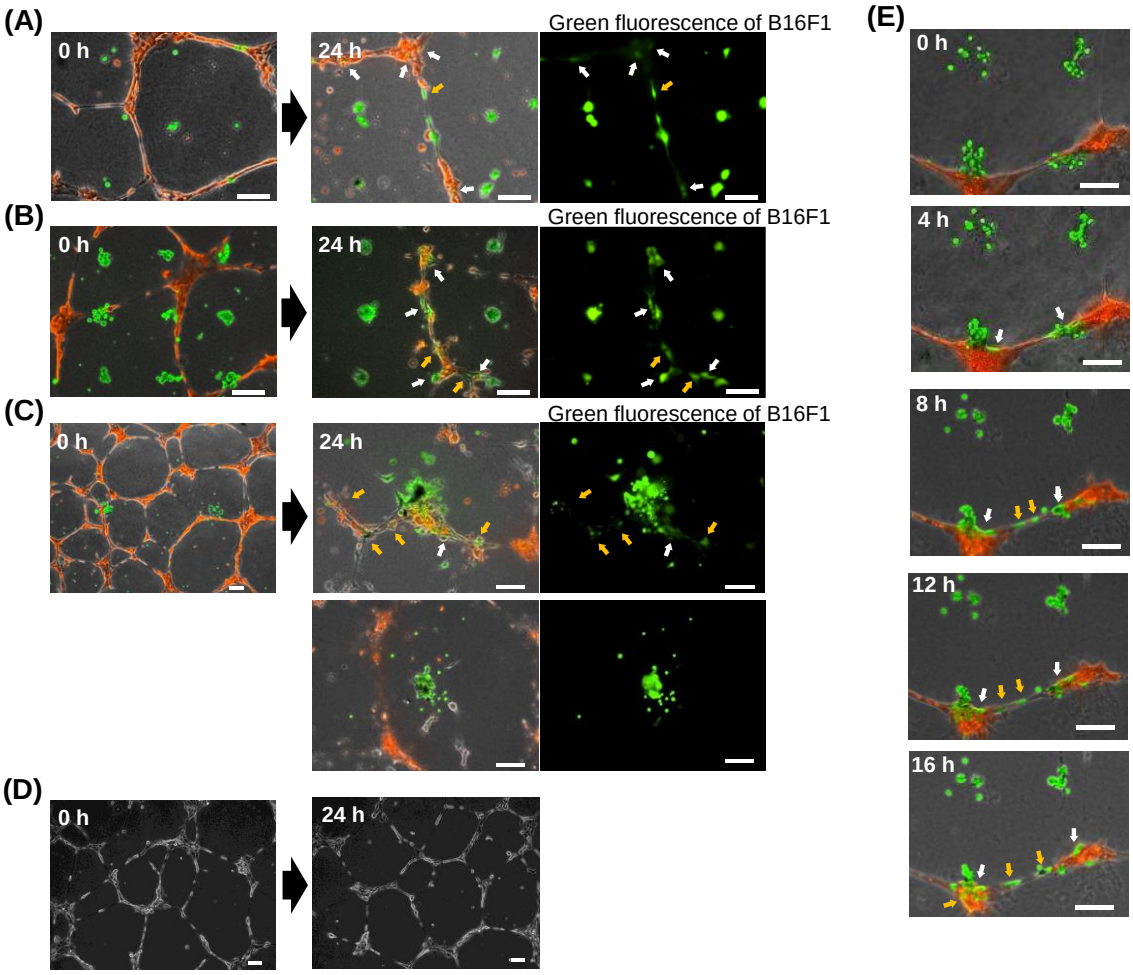

Fig. 4-3. Fluorescent microscopic images of B16F1 (green) in 3D cell culture array with HUVEC network (red). Magnetically labeled B16F1 cells were arrayed at varying seed-densities over HUVEC network: 2.16×10^4 cells/ml (A: average 1.5 cells/spheroid, 250 μm interval pin-holder); 7.2×10^4 cells/ml (B: average 10 cells/spheroid, 250 μm interval pin-holder) 2.16×10^4 cells/ml (C: average 50 cells/spheroid, 1000 μm interval pin-holder); and 0 cells/ml (D). Time-lapse images were taken for three plates on 0 h and after 24 h (A-D). (E) The co-culture array was fabricated at B16F1seeding density of average 10 cells/spot, and time-lapse images were obtained at 4 h intervals from 0 h to 16 h. White arrows highlight B16F1 cells that have invaded the HUVEC network. Yellow arrows indicate the B16F1 that have spread along to the HUVEC network. Scale bar: 100 μm.

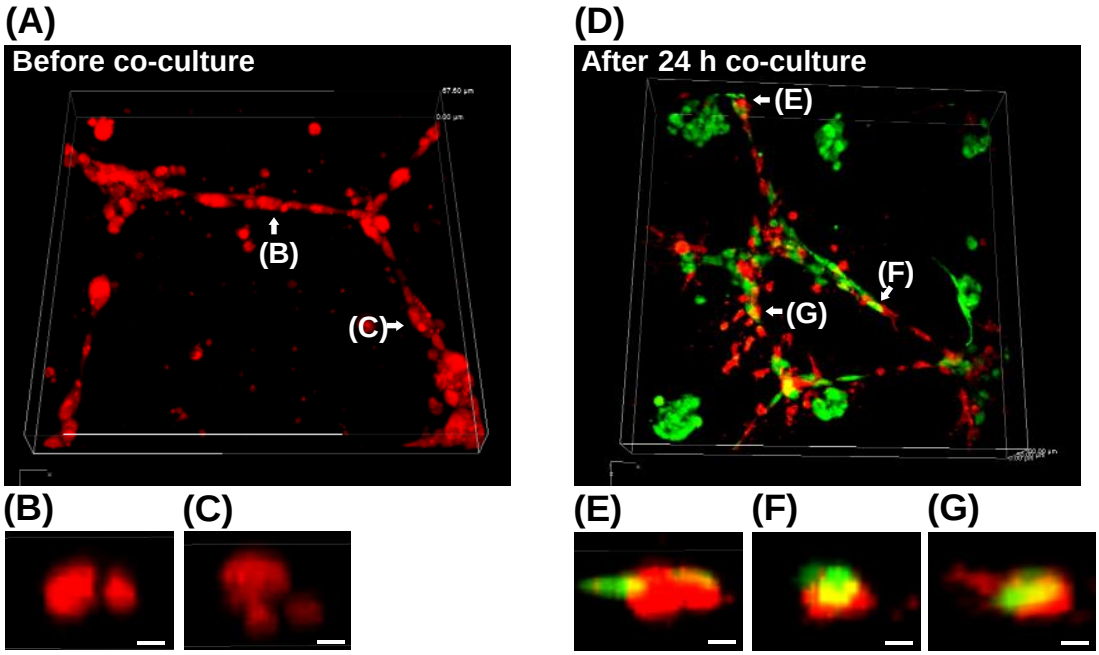

Fig. 4-4. Confocal microscopic images of B16F1 (green) invasion of HUVEC network (red). Magnetically labeled B16F1 cells were arrayed at 10 cells/spheroid with 250 μm interval over the HUVEC network, and images surrounding the HUVEC network were taken before (A-C) and after the 24 h co-culture (D-G). The representative sectional view of the HUVEC network before co-culture with B16F1 (B, C) and invasive points of B16F1 after a 24 h culture (E-G). Scale bar: 10 μm.

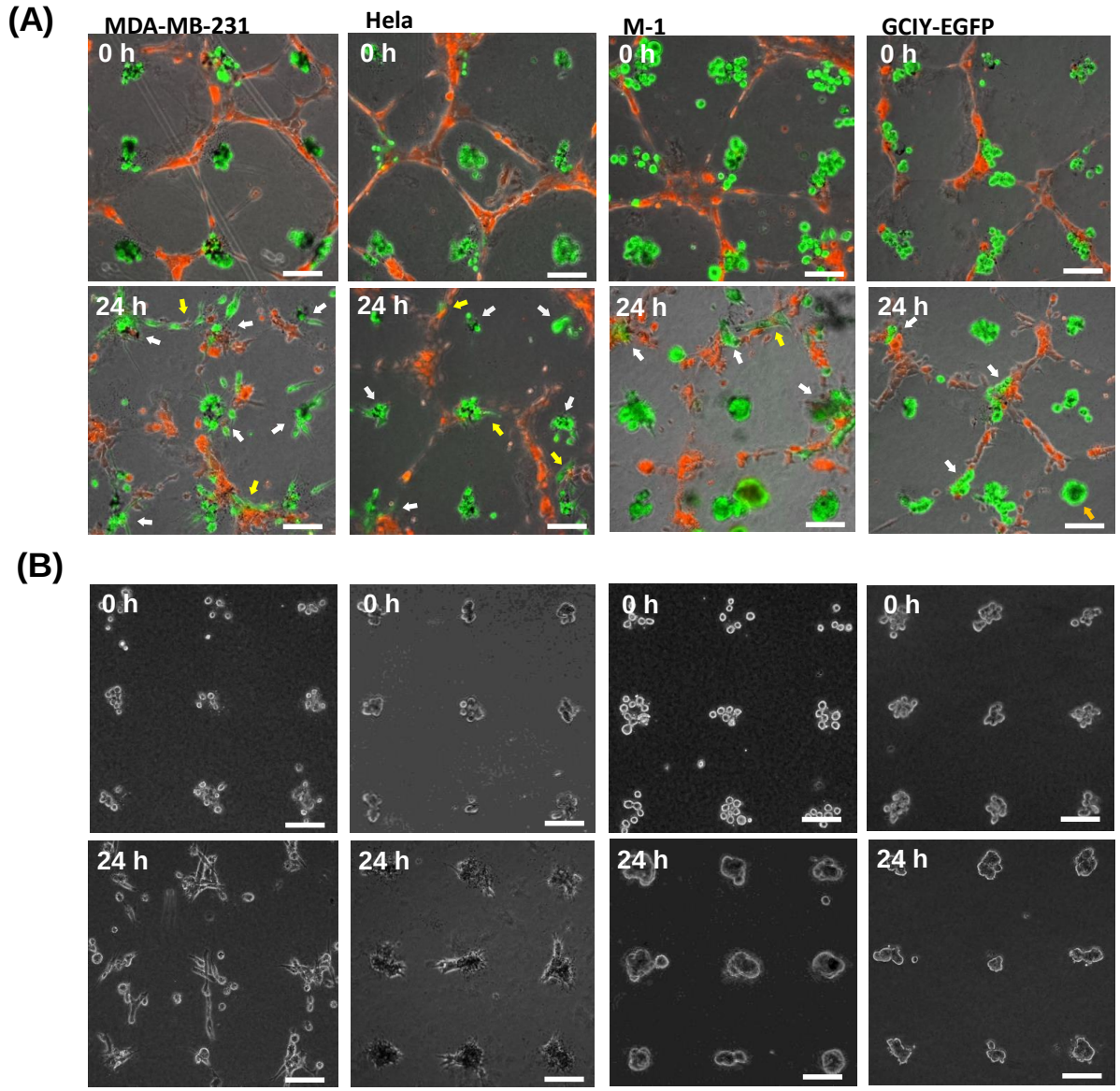

Fig. 4-5. Fluorescent microscopic images of 4 cancer cell lines (green) in 3D cell culture array with HUVEC network (red). Magnetically labeled 4 cancer cell lines (MDA-MB-231, Hela M-1 GCIY-EGFP) were arrayed at varying seed-densities over HUVEC network at 7.2×10^4 cells/ml (average 10 cells/spheroid, 250 μm interval pin-holder). Time-lapse images were taken on 0 h and after 24 h with (A) or without HUVEC (B). White arrows highlight cancer cells that have invaded the HUVEC network. Yellow arrows indicate the cancer cells that have spread along to the HUVEC network. Scale bar: 100 μm.

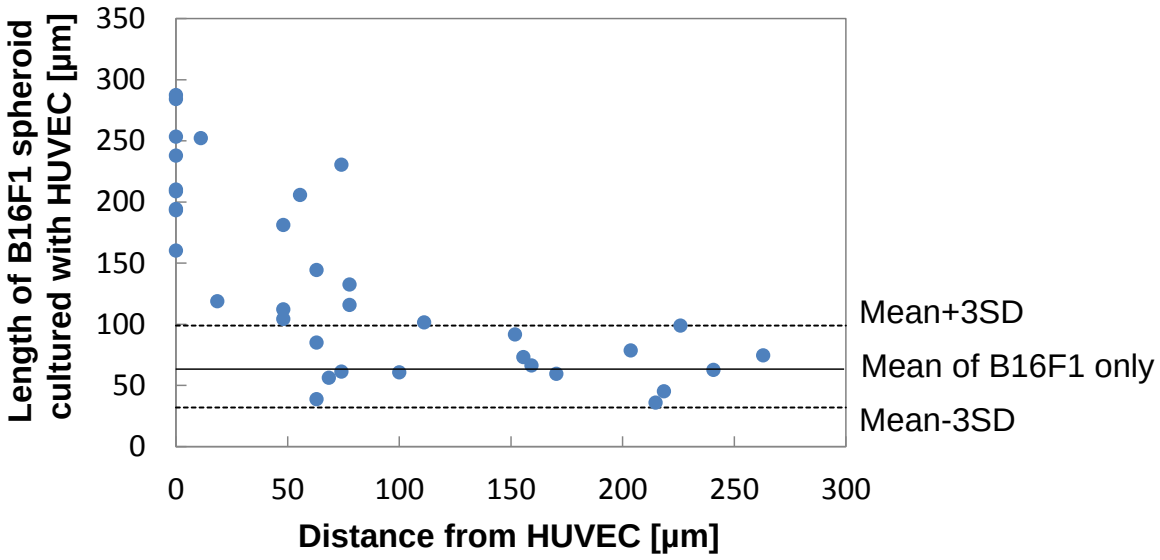

Fig. 4-6. The length of B16F1 spheroids co-cultured with HUVEC network. The length of B16F1 cell spheroids patterned in 10 cells/spheroid with 250 μm interval were image-analyzed by the green fluorescence after a 24 h culture with the HUVEC network. The plot represents the length of each B16F1 spheroid. The solid and dotted lines show the average length and the average length ± 3 × SD of B16F1 cell spheroids in 3D cell monoculture array.

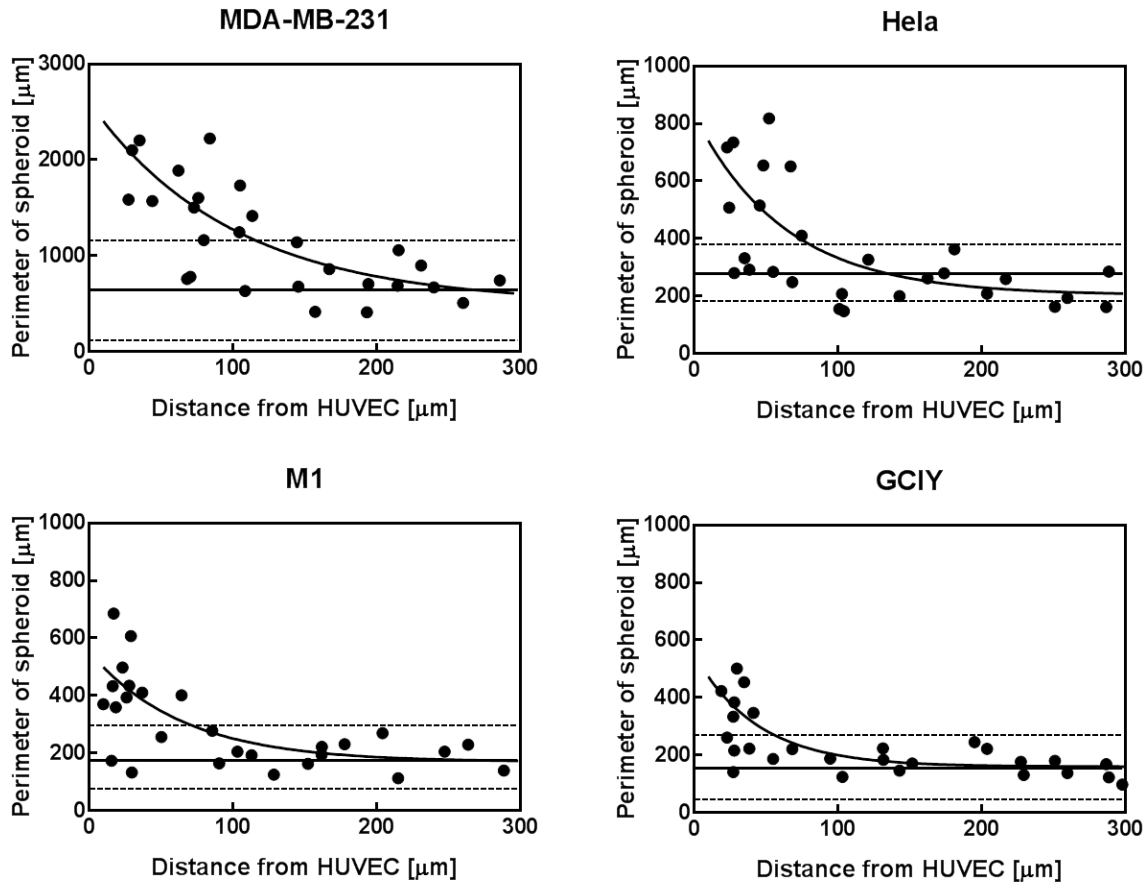

Fig. 4-6. The perimeter of spheroids of 4 cancer cell lines co-cultured with HUVEC network. The perimeter of spheroids of 4 cancer cell lines (MDA-MB-231, Hela, M-1, GCIY-EGFP) patterned in 10 cells/spheroid with 250 μm interval were image-analyzed by the green fluorescence after a 24 h culture with the HUVEC network. The plot represents the length of each cancer cell spheroid. The solid and dotted straight lines show the average length and the average length ± 3 × SD of cancer cell spheroids in 3D cell monoculture array. The solid curve line show the approximated curve using one phase decay.

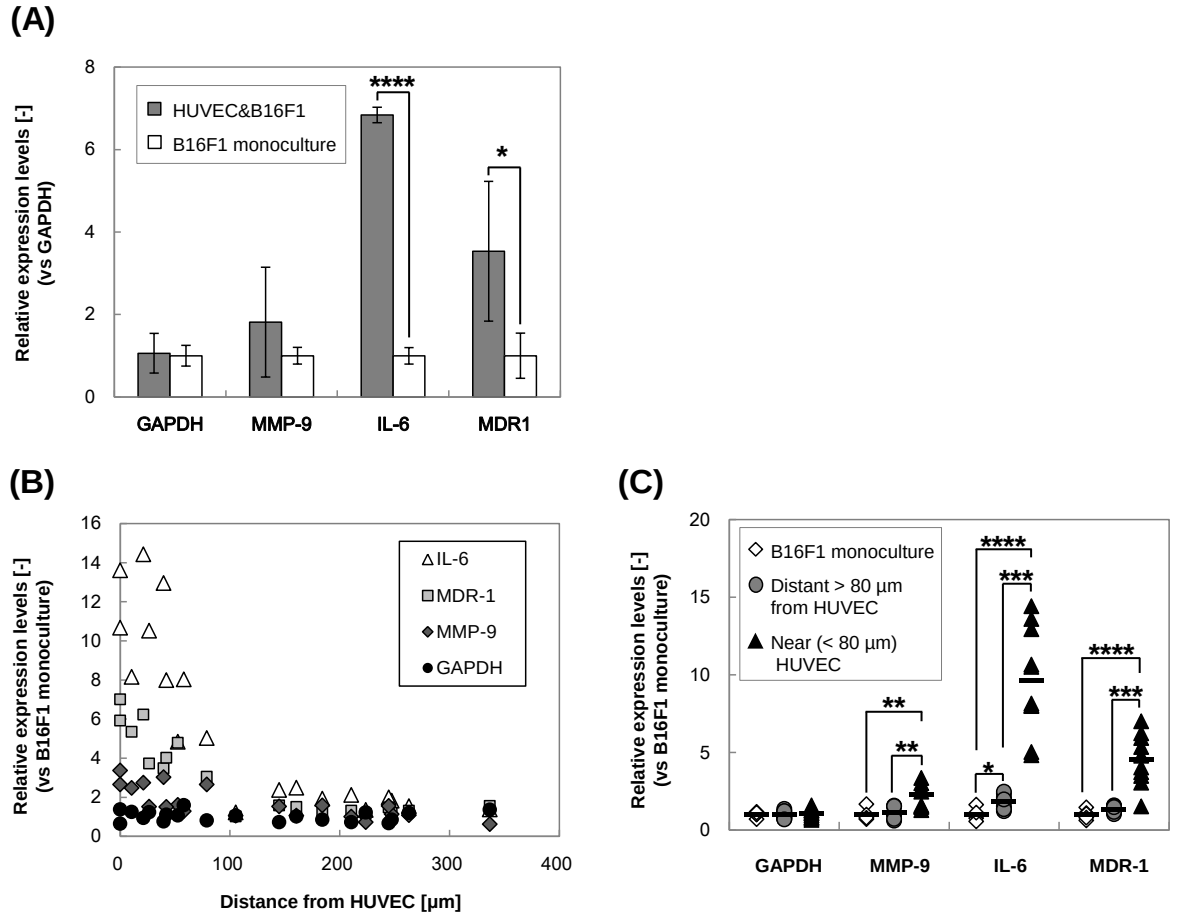

Fig. 4-8. Gene expression of MMP-9, IL-6, and MDR-1 in B16F1 spheroids co-cultured with HUVEC network after 1-day culture. (A) Relative expression levels of MMP-9, IL-6, and MDR-1 in B16F1 cells of a whole culture dish. The asterisks indicated that P value was regarded as a significant difference compared to B16F1 monoculture group (* $p < 0.05$, **** $p < 5\times10^{-5}$). Data points represent means ∓ SD of 3 independent experiments. (B) Relative expression levels in each spheroid were plotted with the distance from the nearest HUVEC network. Each spheroid was picked-up using a micromanipulator. (C) The expression levels in each B16F1spheroid placed near (≤ 80 μm) and distant (> 80 μm) to HUVEC was compared. Expression data was normalized to each gene expressions found in B16F1 monoculture using GAPDH as the reference gene. The asterisks indicated that P value was

regarded as a significant difference (* $p < 0.05$, ** $p < 0.005$, *** $p < 1\times10^{-4}$, **** $p < 5\times10^{-5}$, n = 5-10).

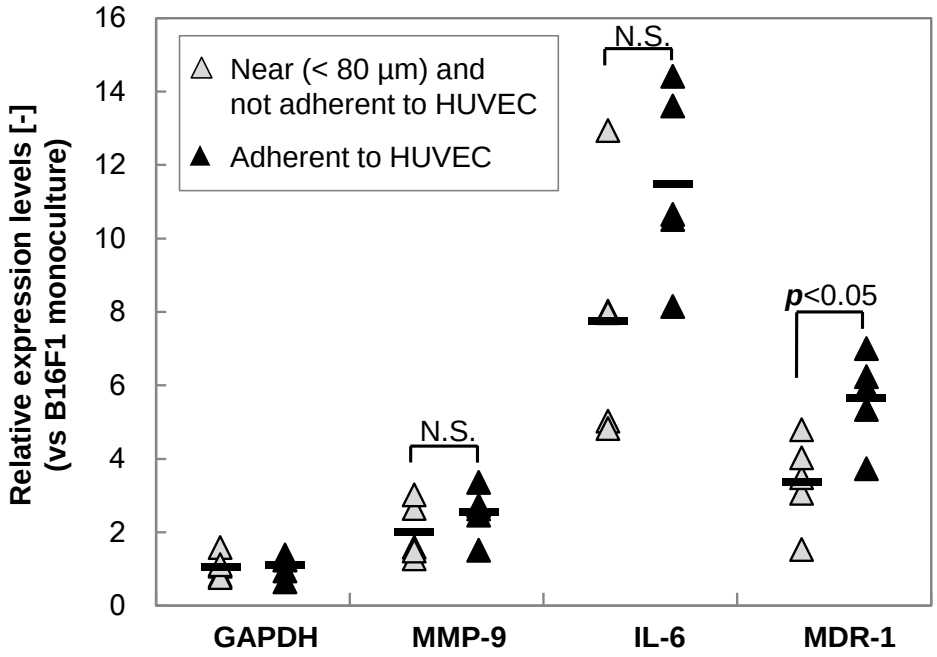

Fig. 4-9. Gene expressions in B16F1 spheroids that adhered or non-adhered to HUVEC. The expression levels in each B16F1 spheroid placed that adhered and non-adhered (< 80 μm) to HUVEC was compared. Expression data was normalized to each gene expressions found in B16F1 monoculture using GAPDH as the reference gene.

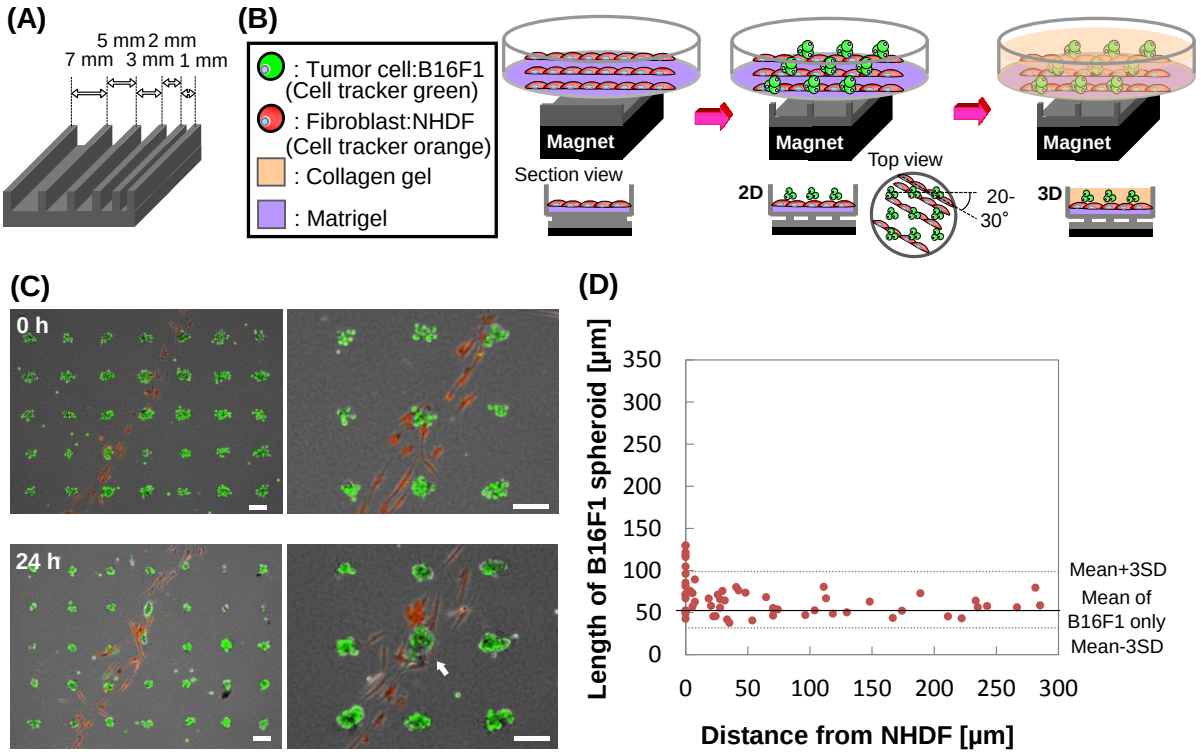

Fig. 4-10. The length of B16F1 spheroids co-cultured with the line patterning of fibroblast. (A) The pin-holder device for creating the line patterning of human fibroblast cell line NHDF with different spacing. The center-to-center distance of the pin-holder device was 1 mm to 7 mm, and the cells were arranged on pins according to magnetic force. (B) Schematic diagram for fabrication of the 3D cell culture array. The cell culture dish with a thin layer of Matrigel was placed on the pin-holder device with line patterning which is placed on the neodymium magnet. The NHDF, labeled with MCL and CellTracker orange, was inoculated on a thin layer of Matrigel for the line patterning at seeding density of 3×10^5 cells/dish, followed by 30 min incubation. The pin-holder device and the magnet were then removed from the culture dish. After 1-day culture, the cell culture dish was placed on the pin-holder device with array patterning which is placed on the neodymium magnet. The B16F1, labeled with MCL and CellTracker green, were patterned on the line patterning of NHDF for 30 min at seeding density of 10 cells/spheroid (1.8×10^5 cells/dish). The patterned

cells were then embedded with collagen gel, the pin-holder device and the magnet were then removed from the culture dish. (C) Magnetically labeled B16F1 cells were arrayed at seeding density of 10 cells/spheroid over NHDF lines. Time-lapse images were taken for three plates on 0 h and after 24 h. White arrows highlight B16F1 cells that have elongated with the NHDF. Scale bar: 100 μm. (D) The length of B16F1 cell spheroids patterned in 10 cells/spheroid with 250 μm interval were image-analyzed by the green fluorescence after a 24 h culture with the line patterning of NHDF. The plot represents the length of each B16F1 spheroid. The solid and dotted lines show the average length and the average length ± 3 × SD of B16F1 cell spheroids in 3D cell monoculture array.

TABLE 4-1. Sequences of primers for RT-PCR.

	Human (sequence 5'-3')		Mouse (sequence 5'-3')	
	Forward	Reverse	Forward	Reverse
GAPDH	CCTGACCTGCCGTCTAGAAA	TGCTGTAGCCAAATTCGTTG	AAGGGCTCATGACCACAGTC	CACTGGGGGTAGGAACAC
IL-6	TAGCCTCAATGACGACCTAAGCT	GGGCTGATTGGAAACCTTATTAAG	GAGGATACCACTCCCAACAGACC	AAGTGCATCATCGTTGTTCATACA
MMP-9	TGGGTGTACGACGGTGAAAA	CATGGGTCTCTAGCCTGATA	GCATACTTGTACCGCTATGG	TAACCGGAGGTGCAAACTGG
MDR1	CTGGTGTTTGGAGAAATGACAG	CCCAGTGAAAAATGTTGCCATTGAC	AACACAGCCAACCTTGGAAC	TGTTGCAATCTTTCCAGCAG

4.5. Summary

In vitro three dimensional (3D) cancer models were developed to observe the invasive capacity of melanoma cell spheroids co-cultured with the vascular-formed endothelial cell network. An array-like multicellular pattern of mouse melanoma cell line B16F1 was developed by magnetic cell labeling using a pin-holder device for allocation of magnetic force. When the B16F1 patterned together with a vascular network of human umbilical vein epithelial cells (HUVEC), spreading and progression were observed along the HUVEC network. The B16F1 cells over 80 μm distance from HUVEC remain in a compact spheroid shape, while B16F1 in the proximity of HUVEC aggressively changed their morphology and migrated. The mRNA expression levels of IL-6, MDR-1 and MMP-9 in B16F1 increased along with the distance from the HUVEC network, and these expressions were increased by 5, 3 and 2-fold in the B16F1 close to HUVEC (within 80 μm distance) as compared to that far from HUVEC (over 80 μm distance). Our results clearly show that malignancy of tumor cells is enhanced in proximity to vascular endothelial cells and leads to intravasation.

4.6. References

1. Friedl P, Alexander S. Cancer invasion and the microenvironment: Plasticity and reciprocity. Cell 147: 992-1009, 2011.
2. Quigley JP, Armstrong PB. Tumor cell intravasation alucidated: The chick embryo opens the window. Cell 94: 281-284, 1998.
3. Wang YH, Dong YY, Wang WM, *et al*. Vascular endothelial cells facilitated HCC invasion and metastasis through the Akt and NF-κB pathways induced by paracrine cytokines. J Exp Clin Cancer Res 32: 51, 2013.
4. Imaizumi T, Itaya H, Fujita K, *et al*. Expression of tumor necrosis factor-a in cultured human endothelial cells stimulated with lipopolysaccharide or interleukin-1 alpha. Arterioscler Thromb Vasc Biol 20: 410-415, 2000.
5. Aref AR, Huang RY, Yu W, *et al*. Screening therapeutic EMT blocking agents in a three-dimensional microenvironment. Integr Biol 5(2): 381-389, 2013.
6. Kang S, Zhou G, Yang P, *et al*. Molecular mechanism of pancreatic tumor metastasis inhibition by Gd@C82(OH)22 and its implication for de novo design of nanomedicine. Proceedings of the national academy of sciences 109: 15431-15436, 2012.
7. Khoufache K, Bazin S, Girard K, *et al*. Macrophage migration inhibitory factor antagonist blocks the development of endometriosis *in vivo*. PLoS One 7: e37264, 2012.
8. Li L, Dragulev B, Zigrino P, *et al*. The invasive potential of human melanoma cell lines correlates with their ability to alter fibroblast gene expression *in vitro* and the stromal microenvironment *in vivo*. Int J Cancer 125: 1796-1804, 2009.
9. Lin CW, Hou WC, Shen SC, *et al*. Quercetin inhibition of tumor invasion via suppressing PKC delta/ERK/AP-1-dependant matrix metalloproteinase-9 activation in breast carcinoma cells. Carcinogenesis 29: 1807-1815, 2008.

10. Gertz K, Kronenberg G, Kalin RE, *et al*. Essential role of interleukin-6 in post-stroke angiogenesis. Brain 135: 1964-1980, 2012.
11. Al-Mehdi AB, Tozawa K, Fisher AB, *et al*. Intravascular origin of metastasis from the proliferation of endothelium-attached tumor cells: a new model for metastasis. Nat Med 6: 100-102, 2000.
12. Bersini S, Jeon JS, Dubini G, *et al*. A microfluidic 3D *in vitro* model for specificity of breast cancer metastasis to bone. Biomaterials 35: 2454-2461, 2014.
13. Birgersdotter A, Sandberg R, Ernberg I. Gene expression perturbation *in vitro*—a growing case for three-dimensional (3D) culture systems. Seminars in Cancer Biology 15: 405-412, 2005.
14. Petersen OW, Ŕønnov-Jessen L, Howlett AR, *et al*. Interaction with basement membrane serves to rapidly distinguish growth and differentiation pattern of normal and malignant human breast epithelial cells. Proc Natl Acad Sci USA 89: 9064-9068, 1992.
15. Kunz-Schughart LA, Freyer JP, Hofstaedter F, *et al*. The use of 3-D cultures for high-throughput screening: the multicellular spheroid model. J Biomol Screen 9: 273-285, 2004.
16. Becker JL, Prewett TL, Spaulding GF, *et al*. Three dimensional growth and differentiation of ovarian tumor cell line in high aspect rotating-wall vessel: morphologic and embryologic considerations. J Cell Biochem 51: 283-289, 1993.
17. Håkanso M, Textor M, Charnley M. Engineered 3D environments to elucidate the effect of environmental parameters on drug response in cancer. Integr Biol 3: 31-38, 2011.
18. Sodunke TR, Turner KK, Caldwell SA, *et al*. Micropatterns of Matrigel for three-dimensional epithelial cultures. Biomaterials 28: 4006-4016, 2007.
19. Fukuda J, Khademhosseini A, Yeo Y, *et al*. Micromolding of photocrosslinkable chitosan hydrogel for spheroid microarray and co-cultures. Biomaterials 27: 5259-5267, 2006.

20. Kim JB. Three-dimensional tissue culture models in cancer biology. Cancer Biol 15: 365-377, 2005.
21. Fennema E, Rivron N, Rouwkema J, *et al*. Spheroid culture as a tool for creating 3D complex tissues. Trends Biotechnol 31: 108-115, 2013.
22. Shin MK, Kim SK, Jung H. Integration of intra- and extravasation in one cell-based microfluidic chip for the study of cancer metastasis. Lab Chip 11: 3880-3887, 2011.
23. Kim BJ, Hannanta-anan P, Chau M, *et al*. Cooperative roles of SDF-1a and EGF gradients on tumor cell migration revealed by a robust 3D microfluidic model. Pros One 8: e68422, 2013.
24. Okochi M, Takano S, Isaji Y, *et al*. Three-dimensional cell culture array using magnetic force-based cell patterning for analysis of invasive capacity of BALB/3T3/v-src. Lab Chip 9: 3378-3384, 2009.
25. Ino K, Okochi M, Konishi N, *et al*. Cell culture arrays using magnetic force-based cell patterning for dynamic single cell analysis. Lab Chip 8: 134-142, 2008.
26. Ino K, Okochi M, Honda H. Application of magnetic force-based cell patterning for controlling cell-cell interactions in angiogenesis. Biotechnol Bioeng 102: 882-890, 2009.
27. Okochi M, Matsumura T, Honda H. Magnetic force-based cell patterning for evaluation of the effect of stromal fibroblasts on invasive capacity in 3D cultures. Biosensors and Bioelectronics 42: 300-307, 2013.
28. Okochi M, Matsumura T, Yamamoto S, *et al*. Cell behavior observation and gene expression analysis of melanoma associated with stromal fibroblasts in a three-dimensional magnetic cell culture array. Biotechnology Progress 29: 135-142, 2013.
29. Shinkai M, Yanase M, Honda H, *et al*. Intracellular hyperthermia for cancer using magnetite cationic liposomes: *in vitro* study. Jpn J Cancer Res 87: 1179-1183, 1996.

30. Weaver AM. Invadopodia: Specialized cell structures for cancer invasion. Clinical & Experimental Metastasis 23: 97-105, 2006.
31. Segura I, Serrano A, De Buitrago GG, *et al*. Inhibition of programmed cell death impairs *in vitro* vascular-like structure formation and reduces *in vivo* angiogenesis. FASEB J 16: 833-841, 2002.
32. Shih W, Yamada S. N-cadherin-mediated cell-cell adhesion promotes cell migration in a three-dimensional matrix. J Cell Sci 125: 3661-3670, 2012.
33. Chang Q, Bournazou E, Sansone P, *et al*. The IL-6/JAK/Stat3 feed-forward loop drives tumorigenesis and metastasis. Neoplasia 15: 848-862, 2013.
34. Yeo EJ, Chun YS, Park JW. New anticancer strategies targeting HIF-1. Biochem Parmacol 68: 1061-1069, 2004.
35. Hutmacher DW. Biomaterials offer cancer research the third dimension. Nat Mater 9: 90-93, 2010.
36. Chen G, Goeddel DV. TNF-R1 signaling: A beautiful pathway. Science 296: 1634-1635, 2002.
37. Oeckinghaus A, Hayden MS, Ghosh S. Crosstalk in NF-κB signaling pathways. Nat Immunol 12: 695-708, 2011.
38. Beyaert R, Cuenda A, Vanden Berghe W, *et al*. The p38/RK mitogen-activated protein kinase pathway regulates interleukin-6 synthesis response to tumor necrosis factor. EMBO J 15: 1914-1923, 1996.
39. Koshikawa N, Yasumitsu H, Umeda M, *et al*. Multiple Secretion of Matrix Serine Proteinases by Human Gastric Carcinoma Cell Lines. Cancer Res 52: 5046-5053, 1992.
40. Darmoul D, Marie JC, Devaud H, *et al*. Initiation of human colon cancer cell proliferation by trypsin acting at protease-activated receptor-2. Br J Cancer 85: 772-779, 2001.

41. Jin X, Hirosaki T, Lin CY, *et al*. Production of soluble matriptase by human cancer cell lines and cell surface activation of its zymogen by trypsin. J Cell Biochem 95: 632-647, 2005.
42. Bäuerle T, Komljenovic D, Berger MR, *et al*. Multi-modal imaging of angiogenesis in a nude rat model of breast cancer bone metastasis using magnetic resonance imaging, volumetric computed tomography and ultrasound. J Vis Exp 14: e4178, 2012.
43. Park YW, Kim SG, Choi JY, *et al*. Recapitulating orthotopic tumor model through establishment of a parotid gland tumor with lung metastasis using HeLa cell injection into nude mice. Oncol Rep 23: 701-708, 2010.
44. Nakanishi H, Mochizuki Y, Kodera Y, *et al*. Chemosensitivity of peritoneal micrometastases as evaluated using a green fluorescence protein (GFP)-tagged human gastric cancer cell line. Cancer Sci 94:112-118, 2003.
45. Gaggioli C, Hooper S, Hidalgo-Carcedo C, *et al*. Fibroblast-led collective invasion of carcinoma cells with differing roles for RhoGTPases in leading and following cells. Nat Cell Biol. 9:1392-1400, 2007.

Chapter 5

Efficient capturing of circulating tumor cells using a magnetic capture column and a size-selective filter

5.1. Introduction

Circulating tumor cells (CTCs) are frequently detected in patients with metastatic cancer and have been linked to poor prognosis [1]. Therefore, they can be used as a surrogate for primary tumor cells for the monitoring of tumor phenotypes and clinical stage [2, 3]. However, CTCs are rare, making their detection and isolation difficult; there are $1-10^2$ CTCs in 7.5 mL of blood, consisting of red blood cells (RBCs), white blood cells (WBCs), macrophages, and granulocytes, and so on [4]. Efficient enrichment is therefore a prerequisite for CTC detection and isolation, and the development of detection methods for CTCs has received a great deal of attention, the aim of which is earlier diagnosis of metastatic disease [5].

To date, many researchers have reported about CTC detection devices that utilize a captured antibody [6]. Indeed, the most common method for CTC capturing is

antibody-mediated capture, using an antibody to epithelial cell adhesion molecule (EpCAM). The CellSearch system (Veridex, Raritan, NJ), a semiautomated cell capture technology that was recently approved by the US Food and Drug Administration, enriches CTCs from whole blood by the use of antibody-coated ferrofluids that target epithelial cell markers such as EpCAM. Clinical studies using EpCAM-positive CTC detection demonstrated that the number of CTCs in peripheral blood could be used to predict the prognosis of patients with metastatic lung [4], breast [7], colorectal [8], and prostate cancer [9]. These CTCs were also found to be associated with clinical stage, disease recurrence, and disease monitoring before and after treatment [10, 11].

It is important to note that the concept of EpCAM-dependent assays is based upon the assumption that the presence of epithelial cells in peripheral blood indicates the presence of tumor cells. The expression of epithelial antigen is downregulated to increase invasiveness and metastatic potential by epithelial-to-mesenchymal transition (EMT) [12, 13]. Several studies have shown that the presence of EpCAM on tumor cells varies with tumor type [14, 15]. Therefore, the use of EpCAM as a positive selection marker is not always optimal, and may not achieve stable and reproducible recovery of CTCs [5].

Other researchers have developed CTC isolation methods based on differences in size and deformability between CTCs and coexisting hematologic cells [16-18]. These devices are based on the fact that almost all cultured epithelial tumor cells are larger than RBCs and WBCs, except for those of minor subgroups, such as small cell lung cancers. Advantages of these size-based capture devices are rapid and efficient enrichment of almost all CTCs, including cells undergoing EMT; low cost [17]; and easy isolation of single living CTCs, which is somewhat difficult to achieve by an antibody-coated microfluidic device and cell sorter type CTC enrichment device [19].

Recently, we have reported the use of a size-selective 3D palladium filter device for

capturing CTCs, and successfully achieved the detection, enrichment, isolation, and genetic analysis of CTCs in both preclinical and clinical settings [20]. However, we also found that at high flow rates (greater than 2 mL/min), the recovery rate of the spiked cancer cells from diluted human blood gradually decreased when using only this filter. Similarly, most other size-based methods of CTC capture from diluted or undiluted blood used low flow rates to increase the recovery rate [5, 17, 18], making CTC detection a time-consuming process. Thus, in the clinical setting, rapid and efficient capturing techniques are needed to obtain a sufficient number of CTCs for their practical detection from large volume blood samples, such as diluted blood.

Magnetic cell capturing techniques using magnetic particles have also been the focus of much attention as a powerful and effective tool for CTC capture by binding cells to magnetic particles with a high capture rate [21]. Kang *et al*. successfully captured a high proportion of EpCAM-positive breast cancer cell line M6C cells (within 90% of the spiked M6C cells) using EpCAM antibody-conjugated magnetic nanoparticles and a microfluidic device at 0.02 mL/min of the loading flow rate [22]. However, as mentioned above, this technique was antibody-dependent and still required the time-consuming step of binding CTCs to the antibodies.

We have developed magnetite cationic liposomes (MCLs) that can be used for antibody-independent magnetic labeling of various kinds of human and mammalian cells [23-28]. Since the lipid component of the MCLs includes a cationic lipid and the surface of the MCLs is positively charged, MCLs have a high affinity to negatively charged cell surfaces. Magnetically labeled cells can be manipulated by magnetic force. We have previously shown that MCLs had little effect on cell viability, growth, differentiation, and gene expression [25, 29], indicating that magnetically labeling cells with MCLs would have little effect on their original phenotypic characteristics, such as genetic traits and/or protein expression patterns.

Considering these advantages of MCLs, we envisaged that MCLs could be used for magnetic labeling of CTCs. The combined use of magnetic capturing and size-based capturing would improve the recovery process of CTCs, without use of any antibodies.

In the present study, we constructed a magnetic capture column and investigated whether the combined use of the magnetic capture column and a size-selective filter [20] improved the CTC recovery process (**Fig. 5-1**). In this process, a relatively large blood volume is transferred into the magnetic capture column at a high flow rate, CTCs labeled with MCLs in the blood are captured within the magnetic column by magnetic force, and the captured CTCs are then gently sorted by the size filter at a low flow rate with a small volume of phosphate buffer saline (PBS).

5.2. Materials and methods

5.2.1. Cell culture

In this study, the GCIY-EGFP cell line was used as a model of metastatic cancer cells. GCIY is a poorly differentiated human gastric carcinoma cell line (RIKEN Cell Bank, Ibaraki, Japan); GCIY-EGFP cells express green fluorescent protein (GFP), as described previously [30]. The GCIY-EGFP cell line was cultured on 10 cm dishes in Dulbecco's Modified Eagle's Medium, high glucose (Invitrogen, Gaithersburg, MD, USA) supplemented with 10% fetal bovine serum (FBS) (Invitrogen), 0.1 μg/mL streptomycin sulfate, and 100 U/mL potassium penicillin G (Invitrogen).

The RPMI1788 cell line, a human lymphoblastoid cell line (RIKEN Cell Bank) was cultured on 10 cm dishes in Roswell Park Memorial Institute (RPMI) 1640 medium (Invitrogen), supplemented with 10% FBS (Invitrogen), 0.1 μg/mL streptomycin sulfate, and 100 U/mL potassium penicillin G (Invitrogen). Cells were cultured in a humidified 5% CO_2 incubator at 37 °C. To evaluate the capture rate of RPMI1788 cells as a model white blood

cells (WBC) using the size-selective filter with or without the magnetic capture column, RPMI1788 cells were stained with CellTracker Orange (CMTMR; Molecular Probes, Eugene, OR, USA). The average sizes of these cells were 12.8 ± 3.5 μm (GCIY) and 8.5 ± 3.5 μm (RPMI1788), respectively, based on image analysis.

5.2.2. Preparation of MCLs

MCLs were prepared as described in 2.2.2. Magnetite nanoparticles (Fe_3O_4, mean diameter 10 nm, saturated magnetization 63.9 Am^2/kg, residual magnetization 2.6 Am^2/kg, and coercivity 2.0 kA/m; Toda Kogyo Co., Hiroshima, Japan) and a lipid mixture of N-(a-trimethylammonioacetyl)-didodecyl-D-glutamate chloride, dilauroyl phosphatidylcholine, and dioleoylphosphatidylethanolamine at a respective molar ratio of 1:2:2 were used.

5.2.3. Evaluation of MCL uptake to spiked cancer cells in human blood

To evaluate the uptake of MCLs to spiked cancer cells in whole human blood, we examined the magnetite concentration of cancer cells spiked into blood samples taken from 3 healthy volunteers under written informed consent. Blood was diluted 5-fold with PBS, 10 mL samples of which were spiked with either 1×10^5 GCIY-EGFP cells (as a cancer cell model) or 1×10^5 RPMI1788 cells (as a WBC model). We then incubated the blood samples with MCLs equivalents to a total amount of 3 μg or 10 μg magnetite for 10 minutes. The whole cells in the blood samples were collected by centrifugation, and the concentration of magnetite was evaluated using the potassium thiocyanate method, as described previously [27]. To evaluate the distributions of MCLs to GCIY-EGFP or RPMI1788 cells in the co-existing conditions of the RBCs, we calculated the difference of MCL uptake into each cell type, and divided by the spiked cell numbers as follows:

MCL uptake [pg/cell] = {(Amount of MCLs with spiked GCIY-EGFP or RPMI1788 cells [pg]) - (Amount of MCLs without spiked GCIY-EGFP or RPMI1788 cells [pg])} / (Number of spiked cells [cell])

In addition, we evaluated the MCL uptake to RBCs from the magnetite concentration of the non-spiked blood sample, divided by the total number of RBCs. The concentration of RBCs was determined using a hemocytometer as described previously [31].

Furthermore, we obtained human peripheral blood mononuclear cell (PBMC) as a native WBC model, and compared the MCL uptake of PBMCs to that of RPMI1788. PBMCs were isolated from blood samples of one healthy volunteer under written informed consent using density gradient centrifugation on Histopaque (Sigma-Aldrich; St. Louis, MO, USA). Either 1 × 10^5 PBMCs or 1 × 10^5 RPMI1788 cells was spiked into 1 mL of PBS and incubated with MCLs equivalents to 10 μg of magnetite for 10 min. These cells were collected by centrifugation and the concentration of magnetite was compared using the potassium thiocyanate method [27].

5.2.4. Fabrication of the magnetic capture column

The magnetic capture column was fabricated to capture the magnetically labeled cells and to improve the recovery rate of cancer cells on the size-selective filter at a high flow rate (**Fig. 5-2A**). Each column has a base of acrylate, measuring approximately 42 (length) × 20 (width) × 5 (height) mm. A bed type vertical milling machine (Model YZ-8WR; YAMAZAKI GIKEN Co. Ltd., Kochi, Japan) with a steel end mill (Model EDS, φ = 2 mm; OSG, Kochi, Japan) was used to construct the crater for magnets (dimensions of 22 (length) × 20 (width) × 3.5 (depth) mm) and the inner cavity (dimensions of 22 (length) × 10 (width) × 0.2 (depth) mm). The size of the inner cavity of the column was optimized to trap the magnetically labeled cells on the cavity surface at a high flow rate of blood (greater than 20

mL/min) in the preliminary experiment. We constructed two copies of each part, which were adhered using acrylic adhesive (Acryl Dine A, Shinko Plastics Co. Ltd., Tokyo, Japan). The total size of the column is approximately 42 (length) × 20 (width) × 10 (height) mm, and the total size of the inner cavity is approximately 22 (length) × 10 (width) × 0.4 (depth) mm.

5.2.5. Fabrication of the size-selective capture filter

The size-selective capture filter was produced by microfabrication technology, consisting of lithography and electroforming processes, as described previously (**Fig.5-2B**) [20]. A photo-sensitive coating (photo-resist) was applied to a metal substrate and resist patterns (photomasks) formed on this conductive substrate using a UV or X-ray lithography process and rises off the solved photo-resist. Metal molecules, Pd or Pd-Nickel (4:1) alloy, electrodeposited on the matrix (substrate) in areas not masked with photo-resist (i.e., the patterned surface), were thicker than the resist, resulting in an overhang on the resist formed on the substrate via electroforming. Once the material was deposited at the desired thickness, the electroformed part could be stripped off from the metal substrate and the product was complete. The finished filter had holes with a round shape resembling a bell mouth.

5.2.6. Evaluation of recovery rate

For magnetic cell labeling, we dispersed MCLs in a 10 mL sample containing cancer cells to a total amount of 10 μg of magnetite, incubated for 10 minutes. To capture the cancer cells using the size-selective filter combined with the magnetic capture column, 10 mL of magnetically-labeled sample containing cancer cells was loaded into the magnetic capture column with neodymium cuboid magnets (437 mT, Magfine, Miyagi, Japan) at 0.5-20 mL/min using a syringe pump (KDS100, KD Scientific, MA, USA). Next, the size-selective filter setting in Swinnex Filter Holder (13mm, Merck Millipore, Darmstadt, Germany) was

added to the column after detaching the magnet from the column, and magnetically captured cells were sorted using a syringe pump (kd Scientific) with 3 mL of PBS at 0.5 mL/min. The cells captured on the size-selective filter were directly observed and counted using a fluorescence microscope (Model IX81; Olympus Co., Tokyo, Japan) to evaluate the recovery rate of the cancer cells.

To evaluate the recovery rate of the size-selective filter with the magnetic capture column, we prepared the loading samples which was included average 100 GCIY-EGFP cells in 10 mL of PBS or FBS, and incubated the loading samples with MCLs containing 10 μg of magnetite. Then, we captured the cells using the size-selective filter with the magnetic capture column, and counted the captured cells on the filter by a fluorescence microscope.

To evaluate the recovery rate from coexisting cells, 100 GCIY-EGFP cells and 2×10^5 orange fluorescent-labeled RPMI1788 cells in 10 mL of FBS were labeled by MCLs and captured magnetically in the capture column at a flow rate of 10 mL/min. After counting of these captured cells in the magnetic capture column by the green and orange fluorescent observation, these captured cells were sorted with 3 mL of PBS at 0.5 mL/min, and counted the remained cells in the magnetic capture column and the captured cells in the filter. Furthermore, to evaluate the capture sensitivity of the rare spiked cancer cells from the coexisting cells using the combined method, 5, 10, 50, or 100 GCIY cells were spiked into 10 mL of FBS with 2×10^5 RPMI1788 cells, and the capture rates were compared among the different spike conditions using the same method described above.

To evaluate the recovery rate from human blood, we spiked 100 GCIY-EGFP cells in 10 mL of 5-fold diluted human blood with PBS. After magnetically labeling, the cells were captured using the size-selective filter with the magnetic capture column, and counted the captured cells on the filter. The blood was obtained from 3 healthy volunteers under written informed consent.

Every recovery rates were calculated as follows:

Recovery rate [%] = (Number of captured cells [cells]) / (Number of spiked cell numbers [cells]) × 100.

5.2.7. CTC capture from whole blood in a mouse model of metastasis

Seven- to eight-week-old male athymic nude mice (KSN strain) were obtained from Shizuoka Laboratory Animal Center (Hamamatsu, Japan) and maintained under specific pathogen-free conditions. All animal experiments were performed according to protocols approved by the Ethics Review Committee for Animal Experimentation of the Aichi Cancer Center and met the standards defined by the United Kingdom Coordinating Committee on Cancer Research guidelines.

We developed mice CTC models as reported previously [20]. Briefly, exponentially growing GCIY-EGFP cells were harvested with trypsin-EDTA, washed with Hank's balanced salt solution (HBSS), and resuspended in HBSS. A tumor cell suspension (5×10^6 cells/0.2 mL) was subcutaneously injected into the back and lower abdominal flanks of the nude mice. After 1-3 months, blood was harvested from the posterior caval vein of the mice, and lung tissue was obtained after dissection.

Approximately 1 mL of whole blood was 5-fold diluted with PBS and then incubated for 10 minutes with MCLs at a total amount of 10 μg magnetite for magnetic labeling. CTCs were captured using the size-selective filter with or without the magnetic capture column, at a flow rate of 10 mL/min for magnetic capture and at 0.5 mL/min, for cell sorting. The captured GFP-positive cells on the size-selective filter were observed and counted using a fluorescent microscope (Model IX81). The captured GFP-positive cells were collected using a micromanipulator. The phase-contrast and fluorescent images of the captured cells were obtained using a microscope (Model IX81) and were merged using image analysis software

(MetaMorph, Universal Imaging Co., Downingtown, PA, USA). The CTC capturing experiment was performed three times (Experimental No. 1, 2, and 3 in **Table 5-1**).

5.2.8. Statistical Analysis

The statistical significance of differences in data between groups was determined by applying Student's t-test or Welch's two-tailed t-test.

5.3. Results

5.3.1. Uptake of MCLs to spiked cancer cells in human blood

From capture of CTCs by magnetic force in the magnetic column, the cells first need to be labeled magnetically by MCLs in the blood. Thus, we firstly quantified the amount of magnetite uptake to the spiked cancer cells in human blood. Blood from volunteers under written informed consent was diluted 5-fold with PBS, 10 mL samples of which were spiked with GCIY-EGFP cells. The spiked blood samples were then incubated with MCLs.

Fig. 5-3A shows the time course of magnetite uptake to the spiked GCIY-EGFP cells. Time-dependent increases of magnetite uptake were observed, and the uptake to the spiked GCIY-EGFP cells was around 2-3-fold higher in the 10-μg magnetite group than in the 3-μg magnetite group. After only 3-minute incubation, more than 15 pg magnetite/cell was observed in the spiked GCIY-EGFP cells of the 10-μg magnetite group. The MCL uptake profile of spiked RPMI 1788 cells were similar to that of GCIY-EGFP cells (**Fig. 5-3B**), whereas uptake by RBCs was low (less than 5×10^{-5} pg/cell) (**Fig. 5-3C**). We confirmed that magnetically labeled cells with more than 10 pg magnetite/cell could be captured magnetically using a flow chamber (data not shown). These results indicate that CTCs and WBCs in the blood would be captured to the column and separated from RBCs by magnetic capturing processes (**Fig. 5-1A-i**). We also confirmed that the addition of a 10 μg magnetite

equivalent of MCLs and incubation for 10 minutes were sufficient conditions for GCIY-EGFP cells in PBS or FBS-containing solution to be labeled magnetically in sufficient numbers to be captured by the column. Thus, we adopted these conditions for magnetic labeling of cells in our subsequent experiments. In addition, the size of the magnetic labeled GCIY-EGFP cells did not change significantly compared to that of the non-labeled GCIY-EGFP cells by microscopic observation (data not shown), indicating that this labeling method did not be affect to the size-based capturing.

5.3.2. Recovery rate of spiked cancer cells by the size-selective filter device combined with the magnetic column

We next evaluated the recovery rate of spiked cancer cells using the combination of the magnetic capture column and the size-selective filter (**Fig. 5-1A**). GCIY-EGFP cells were spiked into 10 mL of the sample solutions and labeled magnetically with MCLs. To investigate the effects of sample viscosity, we used both FBS as a sample of undiluted serum with a high-viscosity and 5-fold diluted FBS with PBS (20% FBS/PBS) as a sample of 5-fold diluted serum, because FBS has 1.8-fold higher viscosity than PBS.

Firstly, we determined recovery rates using the filter only (**Fig. 5-4A**). The size-selective filter had high recovery rates at a sample flow rate of 0.5 mL/min (89.0% from PBS, 85.7% from 20% FBS/PBS, and 80.7% from 100% FBS). However, the recovery rates gradually decreased with increasing the flow rate, as described previously [20]. Recovery rates at 20 mL/min were 64.3% in PBS, 48.7% in 20% FBS/PBS, and 43.3% in 100% FBS. Based on these results, we decided to use 0.5 mL/min flow rate and PBS containing to magnetically capture cells for the size-selective capturing process (**Fig. 5-1A-ii**).

Next, we determined the optimal sample flow rate into the magnetic capture column for the magnetic capturing process (**Fig. 5-1A-i**) to achieve high recovery rates of the spiked

cancer cells. GCIY-EGFP cells were spiked into 100% FBS or 20% FBS/PBS and the sample flow rates at 2, 5, 10, and 20 mL/min were examined. As shown in **Figs. 5-3B and 5-3C**, the recovery rates were as high for the combination of the magnetic capture column and the filter as those using the filter only at 0.5 mL/min of the loading flow rate for almost all conditions, with the excepting of 20 mL/min for 100% FBS. Recovery rates were 85.7%, 83.3%, and 84.7% at 2, 5, and 10 mL/min respectively for 100% FBS; and 89.3%, 86.3%, 82%, and 82% at 2, 5, 10, and 20 mL/min respectively for 20% FBS/PBS. Since a 10 mL/min flow rate gave a high recovery rate for both solutions, we used 10 mL/min for sample flow into the column in the subsequent experiments.

We found that high recovery rates of the spiked cells could be achieved rapidly by the combination of the column and the filter compared to the use of the filter only (**Figs. 5-3B and 5-3C**). For example, to process 10 mL of the 100% FBS samples (a model of undiluted blood), 7 minutes was required for the combination of column and filter (**Fig. 5-4B**): 10 mL/min for 10 mL of sample in the magnetic capturing process, and 0.5 mL/min for 3 mL PBS in the size-selective capturing process (**Fig. 5-1A**). By contrast, 20 minutes was required to process the same sample using the filter alone: 0.5 mL/min for 10 mL of sample (**Fig. 5-4B**). Furthermore, to process 50 mL of 20% FBS/PBS samples (a model of 10 mL of blood, diluted 5-fold), 11 minutes was required for the combination of column and filter, whereas 100 minutes was required for the filter alone (**Fig. 5-4C**). Therefore, the combination of the magnetic capture column and the size-selective filter would be suitable for efficient and rapid capturing of CTCs.

5.3.3. Separation of spiked cancer cells and coexisting lymphocytes by use of the column and filter

Since incubation with MCLs labels both cancer cells and WBCs in the blood (**Fig. 5-3**),

cancer cells and WBCs cannot be separated using the magnetic capture column alone. Thus, we investigated whether these cell types could be separated by the combined use of magnetic capture column and the size-selective capture filter. We spiked GCIY-EGFP cells and RPMI1788 cells in 10 mL of FBS, labeled them with MCLs, flowed the sample solution into the column at 10 mL/min, and flow-captured cells through the filter using 3 mL of PBS at a flow rate of 0.5 mL/min.

After magnetic capture, we observed large numbers of GCIY-EGFP cells and RPMI1788 cells with orange fluorescent labeling on the inner surface of the magnetic column (upper image in **Fig. 5-5A**). The capture rates were 97.7% ± 1.50% for GCIY-EGFP cells and 97.5% ± 1.50% for RPMI1788 cells (graph in **Fig. 5-5A**).

After flowing of the captured cells to the filter, few cells were observed on the inner surface of the column (lower image in **Fig. 5-5A**). The capture rates were significantly decreased to 3.3% for GCIY-EGFP cells and 4.0% for RPMI1788 cells (graph in **Fig. 5-5A**). These results indicated that the magnetic capture column could capture and release almost all magnetically labeled cells in the sample. In the size-selective filter, we observed numerous GCIY-EGFP cells, whereas few RPMI1788 cells were observed on the filter (images in Fig. 5B). The recovery rate of GCIY-EGFP cells was 87.0% ± 3.0% and that of RPMI1788 cells was 3.7% ± 0.50%; the recovery rate of GCIY-EGFP cells was therefore 17.4-fold higher than that of RPMI1788 cells (graph in **Fig. 5-5B**). We also evaluated the percentage of GCIY-EGFP cells in the total captured cells; 100 GCIY-EGFP cells and 1×10^4 RPMI1788 cells labeled with orange fluorescence were spiked into 10 mL of FBS, and the recovery of the cells was performed by using both of the column and filter. As a result, 70.4% of the total captured cells were GCIY-EGFP cells (data not shown).

Furthermore, we investigated the capturing sensitivity of the rare spiked cancer cells from the coexisting cells. Either 5, 10, 50, or 100 GCIY cells were spiked into a 10-mL

solution with 2×10^5 RPMI1788 cells, similar to *in vivo* blood samples [4]. The combined use of a magnetic capture column and the size-selective capture filter had a sensitivity that captured an average of 3.7 ± 0.58 cells/5 spiked GCIY-EGFP cells (**Fig. 5-5C**). From these results, we conclude that the combined use of the magnetic capture column and the size-selective filter could selectively recover cancer cells at a high recovery rate from a sample containing WBCs.

5.3.4. Recovery rates of spiked cancer cells from human blood

We examined whether cancer cells could be recovered at a high rate from blood (which contains WBCs and RBCs) by using the combination of the column and filter. We spiked GCIY-EGFP cells into 10 mL of 5-fold diluted human blood and the recovery of the cells was performed. Since 7 minutes are required to recover the cells for the combined experiment, the total time required to filter the sample was set at 7 min for the filter only experiment; 10 mL of the sample was flowed to the filter at 1.43 mL/min. As shown in **Fig. 5-6**, the recovery rate for the combination of the magnetic column and the filter (80.7% ± 4.0%) was significantly higher than that of the filter only (64.7% ± 2.5%), using the same time for capturing.

5.3.5. Capturing of CTCs from the blood of metastatic tumor model mice

Finally, to test the diagnostic potential of our capturing device, we developed mice CTC models and demonstrated CTC capture from blood withdrawn from the model mice. GFP-positive GCIY-EGFP cells were subcutaneously injected into mice and macroscopic lung metastasis was observed within 2-3 months of the injection (**Fig. 5-8**). We were able to capture GFP-positive cells from the blood of these mice using the combination of the column and the filter, and the number of captured GFP-positive cells was significantly higher than the number captured using only the size-selective filter (**Fig. 5-7** and **Table 5-1**, $p < 0.01$, 2-fold).

In the mouse model used in this study, the lung metastasis remained small, at less than 1 mm in diameter (**Fig. 5-8**). This indicates that our device could capture CTCs during a relatively early stage of metastatic development in mice.

5.4. Discussion

In the present study, we constructed a magnetic capture column for combined use with a size-selective filter. By using the developed column and the filter together, we succeeded in rapid and highly efficient recovery of the spiked cancer cells, as the model of CTCs, from blood samples spiked with cancer cells (**Figs. 5-3 and 5-5**) and the CTCs from the blood of metastatic model mice (**Fig. 5-6 and Table 5-1**). In contrast, previously reported size-based devices for CTC capture could capture CTCs at high recovery rates only at low loading flow rates of 0.2-2 mL/min [5, 17, 32], making cell capture a time-consuming process. Thus, our combined process has the potential to allow a more rapid and efficient diagnosis based on CTC capture and detection.

We observed higher MCL uptake to spiked cancer cells and WBCs than to RBCs in whole human blood (**Fig. 5-3**). This low MCL labeling level of RBCs might be due to differences in cell properties between RBCs, and cancer cells or WBCs. For example, cancer cells and lymphocytes have greater negative surface potential than RBCs, and have more phagocytic capacity than RBCs [33-35]. Based on differences in the MCL labeling level, we could separate the cancer cells and WBCs from RBCs in our magnetic capture column (**Figs. 5-6 and 5-7**). Since the MCL uptake of native human PBMC spiked into PBS was not significantly different than that of RPMI1788 (27.8 ± 7.7 pg/cell and 30.3 ± 4.7 pg/cell, respectively), we inferred that the MCL uptake of RPMI1788 in this study could represent the MCL uptake of native human PBMCs. Since hemoglobin, which is the major protein of RBCs, can affect the results of PCR [36], the separation of the large number of RBCs from the other

cells existing in the blood would be important for accurate gene expression analysis of these cells. Considering these results, our method may be useful for gene expression analysis of captured CTCs.

Since we have confirmed that the magnetically labeled cells at greater than 10 pg/cell could be captured by the column, we added a 10-μg magnetite equivalent of MCLs to the sample and incubated it for 10 min for sufficient cell labeling (**Figs. 5-4-5-7, Table 5-1**). In the present study, we did not consider the MCL labeling time required to recover the cells by the combined method of the column and the filter, and did not optimize the labeling conditions. However, our data suggested that the MCL labeling time would be shortened. As shown in **Fig. 5-3**, a 3-min incubation for 10 μg of MCL could achieve greater than 10 pg/cell. Our previous study also indicated that less than 1 min of incubation time provides sufficient magnetic labeling for the magnetic separation, and an increase of the amount of MCL resulted in an increase in the magnetite uptake [37]. Furthermore, we expect that if the MCLs are stored in the blood-collecting vessel, the magnetic cell labeling by MCL might be achieved during a blood draw, which is essential for CTC detection from blood samples. Therefore, future optimization of the MCL labeling conditions would make our combined method more practical.

CTCs captured from blood could be used as a surrogate for primary tumor cells for the purposes of monitoring tumor phenotypes and clinical stage [2, 3]. We have successfully performed gene expression analysis of captured GCIY-EGFP cells, as a model of CTCs, by collecting the cells using a micromanipulator in the spike experiment *in vitro*, as previously reported [25]. This analysis found that Muc-2 gene expression levels of captured GCIY-EGFP cells were similar to that of cultured GCIY-EGFP before MCL labeling (Unpublished data). Muc-2 is an epithelial tumor marker in various cancers [38-40], and its expression has been shown to be related to tumor malignancy [41]. Furthermore, magnetic cell labeling by MCLs

has not been shown to affect the proliferation and differentiation of any of the various types of normal and cancer cells labeled by this method, including human stem cells [29, 25]. Considering these results, it was concluded that MCLs and the magnetic capturing process did not disturb the analysis of the captured CTCs.

Moreover, we found that a portion of the CTCs captured from metastatic model mice showed a proliferative ability *in vitro* (unpublished data). The magnetic capture column did not affected the viability of GCIY-EGFP cells (after capturing: 97.6 ± 0.9%, before capturing: 98.8 ± 1.1%), and the size-selective filter could be used for the gentle isolation of live CTCs with less cellular stress than that of conventional antibody-based techniques [20]. Therefore, our combined method would be more suitable to capture viable CTCs than the conventional techniques. We plan to analyze the sensitivity of CTCs to anti-cancer drugs. This might open up the possibility to utilize CTC capture in diagnosis and anti-cancer treatment planning for patients with metastatic cancer in the future.

In conclusion, the combined use of the magnetic capture column and the size-based capturing filter is a promising process for the rapid and efficient isolation and genetic analysis of CTCs from peripheral blood.

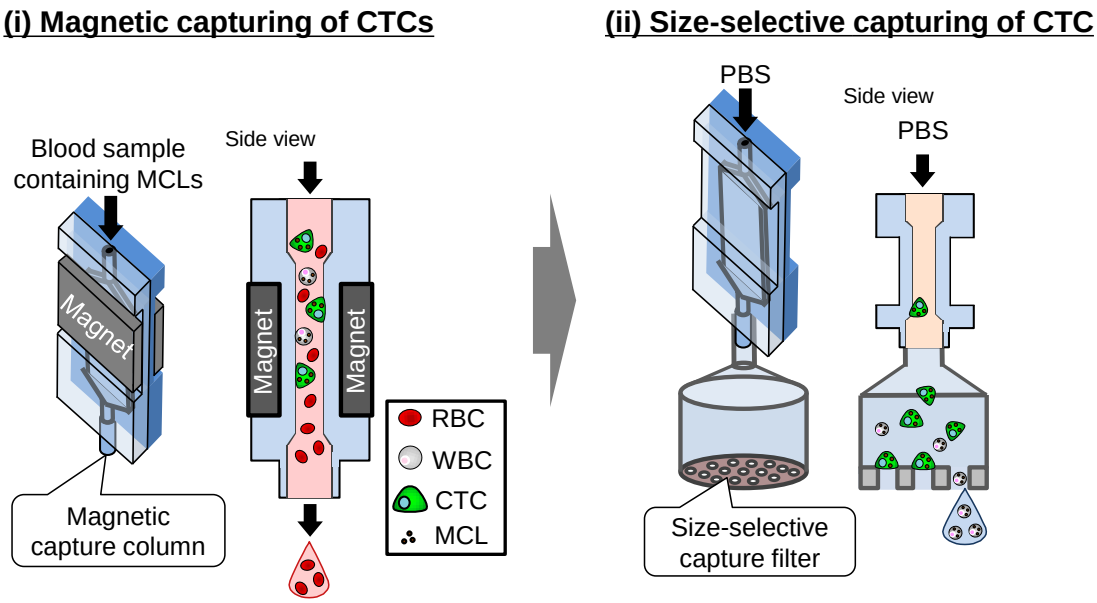

Fig. 5-1. Schematic diagram of magnetic column combined with size-selective filter for circulating tumor cell (CTC) capture Schematic diagram of fabrication of the CTC capture device using the magnetic column and size-selective filter. Blood containing CTCs was magnetically labeled using magnetite cationic liposomes (MCLs) and magnetically labeled cells were captured by the magnetic column. These captured cells were then sorted and CTCs were size-selectively captured on the filter.

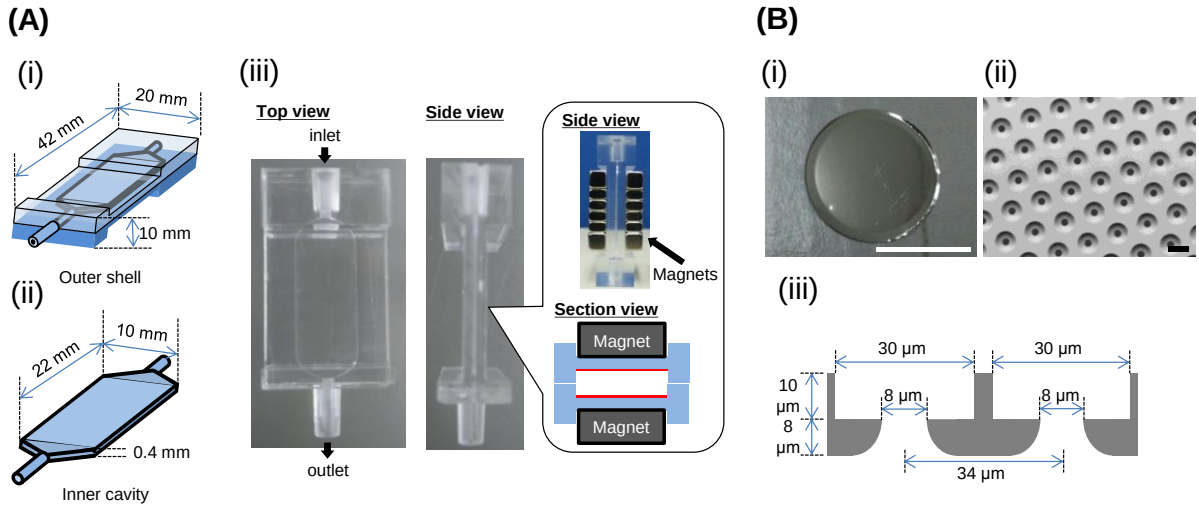

Fig. 5-2. Characterization of the magnetic column and size-selective filter (A) Photographs and illustrations of the magnetic CTC capture column. The column included an inner cavity and a cassette of magnets to capture magnetically labeled cells. (B) (i) Macroscopic view and (ii) SEM image (lower panel) of the size-selective filter. *Scale bars*: 1 cm (upper panel), and 30 μm (lower panel). (iii) Section view of the size-selective filter, with 8-μm pores in the lower layer and 30-μm CTC capture pockets in the upper layer.

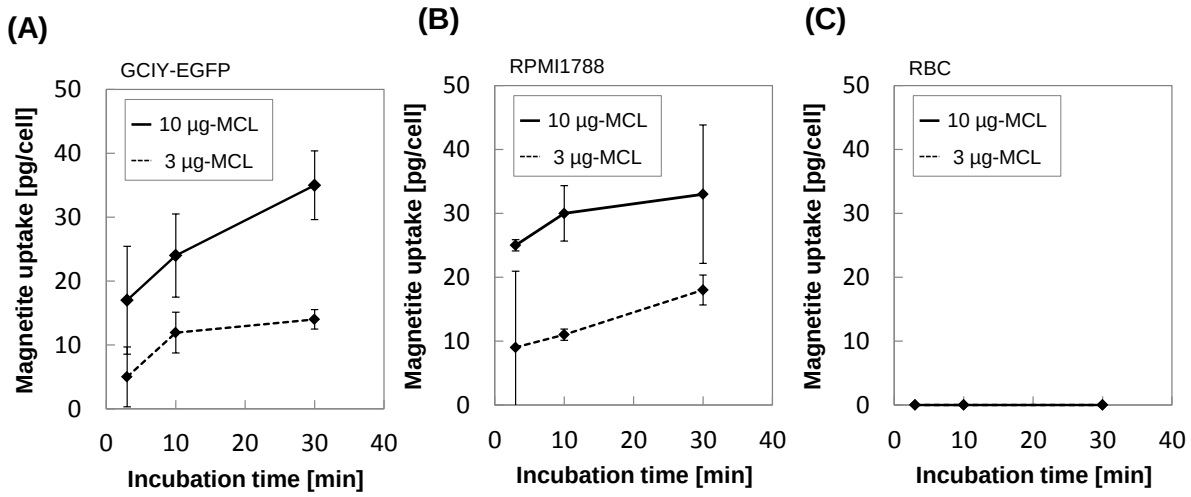

Fig. 5-3. Uptake of magnetite cationic liposomes (MCLs) to spiked cancer cells in human blood MCLs were distributed to the spiked cancer cells (GCIY-EGFP), lymphocytes (RPMI), and red blood cells (RBCs) in human blood, and the uptake of magnetite to each cell type were evaluated by the colorimetric method using thiocyanate. Graphs show the uptake to (A) GCIY-EGFP, (B) RPMI1788, and (C) RBCs. Data are presented as mean ± SD, n = 3.

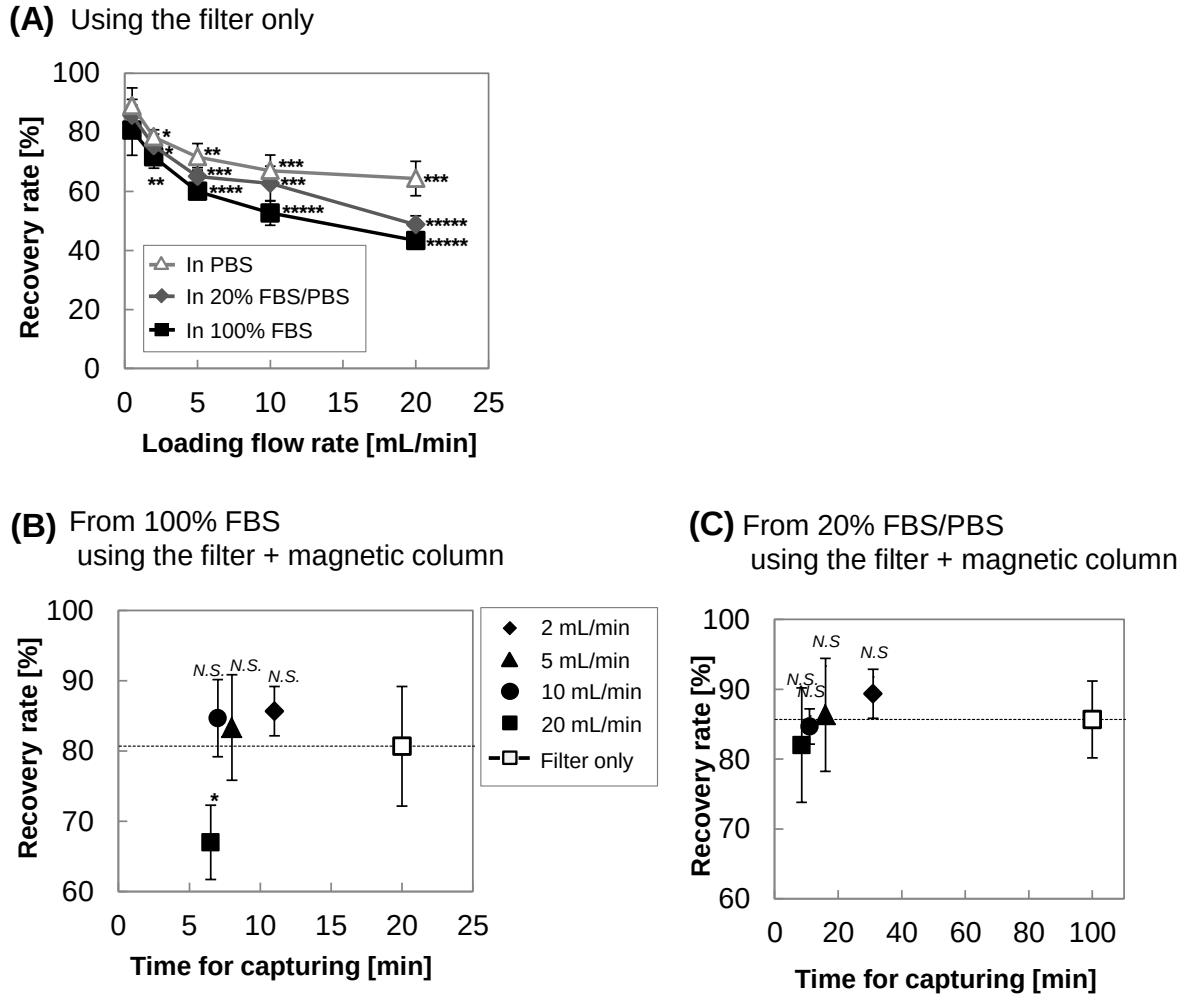

Fig. 5-4. Recovery rate of spiked cancer cells by the size-selective filter device combined with the magnetic column (A) Recovery rate of spiked cancer cells by the size-selective filter only. Samples containing 100 GCIY-EGFP cells in PBS, 20% FBS/PBS, and 100% FBS were prepared, and the spiked GCIY-EGFP cells were captured using the size-selective filter device only. Data are presented as mean ± SD, n = 3. Asterisks indicate that the P value was regarded as a significant difference compared to the control group, which was captured from PBS at 0.5 mL/min using the size-selective filter only (* p <0.05, ** p <0.01, *** p <5×10^{-3}, **** p <1×10^{-3}, ***** p <5×10^{-4}), and N.S. indicates no significant difference. (B) Capture time and recovery rate of spiked GCIY-EGFP cells from 100% FBS (as a model of

non-diluted serum) using the size-selective filter, with or without the magnetic column at various loading flow rates. Black icons show the recovery rate at various loading flow rates using the size-selective filter device with the magnetic column; the white icon shows the recovery rate using the filter only at 0.5 mL/min. Data are presented as mean ± SD, n = 3. Asterisks indicate that the P value was regarded as a significant difference compared to the control group, which was captured from PBS at 0.5 mL/min using the size-selective filter only (* p <0.05), and N.S. indicates no significant difference. (C) Capture time and recovery rate of spiked GCIY-EGFP cells from 20% FBS/PBS (as a model of 5-fold diluted serum) using the size-selective filter only, with or without the magnetic column at various loading flow rates. Black icons show the recovery rate at various loading flow rates using the size-selective filter device with the magnetic column; the white icon shows the recovery rate using the filter only at 0.5 mL/min. Data are presented as mean ± SD, n = 3. N.S. indicates no significant difference compared to the control group, which was captured from PBS at 0.5 mL/min using the size-selective filter only (* p <0.05).

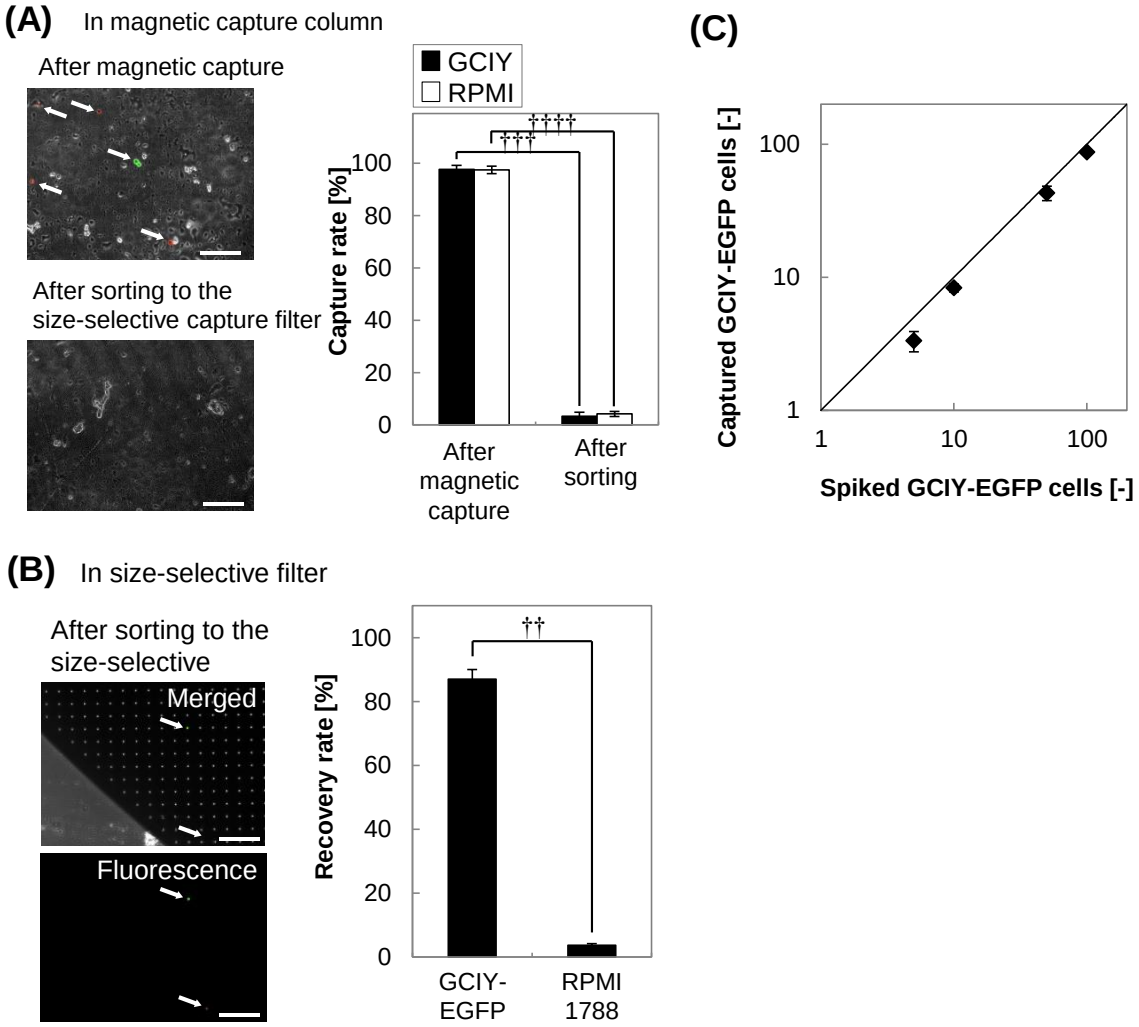

Fig. 5-5. Recovery rate of spiked cancer cells from coexisting lymphocytes (A) Capture of GCIY-EGFP cells from coexisting lymphocytes (RPMI1788) using the magnetic capture column. The left panels show microscopic images of the magnetic capture column after magnetic capture (upper) or after sorting the magnetically captured cells to the size-selective filter (lower). The right graph shows the capture rate of magnetically labeled cells in the magnetic capture column after the magnetic capturing, or after the sorting the magnetically captured cells to the size-selective filter. (B) Capture of GCIY-EGFP cells from coexisting lymphocytes (RPMI1788) in 100% FBS using the size-selective filter and the magnetic column. The left panels show microscopic images of the captured cells in the size-selective

filter after sorting the magnetically captured cells to the size-selective filter. The right graph shows the recovery rate of GCIY-EGFP and RPMI1788 cells in the size-selective filter with the magnetic capture column. Data are presented as mean ± SD, n = 3. Asterisks indicated that the P value was regarded as a significant difference compared to the control group († $p < 5\times10^{-5}$, †† $p < 1\times10^{-7}$, ††† $p < 5\times10^{-8}$). *Scale bar*: 100 μm. (C) Capture efficiencies of the spiked GCIY-EGFP cells into 100% FBS (5 to 100 GCIY-EGFP cells in a 10-mL solution with 2×10^5 of RPMI1788 cells) obtained using the size-selective filter with the magnetic capture column.

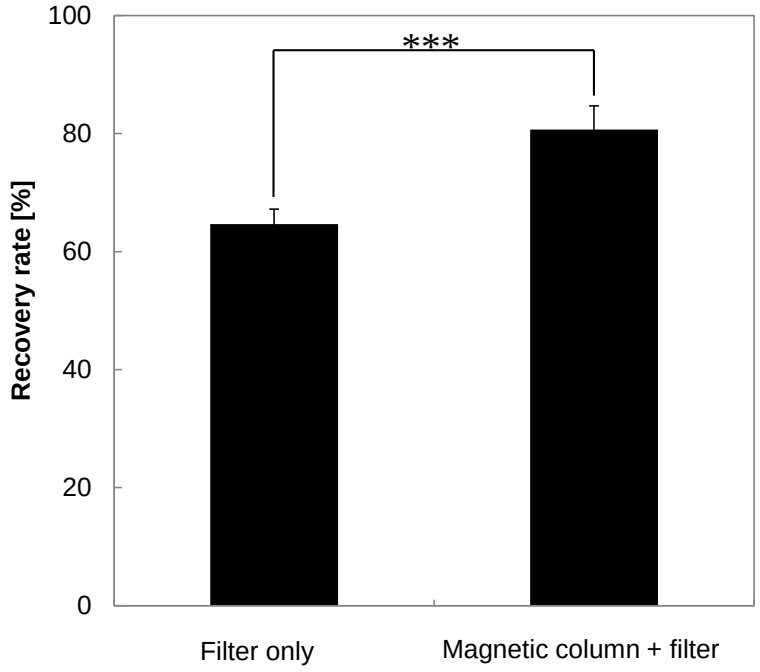

Fig. 5-6. Recovery rate of spiked cancer cells from human blood Recovery rates of spiked GCIY-EGFP cells from 10 mL of 5-fold diluted human blood using the size-selective filter and the magnetic column. "Magnetic column + filter" means the recovery rate using the filter with the magnetic capture column at a total capture time of 7 min (1 min for magnetic capturing at 10 mL/min, and 6 min for sorting to the filter at 0.5 mL/min). "Filter only" means the recovery rate using the filter at the same total capture time (7 min for filtering at 10 mL/7 min). Data are presented as mean ± SD, n = 3. Asterisks indicate that the P value was regarded as a significant difference compared to the filter only (*** $p < 5 \times 10^{-3}$).

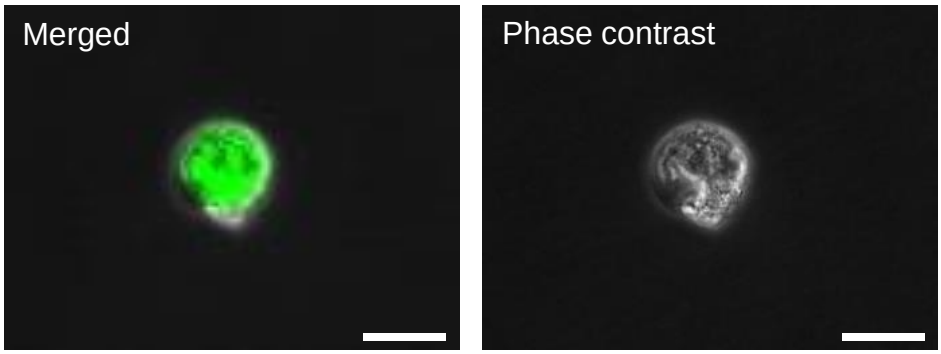

Fig. 5-7. Microscopic images of representative captured EGFP-positive cells from whole blood of tumor bearing mice. EGFP-positive cells were magnetically labeled by magnetite cationic liposomes, and were captured from the whole blood of tumor bearing mice using the size-selective filter device combined with the magnetic column. Scale bar: 10 μm.

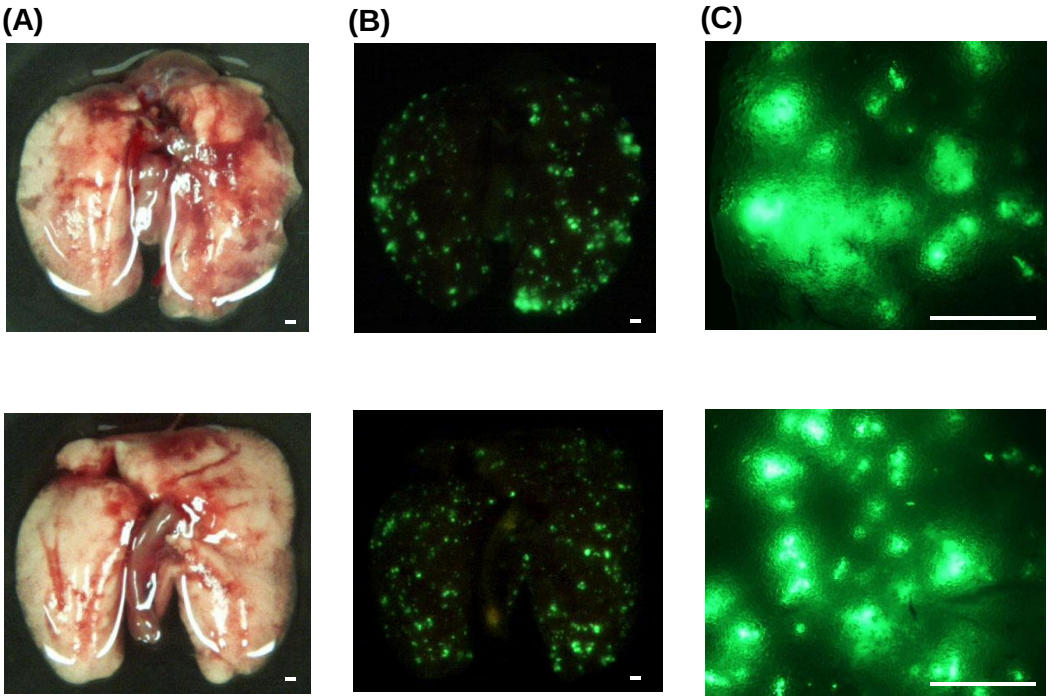

Fig. 5-8. Lung metastasis in the spontaneous metastasis model of nude mice for circulating tumor cell (CTC) capture The lungs of nude mice were obtained 2-3 months after subcutaneous injection of GFP-tagged EGFP cells, and the two representative photographs (A) and fluorescent images (B, C) were taken. Scale bar: 200 μm.

Table 5-1. Numbers of EGFP-positive cells capture from the whole blood of tumor bearing mice

Experiment No.	Magnetic capture + filter	Filter only
1	22	8
2	18	12
3	16	5
Average	18.7	8.3

The number of captured EGFP-positive cells using the combination of the magnetic capture and the filter was significantly higher than the number captured using only the size-selective filter (p <0.01).

5.5. Summary

Detecting and analyzing circulating tumor cells (CTCs) in the blood of cancer patients is a promising approach for the early diagnosis of metastasis. Previously, we developed a size-selective filter for capturing CTCs, but its use was time-consuming, particularly for capturing CTCs from large volumes of blood. In the present study, we describe the use of a magnetic capture column for rapid and efficient isolation of CTCs, which were magnetically labeled with magnetite cationic liposomes. In the capturing process, large volumes of blood containing magnetically labeled cancer cells were introduced into the column at a high flow rate to capture the cells, which were then flowed into the filter at a low flow rate. Our results show that the combined use of the column and filter decreased the required time for the spiked cancer cell capture, and the recovery rate of the spiked cancer cells from blood was significantly higher using the combination process (80.7%) than that using the filter alone (64.7%). Moreover, almost twice the number of CTCs could be captured from the blood of metastatic model mice by using the combination process. These results suggest that the developed process would be useful for the rapid and efficient isolation of CTCs.

5.6. References

1. Pantel K, Brakenhoff RH. Dissecting the metastatic cascade. Nat Rev Cancer 4:448-456, 2004.
2. Nadal R, Fernandez A, Sanchez-Rovira P, *et al*. Biomarkers characterization of circulating tumour cells in breast cancer patients. Breast Cancer Res 14:12, 2012.
3. Sandri MT, Zorzino L, Cassatella MC, *et al*. Changes in circulating tumor cell detection in patients with localized breast cancer before and after surgery. Ann Surg Oncol 17:1539-1545, 2010.
4. Hosokawa M, Hayata T, Fukuda Y, *et al*. Size-selective microcavity array for rapid and efficient detection of circulating tumor cells. Anal Chem 82:6629-6635, 2010.
5. Ozkumur E, Shah AM, Ciciliano JC, *et al*. Inertial focusing for tumor antigen-dependent and -independent sorting of rare circulating tumor cells. Sci Transl Med 5:11, 2013.
6. Cristofanilli M, Budd GT, Ellis MJ, *et al*. Circulating tumor cells, disease progression, and survival in metastatic breast cancer. N Engl J Med 351:781-791, 2004.
7. Krebs MG, Hou JM, Sloane R, *et al*. Analysis of circulating tumor cells in patients with non-small cell lung cancer using epithelial marker-dependent and -independent approaches. J Thorac Oncol 7:306-315, 2012.
8. Lu CY, Tsai HL, Uen YH, *et al*. Circulating tumor cells as a surrogate marker for determining clinical outcome to mFOLFOX chemotherapy in patients with stage III colon cancer. Br J Cancer 108:791-797, 2013.
9. Thalgott M, Rack B, Maurer T, *et al*. Detection of circulating tumor cells in different stages of prostate cancer. J Cancer Res Clin Oncol 139:755-763, 2013.
10. Liu MC, Shields PG, Warren RD, *et al*. Circulating tumor cells: A useful predictor of treatment efficacy in metastatic breast cancer. J Clin Oncol 27:5153-5159, 2009.
11. Lucci A, Hall CS, Lodhi AK, *et al*. Circulating tumour cells in non-metastatic breast

cancer: a prospective study. Lancet Oncol 13:688-695, 2012.

12. Yu M, Bardia A, Wittner B, *et al*. Circulating breast tumor cells exhibit dynamic changes in epithelial and mesenchymal composition. Science 339:580-584, 2013.
13. Vona G, Estepa L, Beroud C, *et al*. Impact of cytomorphological detection of circulating tumor cells in patients with liver cancer. Hepatology 39:792-797, 2004.
14. Went PT, Lugli A, Meier S, *et al*. Frequent EpCam protein expression in human carcinomas. Hum Pathol 35:122-128, 2004.
15. Sieuwerts AM, Kraan J, Bolt J, *et al*. Anti-epithelial cell adhesion molecule antibodies and the detection of circulating normal-like breast tumor cells. J Natl Cancer Inst 101:61-66, 2009.
16. Vona G, Sabile A, Louha M, *et al*. Isolation by size of epithelial tumor cells - A new method for the immunomorphological and molecular characterization of circulating tumor cells. Am J Pathol 156:57-63, 2000.
17. Hosokawa M, Kenmotsu H, Koh Y, *et al*. Size-based isolation of circulating tumor cells in lung cancer patients using a microcavity array system. PLoS One 8: e67466, 2013.
18. Desitter I, Guerrouahen BS, Benali-Furet N, *et al*. A new device for rapid isolation by size and characterization of rare circulating tumor cells. Anticancer Res 31:427-441, 2011.
19. Takao M, Takeda K. Enumeration, characterization, and collection of intact circulating tumor cells by cross contamination-free flow cytometry. Cytometry A 79A:107-117, 2011.
20. Yusa A, Toneri M, Masuda T, *et al*. Development of a new rapid isolation device for circulating tumor cells (CTCs) using 3D Palladium filter and its application for genetic analysis. PLoS One 9: e88821, 2014.
21. Wu LY, Liu TC, Hopkins MR, *et al*. Chemoaffinity capture of pre-targeted prostate cancer cells with magnetic beads. Prostate 72:1532-1541, 2012.
22. Kang JH, Krause S, Tobin H, *et al*. A combined micromagnetic-microfluidic device for

rapid capture and culture of rare circulating tumor cells. Lab Chip 12:2175-2181, 2012.

23. Shimizu K, Ito A, Lee JK, *et al*. Construction of multi-layered cardiomyocyte sheets using magnetite nanoparticles and magnetic force. Biotechnol Bioeng 96:803-809, 2007.
24. Shimizu K, Ito A, Arinobe M, *et al*. Effective cell-seeding technique using magnetite nanoparticles and magnetic force onto decellularized blood vessels for vascular tissue engineering. J Biosci Bioeng 103:472-478, 2007.
25. Yamamoto S, Hotta MM, Okochi M, *et al*. Effect of vascular formed endothelial cell network on the invasive capacity of melanoma using the *in vitr*o 3D co-culture patterning model. PLoS One 9: e103502, 2014.
26. Ino K, Okochi M, Honda H. Application of magnetic force-based cell patterning for controlling cell-cell interactions in angiogenesis. Biotechnol Bioeng 102:882-890, 2009.
27. Okochi M, Matsumura T, Yamamoto S, *et al*. Cell behavior observation and gene expression analysis of melanoma associated with stromal fibroblasts in a three-dimensional magnetic cell culture array. Biotechnol Prog 29:135-142, 2013.
28. Okochi M, Takano S, Isaji Y, *et al*. Three-dimensional cell culture array using magnetic force-based cell patterning for analysis of invasive capacity of BALB/3T3/v-src. Lab Chip 9:3378-3384, 2009.
29. Shimizu K, Ito A, Yoshida T, *et al*. Bone tissue engineering with human mesenchymal stem cell sheets constructed using magnetite nanoparticles and magnetic force. J Biomed Mater Res B Appl Biomater 82B:471-480, 2007.
30. Nakanishi H, Mochizuki Y, Kodera Y, *et al*. Chemosensitivity of peritoneal micrometastases as evaluated using a green fluorescence protein (GFP)-tagged human gastric cancer cell line. Cancer Sci 94:112-118, 2003.
31. Okochi M, Sakai Y, Isaji Y, *et al*. Personalized assessment of oxidative cellular damages associated with diabetes using erythrocytes adhesion assay. J Biosci Bioeng 112:635-637,

2011.

32. Chung J, Shao HL, Reiner T, *et al*. (2012) Microfluidic cell sorter (μFCS) for on-chip capture and analysis of single cells. Adv Healthc Mater 1:432-436, 2012.
33. Wall J, Ayoub F, Oshea P. Interactions of macromolecules with the mammalian-cell surface. J Cell Sci 108:2673-2682, 1995.
34. Zhang Y, Yang M, Portney NG, *et al*. Zeta potential: a surface electrical characteristic to probe the interaction of nanoparticles with normal and cancer human breast epithelial cells. Biomed Microdevices 10:321-328, 2008.
35. Pasquale L, Winiski A, Oliva C, *et al*. An experimental test of new theoretical-models for the electrokinetic properties of biological-membranes - The effect of UO2++ and tetracaine on the electrophoretic mobility of bilayer-membranes and human-erythrocytes. J Gen Physiol 88:697-718, 1986.
36. Al-Soud WA, Radstrom P. Purification and characterization of PCR-inhibitory components in blood cells. J Clin Microbiol 39:485-493, 2001.
37. Ito H, Kato R, Ino K, *et al*. Magnetic manipulation device for the optimization of cell processing conditions. J Biosci Bioeng 109:182-188, 2010.
38. Bengtsson AM, Jonsson G, Magnusson C, *et al*. The cysteinyl leukotriene 2 receptor contributes to all-trans retinoic acid-induced differentiation of colon cancer cells. BMC Cancer 13:13, 2013.
39. Kai H, Yoshitake K, Hisatsune A, *et al*. Dexamethasone suppresses mucus production and MUC-2 and MUC-5AC gene expression by NCI-H292 cells. Am J Physiol Lung Cell Mol Physiol 271:L484-L488, 1996.
40. Khazan N, Ghavamzadeh A, Boyajyan A, *et al*. MUC2 mRNA detection in peripheral blood and bone marrow of breast cancer patients reveals micrometastasis. Nat Sci 5:38-43, 2013.

41. Imai Y, Yamagishi H, Fukuda K, *et al*. Differential mucin phenotypes and their significance in a variation of colorectal carcinoma. World J Gastroenterol 19:3957-3968, 2013.

Chapter 6

Ex vivo culture of circulating tumor cells from blood of metastasis model mice using magnetic force-based cell co-culture on a fibroblast feeder layer

6.1. Introduction

Circulating tumor cells (CTCs) are present in the blood of many patients with metastatic tumor [1] and have been linked to poor prognosis [2]. They can be used as a surrogate for primary tumor cells for the monitoring of tumor phenotypes and clinical stage [3, 4]. However, since CTCs are present at very low concentrations, their detection and isolation are difficult; there are $1-10^2$ CTCs in 7.5 mL of blood [5].

To date, CTC-isolation methods have been proposed, including cell marker-dependent and -independent methods. The former methods involve a magnetic separation using anti-epithelial cell adhesion molecule (EpCAM) antibody conjugated magnetic beads, such as CellSearch system (Veridex, Raritan, NJ) [5-10]. However, the presence of EpCAM on tumor

cells varies with tumor type [11, 12], and the expression of epithelial antigen is downregulated to increase invasiveness and metastatic potential by epithelial-to-mesenchymal transition (EMT) [13, 14]. Thus, cell marker-dependent methods are not always applicable, and may not achieve stable and reproducible recovery of CTCs [15]. The latter methods involve filters to separate CTCs. These methods are based on the differences in size and deformability of CTCs and coexisting hematologic cells [15-17], and have advantage on rapid and simple isolation of almost all CTCs, including cells undergoing EMT [18].

The isolated CTCs were subsequently analyzed by several methods, such as the genome mutation analysis and malignant-related marker expression analysis [13, 14, 19]. In addition to these analyses, the phenotype-based analysis of *ex vivo* cultured CTCs, such as growth, invasiveness or drug sensitivity analysis, becomes of increasing importance recently [1, 20]. Ameri *et al*. reported that *ex vivo* cultured CTCs from metastasis model mice showed an altered hypoxia response and an enhanced aggressive phenotype *in vitro* and *in vivo* [20]. Yu *et al*. performed the drug sensitivity testing of *ex vivo* cultured CTCs with multiple mutations from patients, and have shown that the cultured CTCs provides an opportunity to study patterns of drug susceptibility, linked to the genetic context that is unique to an individual tumor [1]. As shown in these pioneering studies, the phenotype-based analysis of *ex vivo* cultured CTCs is a potent and promising strategy for exploring new therapeutic targets and understanding CTCs' biological properties. However, proliferation of the isolated CTCs are still technically challenging because CTCs are very rare and most of CTCs are dead in the circulation.

Previously, we have developed the cell surface marker independent method for rapid and efficient isolation of CTCs, in which a magnetic capture column and a size-selective 3D palladium filter device were used in combination [18, 21]. In this combination process, CTCs

in blood of metastatic model mice were magnetically labeled independently of cell surface markers by using magnetite cationic liposomes (MCLs), which are cationic liposomes containing 10 nm-magnetite nanoparticles. Both CTCs and white blood cells were labeled with MCLs via electrostatic interaction between positively charged MCLs and the negatively charged cellular membrane [21]. Then, a relatively large volume of the blood was passed through into the magnetic capture column at a high flow rate, and the magnetically captured CTCs were then gently sorted by the size filter at a low flow rate. Comparing to the use of the filter only, almost twice the number of CTCs were isolated from the blood using the combination process [21]. We also confirmed that the combination process did not affect the viability of the isolated cells when the tumor cells were artificially spiked into blood *in vitro* as a CTCs model. However, when we seeded the isolated CTCs from the blood of metastasis model mice onto the cell culture dish and incubated at normal cell culture condition (37 °C, 5% CO_2), we could not observe the growth of the cells. Thus, some technical developments are needed to support the growth of the isolated CTCs.

Here, we report a novel method for *ex vivo* culture of CTCs using a fibroblast feeder layer and a magnetic force-based cell co-culture method [22-27]. A fibroblast feeder layer has been used for preparing the culture condition of stem cells, including embryonic stem cells and induced pluripotent stem cells [28, 29]. It has also been reported that the fibroblasts promote the survival capacity, adhesion, and proliferation in many cancer cell lines via remodeling the ECM [30-33]. Therefore, we hypothesized that co-culture of isolated CTCs with fibroblasts would support the proliferation of CTCs. Furthermore, to facilitate the attachment of isolated CTCs on the fibroblast feeder layer, we used a magnetic force-based co-culture method [22-27]. In this method, the magnetically labeled cells were forced to be positioned on the cultured feeder layer by magnetic field of a magnet [22-27].

In the present study, we isolated CTCs from blood of metastatic model mice by our

combination method [21] and cultured the isolated magnetically labeled CTCs on the fibroblasts layer by using a magnetic force-based co-culture method. We obtained three clones of CTC-derived cells, and phenotype analyses were demonstrated.

6.2. Materials and methods

6.2.1. Cell culture

The COLM5-EGFP cell line was used as a model of metastatic cancer cells. COLM5 is a poorly differentiated human colorectal carcinoma cell line (RIKEN Cell Bank, Ibaraki, Japan); COLM5-EGFP cells express green fluorescent protein (GFP), as described previously [26]. The COLM5-EGFP cell line, the CTC-derived cells (COLM5-EGFP-CTC1, COLM5-EGFP-CTC2, and COLM5-EGFP-CTC3), and the mouse fibroblast NIH-3T3 were cultured on 10 cm dishes in Dulbecco's Modified Eagle's Medium, high glucose (Invitrogen, Gaithersburg, MD, USA) supplemented with 10% fetal bovine serum (FBS) (Invitrogen), 0.1 μg/mL streptomycin sulfate, and 100 U/mL potassium penicillin G (Invitrogen). Cells were cultured in a humidified 5% CO_2 incubator at 37 °C.

6.2.2. Animals and Ethics Statement

Seven- to eight-week-old male athymic nude mice (KSN strain) were obtained from Shizuoka Laboratory Animal Center (Hamamatsu, Japan) and maintained under specific pathogen-free conditions. All animal experiments were performed according to protocols approved by the Ethics Review Committee for Animal Experimentation of the Aichi Cancer Center and met the standards defined by the United Kingdom Coordinating Committee on Cancer Research guidelines.

6.2.3. Capturing of CTCs from whole blood of a metastasis mouse model using MCL,

the magnetic capture column, and the size-selective capture filter

We captured the CTCs from whole blood in a metastasis mouse model using the magnetic capture column and the size-selective capture filter, as described previously [24]. We developed mice CTC models bearing COLM5-EGFP cells and prepared MCLs as described previously [25, 33]. Approximately 1 mL of whole blood was 5-fold diluted with PBS and then incubated for 10 minutes with MCLs at a total amount of 10 μg magnetite for magnetic labeling.

Magnetically-labeled blood sample containing CTCs was loaded into the magnetic capture column with neodymium cuboid magnets (437 mT, Magfine, Miyagi, Japan) at 0.5 mL/min using a syringe pump (KDS100, KD Scientific, MA, USA). Then, the size-selective filter setting in Swinnex Filter Holder (13mm, Merck Millipore, Darmstadt, Germany) was added to the column after detaching the magnet from the column, and magnetically captured cells were sorted using a syringe pump (kd Scientific) with 3 mL of PBS at 0.5 mL/min. The captured EGFP-positive cells on the size-selective filter were observed and counted using a fluorescent microscope (Model IX81). The captured EGFP-positive cells were recovered from the filter by a reverse-flow using 2 mL DMEM at a flow rate of 10 mL/min.

The capturing experiment of CTCs was performed three times for culturing with or without a fibroblast sheet and magnetic attraction, respectively (**Table 6-1**, Experimental No. 1-3 for culturing with both fibroblast and magnetic attraction, Experimental No. 4-6 for culturing with magnetic attraction and without fibroblast, Experimental No. 7-9 for culturing without both fibroblast and magnetic attraction, respectively).

6.2.4. Culturing the captured CTCs on a fibroblast sheet

The fibroblast sheet was used as a feeder cell for enhancing CTC adhesion and proliferation. We used NIH-3T3 as a model fibroblast. 5×10^6 cells of NIH-3T3 was seeded

into a gas-permeable tissue culture dish (hydrophilic lumox dish, 35 mm, SARSTEDT, Nümbrecht -Rommelsdorf, Germany), and was cultured until confluent to form a fibroblast sheet. Then, the cells were treated with 10 µg/mL mitomycin C (Wako, Tokyo, Japan) in the medium for 1.5 h to inhibit the proliferation, and washed by phosphate buffered saline (PBS). Mitomycin C was used to become easily the isolation of CTCs to the contaminated fibroblast in the further passages.

The pin-holder device was fabricated to enhance the adhesion of the captured CTCs on a fibroblast sheet effectively and to isolate the CTCs by the profile of their magnetic distribution [33, 35, 36]. The pin-holder device has a base of magnetic soft iron, measuring 20 mm wide × 20 mm long × 10 mm high, and the array of square-pole type pillars with dimensions of 100 µm wide × 100 µm long × 320 µm high at intervals of 150 µm with center-to-center spacing of 250 µm. The magnetic field was concentrated on the pillars using an external neodymium disc magnet (50 mm in diameter and 10 mm in height with a surface magnetic induction of 0.38 T; Niruko Factories Co., Shiga, Japan).

A culture dish with or without a fibroblast sheet placed on the pin-holder device with the magnet, and was added the whole amount of recovered DMEM including CTCs for arrangement of magnetically labeled CTCs. After arrangement at 37°C for 1 h, the dish was then removed from the pin-holder device and magnet, and cultured CTCs with or without a fibroblast sheet. The time-lapse monitoring was performed using phase-contrast microscopy (Model IX81; Olympus, Tokyo, Japan) during the culture. After 12 days of culture with or without a fibroblast sheet, the numbers of the adhesive cells and the grown cells were counted by fluorescent microscopy (Model IX81; Olympus). The adhesive and grown rates of CTC were calculated as follows:

Adhesive rate [%] = (Number of captured cells [cells]) / (Number of adhesive cell numbers on a culture surface [cells]) × 100.

Grown rate [%] = (Number of captured cells [cells]) / (Number of grown cell numbers [cells]) × 100.

6.2.5. Isolation of grown CTC-derived cell

For isolation of the CTC-derived cell from one CTC, the each grown CTC-derived cell was picked-up and transferred using a micromanipulator (CellTram vario 5176, Eppendorf, Humberg, Germany) to a new fibroblast sheet in a gas-permeable tissue culture dish (35 mm, SARSTEDT) for the first culture, which was constructed as described above. After 18-21 days of culture, the grown CTC-derived cells were picked-up and transferred using a micromanipulator to a new 48 well plate (Greiner Bio One, Frickenhausen, Germany) without fibroblast for the second culture. After 14 days of culture, the grown CTC-derived cells were harvested with trypsin/EDTA, and were seeded into a new 10 cm culture dish without fibroblast for the third culture. The microscopic images of each grown CTC-derived cells in a 10 cm culture dish were obtained using a fluorescent microscope (Model IX81) after 5 passages in a 10 cm culture dish at least. Although we would picked-up the CTCs with some numbers of fibroblast from the fibroblast sheet, the contaminated fibroblasts could be decreased during the passages of CTCs by inhibition of the proliferation using mitomycin C.

6.2.6. Cell growth rate assay

Viable cells were identified by the trypan blue exclusion method, and cell counting was performed using a hemocytometer. To create the growth curve of CTC-derived cells, we seeded 2×10^5 cells into 10 cm culture dish. The numbers of the viable CTC-derived cells were counted by the trypan blue exclusion method in each time point, and were calculated the relative cell number compared to that of COLM5-EGFP. The doubling time and the relative growth rate were calculated from this growth curve.

6.2.7. Invasion assay

Invasive ability of CTC-derived cells into the lower compartment with serum-containing culture media was quantified in a transwell assay (8 μm inserts for 24-well plates, BD Biosciences, Bedford, MA, USA). We seeded 2×10^5 of CTC-derived cells into the upper compartment with serum-free DMEM, and set it on the lower compartment with 10% FBS-containing DMEM. After 24 h of culture, the invaded cells to the lower component were estimated using Cell Counting Kit-8 assay (Dojindo Laboratories, Mashiki-machi, Kumamoto, Japan) according to the manufacturer's protocol. Optical density (OD) at 450 nm (formation of formazan) was measured using Fluoroskan Ascent Microplate Fluorometer (Thermo Scientific, Waltham, MA, USA). Cell counts were indirectly estimated from a standard curve generated using solutions of known cell counts: 0, 1×10^2, 5×10^2, 1×10^3, 5×10^3, and 1×10^4 cells per well. The relative numbers of invaded CTC-derived cells were calculated from the numbers of invaded cells compared to that of COLM5-EGFP, as a control cell.

6.2.8. Drug resistant assay

To evaluate the drug-resistant ability of CTC-derived cells, we seeded 2×10^3 cells/well into 96 well plate (Greiner Bio One), and were cultured in DMEM with 10 ng/mL of paclitaxel (Wako), as a model anti-cancer drug. After 48 h of culture, the viability of the cells was estimated using Cell Counting Kit-8 assay (Dojindo Laboratories), as described above. The survival rates of each CTC-derived cell were calculated from the viability compared to that of the non-treated viabilities. Then, the relative survival rates were calculated from these survival rates compared to that of COLM5-EGFP, as a control cell.

6.2.9. Gene expression analysis

Cells were washed with PBS, and lysed using lysis enhancer and resuspension buffer from CellsDirect One-step qRT-PCR kits (Invitrogen). Real-time RT-PCR assays were conducted on an ABI StepOne Real Time PCR Systems, using SYBR Green RNA 1step kit (Applied Biosystems, Branchburg, NJ, USA). Primers were purchased from Greiner Bio One. The sequences of the primers are listed in **Table 6-2**. The comparative threshold cycle (Ct) method was used to quantify gene expression in each sample. Normalization of gene expression was performed using GAPDH as a reference gene, and all data was expressed as a ratio to the reference sample of COLM5-EGFP.

6.2.10. Statistical Analysis

The statistical significance of differences in data between groups was determined by applying Student's t-test or Welch's two-tailed t-test.

6.3. Results

6.3.1. Co-culture of magnetically captured CTCs on a fibroblast feeder layer

CTCs in whole blood of COLM5-EGFP-bearing metastatic mice were captured by using a magnetic capture column and a size-selective filter device as we reported previously (**Fig. 6-1A**) [21]. Then, the captured magnetically labeled CTCs were transferred to the cell culture dish with a fibroblast feeder layer placed on the magnet (**Fig. 6-1B**). With a feeder layer, 31 cells out of captured 36 single CTCs adhered on the feeder layer and among them, 4 cells proliferated (**Fig. 6-2** and Experiment No. 1-3 in **Table 6-1**). On the contrary, without a feeder layer, no cells adhered and proliferated out of magnetically captured 59 or 82 single CTCs with or without the magnetic attraction, respectively (Experiment No. 4-6 and No. 7-9 in **Table 6-1**, respectively). These results indicated that a fibroblast feeder layer was important to enhance adhesion and proliferation for CTC culturing.

6.3.2. Cloning culture of proliferated CTCs

Since we obtained 4 colonies of the proliferated CTCs on a fibroblast feeder layer, we next picked them up and transferred to the new cell culture dish with a feeder layer respectively by using a micromanipulator. The colony sizes derived from different 4 CTCs increased by the day and after 18-21 days, the grown CTC-derived cells were picked up and transferred to a new 48 well plate without a fibroblast layer by using a micromanipulator. Since the growth of one of four CTC-derived cells was stopped at this step, we subsequently cultured three CTC-derived cells. The morphologies of the three CTC-derived cells (CTC1, CTC2, and CTC3) after 5 passages were shown in **Fig. 6-3A**. We found that the proliferation of all three CTC-derived cells was slower than that of the parental COLM5-EGFP cells (**Fig. 6-3B**). The doubling times of COLM5-EGFP cells, CTC1, CTC2, and CTC3 were 2.18, 6.56, 7.35, and 7.57 days, respectively.

6.3.3. Phenotypic analysis of the CTC-derived cells

Since cloning culture of three CTC-derived cells was succeeded, we next demonstrated their phenotypic analysis and gene expression analysis in combination. These analyses cannot be performed with single CTCs as they are captured.

For the phenotypic analysis, the invasion assay and drug test against PTX, a model anti-cancer agent, were performed. The invasive ability of all three CTC-derived cells was significantly increased than that of the original COLM5-EGFP cells; relative number of invaded cells was 1.2 ± 0.06 for CTC1, 1.1 ± 0.03 for CTC2, and 1.4 ± 0.07 for CTC3 (**Fig. 6-4A**). For the drug test against PTX, the survival rate of CTC-derived cells was significantly higher than that of the COLM5-EGFP cells for all CTC-derived cells (1.3 ± 0.04 for CTC1, 1.3 ± 0.01 for CTC2, and 1.5 ± 0.01 for CTC3) (**Fig. 6-4B**).

Since the activated invasive and drug-resistance abilities were observed (**Fig. 6-4**), we evaluated the genetic expressions of the genes relating to the invasive or drug-resistance ability in the CTC-derived cells. We measured the gene expression of VEGF, MMP-2, and E-cadherin reported as the invasion-related genes, and MDR-1 reported as the drug-resistance-related gene. VEGF and MMP-2 were increased the invasive and metastatic capacities of cancer cell [35, 36], and loss of E-cadherin expression has been found to correlate with an invasive phenotype in many carcinomas [37]. MDR-1 is the most common cause of multidrug resistance, including paclitaxel, in many types of solid and hematological human cancers [35-38].

Fig. 6-5 shows the relative expressions of each gene in the CTC-derived cells compared to that in the original COLM5-EGFP cells. As expected from the results of phenotypic analysis (**Fig. 6-4**) and the other studies [35-38], the expression levels of VEGF, MMP-2, and MDR-1 in CTC-derived cells were significantly higher than that in original COLM5-EGFP cells and the expression level of E-cadherin in CTC-derived cells were significantly lower than that in the original cells, excepting for that of VEGF and E-cadherin in CTC1.

6.4. Discussion

In the present study, we developed an *in vitro* co-culture method of CTCs with a fibroblast feeder layer by a magnetic force-based co-culture method. We found that the fibroblast layer enhanced the adhesion and supported the proliferation of the captured CTCs (**Fig. 6-2** and **Table 6-1**). We could clone three CTC-derived cells from single CTCs, and evaluate the malignant changes of their phenotypes, including the invasive capacity (**Fig. 4A**) and drug resistance (**Fig. 4B**). The mRNA expressions of invasion-related genes (VEGF and MMP-2) and drug resistance-related gene (MDR-1) increased and that of adhesion molecule gene (E-cadherin) decreased in CTC-derived cells (**Fig. 6-5**).

The use of a fibroblast feeder layer realized effective *ex vivo* culture of CTC-derived cells (**Figs. 6-2-6-4** and **Table 1**). It has been reported that the interaction with fibroblasts enhanced the survival capacity, adhesion, and proliferation of stem cells including induced pluripotent stem cells and many cancer cell lines [28-33]. Fibroblasts synthesize many ECMs such as type I-, type III-, type V-collagen, and fibronectin, and form basement membranes for adhesion of cancer cells [31]. Also, cancer associated-fibroblasts secrete several growth factors such as hepatocyte growth factor, insulin-like growth factor, epidermal growth factor, and fibroblast growth factor-2, and induce proliferative signals to cancer cells [31]. Although, further experiments are needed to reveal which molecules are involved in the process of CTC-derived cells culture, this co-culture method using a fibroblast feeder layer would be promising to support CTCs adhesion and proliferation for performing phenotype-based analyses.

We obtained three CTC-derived cells and investigated the phenotypic changes including invasive- and drug-resistance-abilities (**Fig. 6-4**). We also performed gene expression analysis of the genes relating to those abilities; the expressions of VEGF, MMP-2 and MDR-1 were activated, and the expression of E-cadherin was inactivated in CTC derived cells (**Fig. 6-5**). VEGF is an angiogenesis-inducible factor and MMP-2 is the gelatinases (72 kD type IV collagenase). Overexpression of VEGF or MMP-2 increased the invasive and metastatic capacities of cancer cell [35, 36]. MDR-1 which leads to the production of ATP-driven efflux transporter Pgp-170 is the most common cause of multidrug resistance in many types of solid and hematological human cancers [38]. These results indicated that the malignancy of the CTC-derived cells were higher than that of COLM5-EGFP cells which were used to form original tumors in metastatic model mice.

Mutations in CTCs had reported in many cancer patients, such as a tumor suppressor gene TP53 mutation in breast cancer [39] and β-catenin mutation in primary liver cancer [13].

Also, the mutant populations of KRAS, BRAF, CD133, and Plastin3 in CTCs from colorectal cancer patients highly correlated to that in the primary tumor [40]. The expressions of VEGF, MMP-2, and MDR-1 were activated by NF-κB signaling playing important roles in tumor resistance to chemotherapy [41-45]. These results suggest that the changes in malignancy might be caused by some mutations in some signaling pathways and/or by condensation of specific cell populations during the primary tumor formation and/or the invasion and metastasis process from the tumor, and further analysis on involvement of the NF-κB signaling would give us more insight to understand this malignancy change.

We also observed the decrease of proliferation in the CTC-derived cells (Fig.3C). Proliferation decrease in metastatic focus which was generated from CTCs have sometimes been observed both in metastatic mice models and patients [46]. Pence *et al*. also said that proliferation change was not a central mechanism of metastasis since the same primary tumor can generate metastatic focus with higher, lower, or similar proliferations [47]. Thus, we considered that the observed changes on the invasion or gene expressions of the CTC-derived cells in our study were not related the proliferative feature.

The CTC-derived cells could make a tumor after injection into the back and lower abdominal flanks of mice, but the expansion rates were decreased than that of the parental COLM5-EGFP (data not shown). This result indicated that phenotype-based proliferation analysis for a number of CTCs might predict the expansion rate of metastatic focus. Summarizing the above, the invasiveness might be one of importance to increase CTC appearance and/or tumorigenesis compared to the raise of proliferation. In addition, some mice which were injected CTC-derived cell in were revealed peritoneal metastasis (data not shown), though the parental COLM5-EGFP mainly metastasized to lung or liver. Thus, the CTC-derived cell might be changed the organ affinity via invasion and/or in primary tumor.

Previously, we have developed the combination process of a magnetic capture column

and a size-selective 3D palladium filter device for cell surface marker independent CTCs isolation method. In this process, MCLs were added to the samples to achieve more than 10 ng-magnetite/cell of magnetic labeling efficiency to capture the cells by the magnetic capture column [21]. In the present study, we made good use of the magnetically labeled CTCs and demonstrated the magnetic co-culture of CTC-derived cells on the fibroblasts feeder layer. Thus, we developed the subsequent bioprocess for the effective CTCs isolation and culture.

The toxicity of MCLs consisting of magnetite nanoparticles and cationic liposomes against cells is an important issue for clinical diagnostics applications of our developed *ex vivo* culturing method for CTCs. Previously, we confirmed that the growth of COLM5-EGFP cells was not inhibited by the magnetic labeling of MCLs at a magnetite concentration of 100 pg-magnetite/cell and below, and the viability of spiked human cancer cells labeled with MCLs were not decreased by the capturing and filtering process (98.8 ± 1.1% for before and 97.6 ± 0.9% for after) [21]. Furthermore, several groups, including our group, also show that the MCLs do not affect the viability, proliferation or differentiation of other cell types within the magnetite concentration tested [24, 25, 27, 48-51]. Considering these results, the viability and proliferation of CTCs in clinical samples would not be inhibited by MCLs at the condition used in the present study.

In conclusion, the *ex vivo* culture method of CTCs using a fibroblast feeder layer and magnetic force was developed in this study. We demonstrated that the culturing process using MCLs combined with the magnetically- and size-selective-capturing is a valuable analysis tool for phenotype-based characters of CTCs. Therefore, our process is a highly applicable to evaluate phenotype-based malignancies of CTCs for cancer therapy.

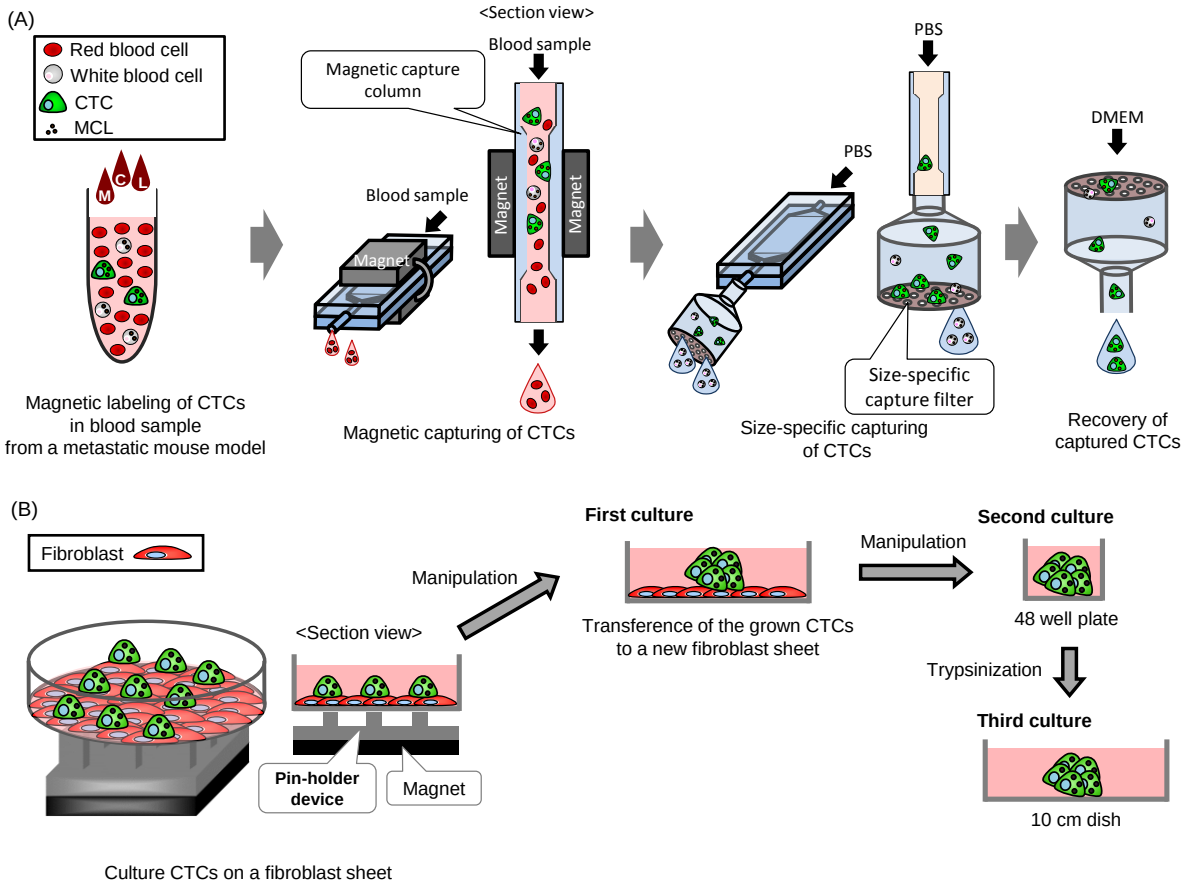

Fig. 6-1. Schematic diagram for culturing of circulating tumor cell (CTC) using a fibroblast sheet and a pin-holder device (A) Schematic diagram of magnetic column combined with size-selective filter for circulating tumor cell (CTC) capture. CTCs in a blood sample were magnetically labeled by MCL. Then, the CTCs were magnetically and size-selective captured using a magnetic column and a size-selective filter. (B) Schematic diagram for culturing of captured CTCs using a fibroblast feeder layer and a pin-holder device. The captured CTCs were attracted and isolated on a fibroblast layer using magnetic force distribution by a pin-holder device with a magnet. The proliferated CTCs were transferred to a next culture dish using micromanipulator for the first- and second-culture, or using trypsinization.

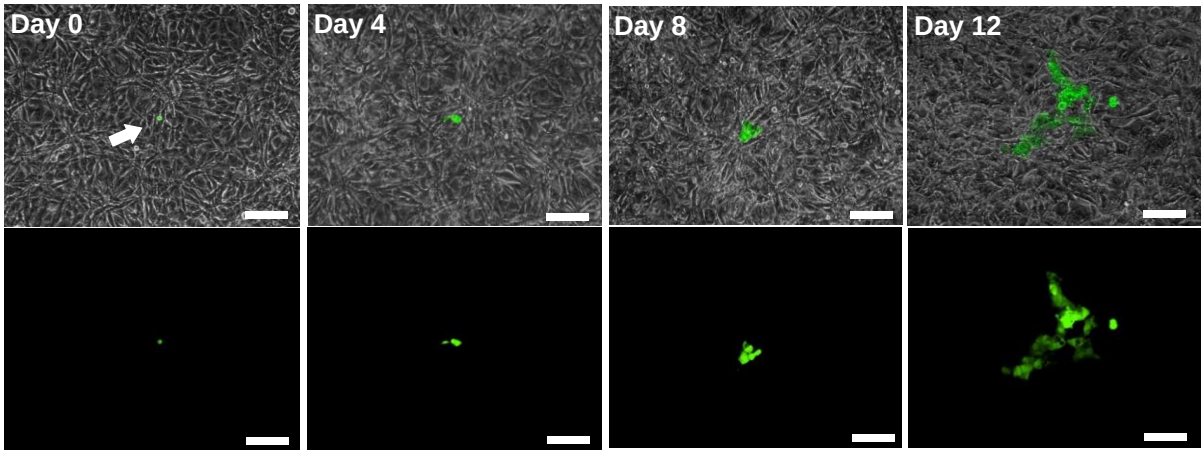

Fig. 6-2. Time-lapse images of representative captured EGFP-positive cells from whole blood of tumor bearing mice during co-culturing on a fibroblast sheet The captured EGFP-positive cells were attracted and isolated using a pin-holder device, and were cultured on a fibroblast sheet. Lower images shows the EGFP-fluorescent images of the captured EGFP-positive cells from blood of COLM5-EGFP-bearing mice which was grown on a fibroblast sheet, and upper panels show the overlay images. Scale bars: 100 μm.

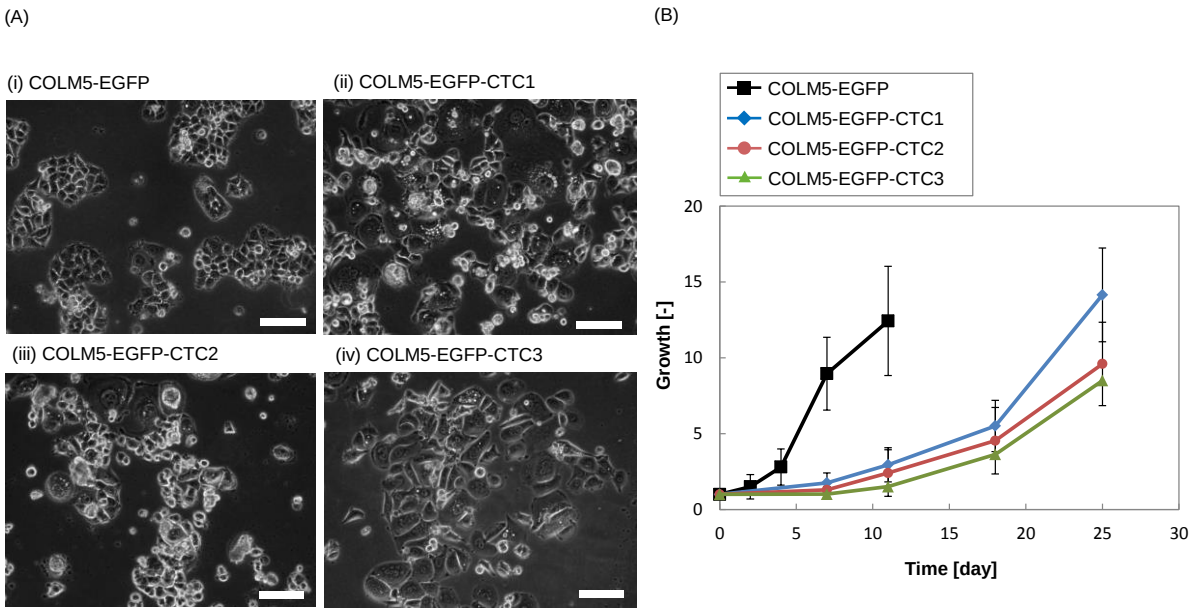

Fig. 6-3. Microscopic images and growth curve of the CTC-derived cells (A) Microscopic images of the original cancer cell line COLM5-EGFP (i) and the CTC-derived cells (ii-iv) which were cultured in a culture dish. Scale bars: 100 µm. (B) Growth curve of the CTC-derived cells (COLM5-EGFP-CTC1-3), and the original cancer cell line (COLM5-EGFP) in a culture dish. Data are presented as mean ± SD, n = 3.

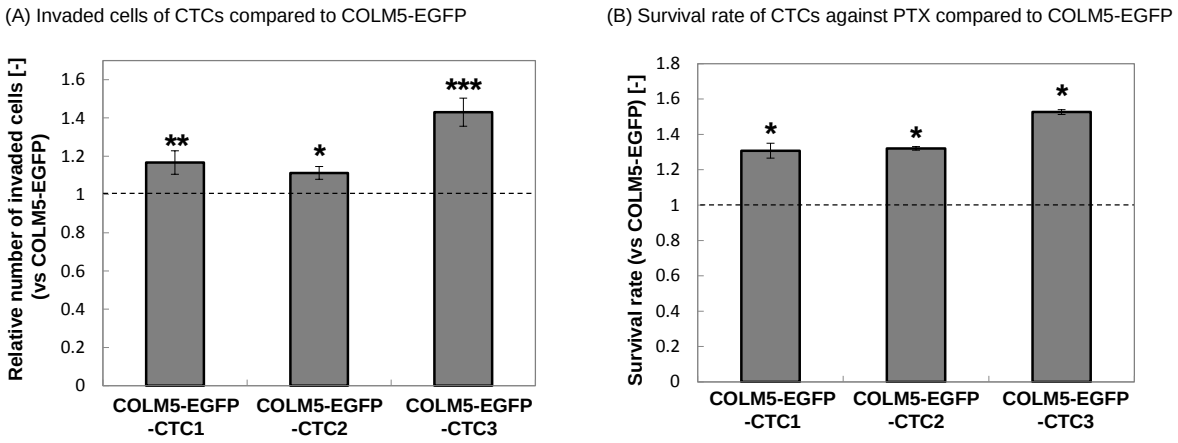

Fig. 6-4. Invasive capacity and drug-resistance ability of the CTC-derived cells (A) Relative cell numbers of the invaded CTC-derived cells using transwell assay. The number of invaded CTC-derived cells was normalized to that of COLM5-EGFP. Data are presented as mean ± SD, n = 3. Asterisks indicate that the *p*-value was regarded as a significant difference compared to that of COLM5-EGFP, as the control group (* $p < 0.05$, ** $p < 0.01$, *** $p < 5\times10^{-3}$). (B) Survival rate of CTC-derived cells against 10 ng/mL of paclitaxel (PTX), as a model anti-cancer drug. The number of the survival CTC-derived cells was normalized to that of COLM5-EGFP. Data are presented as mean ± SD, n = 3. Asterisks indicate that the *p*-value was regarded as a significant difference compared to that of COLM5-EGFP, as the control group (* $p < 0.05$).

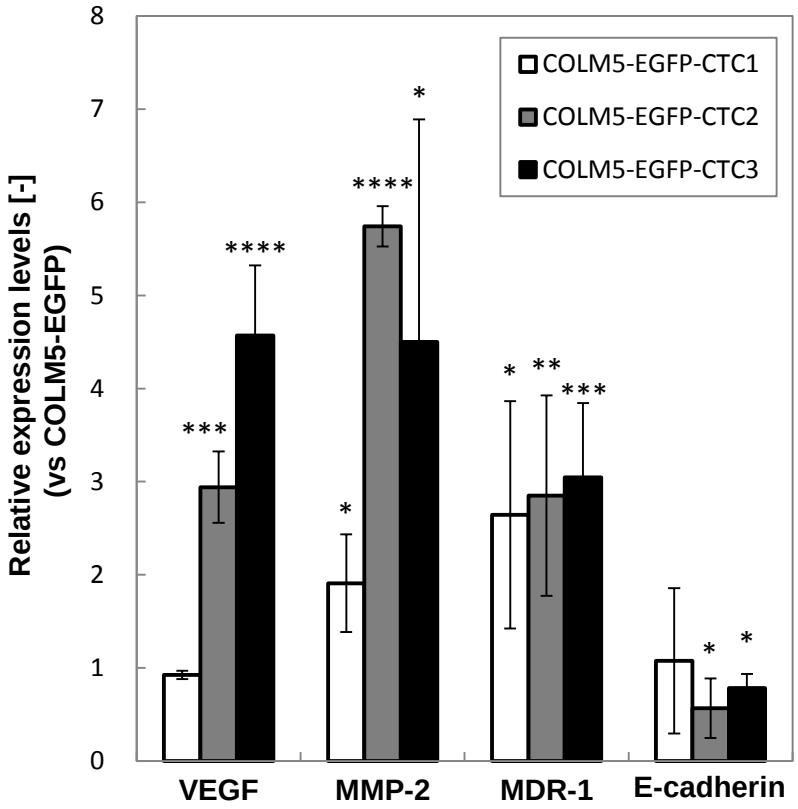

Fig. 6-5. Relative expression of invasion- and drug-resistance-related genes in the CTC-derived cells Expression data was normalized to each gene expressions found in COLM5-EGFP using GAPDH as the reference. Data are presented as mean ± SD, n = 3. Asterisks indicate that the *p*-value was regarded as a significant difference compared to that of COLM5-EGFP, as the control group (* p <0.05, ** p <0.01, *** p <5×10^{-3}, **** p <5×10^{-5}).

Table 6-1. Numbers of captured, adhesive and proliferative CTC-derived cells on a fibroblast feeder layer.

Experimental No.	Magnetic force	Fibroblasts	Cell number [cells]		
			Captured cells	Adhered cells	Proliferated cells
1	+	+	8	8	1
2	+	+	12	8	2
3	+	+	16	15	1
		Average	12	10.3 (86.1%)	1.3 (10.8%)
4	+	-	23	0	0
5	+	-	16	0	0
6	+	-	20	0	0
		Average	19.7	0	0
7	-	-	15	0	0
8	-	-	46	0	0
9	-	-	21	0	0
		Average	27.3	0	0

Table 6-2. Sequences of primers for RT-PCR.

	Forward (5’-3’)	Reverse (5’-3’)
GAPDH	CCTGACCTGCCGTCTAGAAA	TGCTGTAGCCAAATTCGTTG
VEGF	ATGAACTTTCTGCTGTCTTGGGT	TGGCCTTGGTGAGGTTTGATCC

MMP-2	GCTGGCTGCCTTAGAACCTTTC	GAACCATCACTATGTGGGCTGAGA
MDR-1	GACAGATATCTTTGCAAATGCAGG	GCCATTGACTGAAAGAACATTCC
E-cadherin	GTGACTGATGCTGATGCCCCCAATACC	GACGCAGAATCAGAATTAGGAAAGCAAG

6.5. Summary

Phenotype-based analysis of circulating tumor cells (CTCs) is a potent and promising approach to reveal new therapeutic targets and to understand biological properties of CTCs. However, *ex vivo* culturing of CTCs is still technically challenging. In the present study, we developed a novel *ex vivo* culture method for CTCs using a fibroblast feeder layer and a magnetic co-culture method. CTCs in the blood of metastatic model mice were labeled magnetically with magnetite cationic liposomes (MCLs). The magnetically labeled CTCs were isolated by the combination process of a magnetic capture column and a size-selective capture filter device, which we reported previously. The isolated CTCs were forced to be positioned on a fibroblast feeder layer by magnetic force. As results, we observed the adhesion and proliferation of the CTCs in the condition with a fibroblast feeder layer and a magnetic force, whereas no adhesion and proliferation were observed without feeder layer. Subsequently, we cultured the CTCs and obtained three CTC-derived cells. Using the CTC-derived cells, we performed the phenotype-based analyses for investigating invasive- and drug resistant-abilities and found that the CTC-derived cells had higher malignancy than that of original cells. Thus, the developed method using a fibroblast layer would be a promising approach of *ex vivo* culture of CTCs for evaluating their phenotype-based malignancies for cancer therapy.

6.6. References

1 Yu M, Bardia A, Aceto N, *et al*. *Ex vivo* culture of circulating breast tumor cells for individualized testing of drug susceptibility. *Science*. 2014; **345**: 216-220.

2 Nadal R, Fernandez A, Sanchez-Rovira P, *et al*. Biomarkers characterization of circulating tumour cells in breast cancer patients. *Breast Cancer Res*. 2012; **14**: 12.

3 Sandri MT, Zorzino L, Cassatella MC, *et al*. Changes in circulating tumor cell detection in patients with localized breast cancer before and after surgery. *Ann Surg Oncol*. 2010; **17**: 1539-1545.

4 Pantel K, Brakenhoff RH. Dissecting the metastatic cascade. *Nat Rev Cancer*. 2004; **4**: 448-456.

5 Krebs MG, Hou JM, Sloane R, *et al*. Analysis of circulating tumor cells in patients with non-small cell lung cancer using epithelial marker-dependent and -independent approaches. *J Thorac Oncol*. 2012; **7**: 306-315.

6 Cristofanilli M, Budd GT, Ellis MJ, *et al*. Circulating tumor cells, disease progression, and survival in metastatic breast cancer. *N Engl J Med*. 2004; **351**: 781-791.

7 Lu CY, Tsai HL, Uen YH, *et al*. Circulating tumor cells as a surrogate marker for determining clinical outcome to mFOLFOX chemotherapy in patients with stage III colon cancer. *Br J Cancer*. 2013; **108**: 791-797.

8 Thalgott M, Rack B, Maurer T, *et al*. Detection of circulating tumor cells in different stages of prostate cancer. *J Cancer Res Clin Oncol*. 2013; **139**: 755-763.

9 Liu MC, Shields PG, Warren RD, *et al*. Circulating tumor cells: A useful predictor of treatment efficacy in metastatic breast cancer. *J Clin Oncol*. 2009; **27**: 5153-5159.

10 Lucci A, Hall CS, Lodhi AK, *et al*. Circulating tumour cells in non-metastatic breast cancer: a prospective study. *Lancet Oncol*. 2012; **13**: 688-695.

11 Went PT, Lugli A, Meier S, *et al*. Frequent EpCam protein expression in human

carcinomas. *Human Pathol*. 2004; **35**: 122-128.

12 Sieuwerts AM, Kraan J, Bolt J, *et al*. Anti-epithelial cell adhesion molecule antibodies and the detection of circulating normal-like breast tumor cells. *J Natl Cancer Inst*. 2009; **101**: 61-66.

13 Vona G, Estepa L, Beroud C, *et al*. Impact of cytomorphological detection of circulating tumor cells in patients with liver cancer. *Hepatology*. 2004; **39**: 792-797.

14 Yu M, Bardia A, Wittner B, *et al*. Circulating breast tumor cells exhibit dynamic changes in epithelial and mesenchymal composition. *Science*. 2013; **339**: 580-584.

15 Hosokawa M, Hayata T, Fukuda Y, *et al*. Size-selective microcavity array for rapid and efficient detection of circulating tumor cells. *Anal Chem*. 2010; **82**: 6629-6635.

16 Vona G, Sabile A, Louha M, *et al*. Isolation by size of epithelial tumor cells: a new method for the immunomorphological and molecular characterization of circulatingtumor cells. *Am J Pathol.* 2000; **156**: 57-63.

17 Desitter I, Guerrouahen BS, Benali-Furet N, *et al*. A new device for rapid isolation by size and characterization of rare circulating tumor cells. *Anticancer Res.* 2011; **31**: 427-441.

18 Yusa A, Toneri M, Masuda T, *et al*. Development of a new rapid isolation device for circulating tumor cells (CTCs) using 3D Palladium filter and its application for genetic analysis. *PLoS One*. 2014; **9**: 11.

19 Ozkumur E, Shah AM, Ciciliano JC, *et al*. Inertial focusing for tumor antigen-dependent and -independent sorting of rare circulating tumor cells. *Sci Transl Med*. 2013; **5**: 11.

20 Ameri K, Luong R, Zhang H, *et al*. Circulating tumour cells demonstrate an altered response to hypoxia and an aggressive phenotype. *Br J Cancer.* 2010; **102**: 561-569.

21 Yamamoto S, Fei J, Mina O, *et al*. Efficient capturing of circulating tumor cells using a magnetic capture column and a size-selective filter, *Bioprocess Biosyst Eng*, 2015; **38**:

1693-1704.

22 Ino K, Okochi M, Honda H. Application of magnetic force-based cell patterning for controlling cell-cell Interactions in angiogenesis. *Biotechnol Bioeng*. 2009; **102**: 882-890.

23 Okochi M, Takano S, Isaji Y, *et al*. Three-dimensional cell culture array using magnetic force-based cell patterning for analysis of invasive capacity of BALB/3T3/v-src. *Lab Chip*. 2009; **9**: 3378-3384.

24 Yamamoto S, Hotta MM, Okochi M, *et al*. Effect of vascular formed endothelial cell network on the invasive capacity of melanoma using the *in vitro* 3D co-culture patterning model. *PLoS One*. 2014; **9**: e103502.

25 Shimizu K, Ito A, Yoshida T, Yamada Y, *et al*. Bone tissue engineering with human mesenchymal stem cell sheets constructed using magnetite nanoparticles and magnetic force. *J Biomed Mater Res B Appl Biomater*. 2007; **82B**: 471-480.

26 Okochi M, Matsumura T, Yamamoto S, *et al*. Cell behavior observation and gene expression analysis of melanoma associated with stromal fibroblasts in a three-dimensional magnetic cell culture array. *Biotechnol Prog*. 2013; **29**: 135-142.

27 Yamamoto S, Okochi M, Jimbow K, *et al*. Three-dimensional magnetic cell array for evaluation of anti-proliferative effects of chemo-thermo treatment on cancer spheroids. *Biotechnol Bioprocess Eng*. 2015; **20**: 488-497.

28 Takahashi K, Narita M, Yokura M, *et al*. Human induced pluripotent stem cells on autologous feeders. *PLoS One*. 2009; **4**: 6.

29 Zhou Y, Mao HL, Joddar B, *et al*. The significance of membrane fluidity of feeder cell-derived substrates for maintenance of iPS cell stemness. *Sci Rep*. 2015; **5**: 13.

30 Olaso E, Santisteban A, Bidaurrazaga J, *et al*. Tumor-dependent activation of rodent hepatic stellate cells during experimental melanoma metastasis. *Hepatology*. 1997; **26**: 634-642.

31 Kalluri R, Zeisberg M. Fibroblasts in cancer. *Nat Rev Cancer*. 2006; **6**: 392-401.

32 Erez N, Truitt M, Olson P, *et al*. Cancer-associated fibroblasts are activated in incipient neoplasia to orchestrate tumor-promoting inflammation in an NF-kappa B-dependent manner. *Cancer Cell*. 2010; **17**: 135-147.

33 Martinez-Outschoorn UE, Trimmer C, Lin Z, *et al*. Autophagy in cancer associated fibroblasts promotes tumor cell survival Role of hypoxia, HIF1 induction and NF kappa B activation in the tumor stromal microenvironment. *Cell Cycle*. 2010; **9**: 3515-3533.

34 Ito Y, Nakanishi H, Kodera Y, *et al*. Characterization of a novel lymph node metastasis model from human colonic cancer and its preclinical use for comparison of anti-metastatic efficacy between oral S-1 and UFT/ LV. *Cancer Sci*. 2010; **101**: 1853-1860.

35 Takahashi Y, Kitadai Y, Bucana CD, *et al*. Expression of vascular endothelial growth-factor and its receptor, KDR, correlates with vascularity, metastasis, and proliferation of human colon-cancer. *Cancer Res*. 1995; **55**: 3964-3968.

36 Kurschat P, Wickenhauser C, Groth W, *et al*. Identification of activated matrix metalloproteinase-2 (MMP-2) as the main gelatinolytic enzyme in malignant melanoma by in situ zymography. *J Pathol*. 2002; **197**: 179-187.

37 Nakajima S, Doi R, Toyoda E, *et al*. N-cadherin expression and epithelial-mesenchymal transition in pancreatic carcinoma. *Clin Cancer Res*. 2004; **10**: 4125-4133.

38 Viale M, Cordazzo C, Cosimelli B, *et al*. Inhibition of MDR1 activity *in vitro* by a novel class of diltiazem analogues: Toward new candidates. *J Med Chem*. 2009; **52**: 259-266.

39 Fernandez SV, Bingham C, Fittipaldi P, *et al*. TP53 mutations detected in circulating tumor cells present in the blood of metastatic triple negative breast cancer patients. *Breast Cancer Res*. 2014; **16**: 445.

40 Lyberopoulou A, Aravantinos G, Efstathopoulos EP, *et al*. Mutational analysis of

circulating tumor cells from colorectal cancer patients and correlation with primary tumor tissue. *PLoS One*. 2015; **10**: e0123902.

41 Wang YH, Dong YY, Wang WM, *et al*. Vascular endothelial cells facilitated HCC invasion and metastasis through the Akt and NF-kappa B pathways induced by paracrine cytokines. *J Exp Clin Cancer Res*. 2013; **32**: 11.

42 Chen GQ, Goeddel DV. TNF-R1 signaling: A beautiful pathway. *Science*. 2002; **296**: 1634-1635.

43 Oeckinghaus A, Hayden MS, Ghosh S. Crosstalk in NF-kappa B signaling pathways. *Nature Immunol*. 2011; **12**: 695-708.

44 Beyaert R, Cuenda A, VandenBerghe W, *et al*. The p38/RK mitogen-activated protein kinase pathway regulates interleukin-6 synthesis in response to tumour necrosis factor. *Embo J*. 1996; **15**: 1914-1923.

45 Wang W, Nag SA, Zhang R. Targeting the NFκB signaling pathways for breast cancer prevention and therapy. *Curr Med Chem*. 2015; **22**: 264-289.

46 Lu X, Yan CH, Yuan M, *et al*. *In vivo* dynamics and distinct functions of hypoxia in primary tumor growth and organotropic metastasis of breast cancer. *Cancer Res*. 2010; **70**: 3905-3914.

47 Pence JC1, Kizilbash AM, Kerns BJ, *et al*. Proliferation index in various stages of breast cancer determined by Ki-67 immunostaining. *J Surg Oncol*. 1991; **48**: 11-20.

48 Ito A, Ino K, Hayashida M, *et al*. Novel methodology for fabrication of tissue-engineered tubular constructs using magnetite nanoparticles and magnetic force. *Tissue Eng*. 2005; **11**: 1553-1561.

49 Shimizu K, Ito A, Lee JK, *et al*. Construction of multi-layered cardiomyocyte sheets using magnetite nanoparticles and magnetic force. *Biotechnol Bioeng*. 2007; **96**: 803-809.

50 Shimizu K, Ito A, Honda H. Mag-seeding of rat bone marrow stromal cells into porous

hydroxyapatite scaffolds for bone tissue engineering. *J Biosci Bioeng.* 2007; **104**: 171-177.

51 Horie M, Ito A, Maki T, *et al*. Magnetic separation of cells from developing embryoid bodies using magnetite cationic liposomes. *J Biosci Bioeng.* 2011; **112**: 184-187.

Chapter 7

Concluding remarks

In vitro cell culture models have attracted great attention for understanding the malignancy process, drug screening, and medical diagnostics of various cancers. In this thesis, I aimed to develop 3D *in vitro* cancer cell spheroid arrays using a magnetic cell patterning method for understanding the malignancy process and drug test, and to construct an *ex vivo* culture method for CTCs.

In the **Chapter 1**, a general introduction covering the importance of *in vitro* cancer models in understanding of cancer malignancy process and drug screening were discussed. Considering to these backgrounds, I also described the objective of this thesis.

In the **Chapter 2**, 3D cell culture arrays of melanoma cell spheroids were assembled to evaluate the combined effect of a melanogenesis-targeting drug, NPrCAP, and heat treatment, as a model of anti-cancer treatment. An array-like multicellular pattern of mouse melanoma B16F1 spheroids in a collagen gel was established by magnetic cell labeling using a pin-holder device to exert a magnetic force. As a result, melanogenesis of B16F1 cells was 29-fold higher in this 3D array than in conventional 2D monolayer cultures. Because the spheroid size was linearly correlated with the cell number within a spheroid, the

anti-proliferative effect could be evaluated in a non-destructive manner. Moreover, the half-maximal inhibitory concentration of NPrCAP coupled with heat treatment calculated from the spheroid size was 2-fold higher in the 3D array than in 2D culture. These results indicate that spheroid formation decreases the chemosensitivity of cancer cells, and this model would be suitable as a susceptibility assay for melanogenesis-targeting drugs. Therefore, this 3D culture model provides a better screening format to evaluate drug and physical treatments for cancer therapy than 2D formats.

In the **Chapter 3**, a 3D multicellular tumor spheroid culture array has been fabricated to analyze the effect of stromal fibroblast on the invasive capacity of melanoma. The interaction of fibroblast on the invasion of human melanoma cell (M-1) was investigated using three types of cell interaction models: (i) fibroblasts were magnetically labeled and patterned together in array with melanoma spheroids (direct-interaction model), (ii) fibroblasts coexisting in the upper collagen gel (indirect-interaction model) of melanoma spheroids, and (iii) fibroblast sheets coexisting under melanoma spheroids (fibroblast-sheet model). The fibroblast-sheet model has largely increased the invasive capacity of melanoma, and the promotion of adhesion, migration, and invasion were also observed. In the fibroblast-sheet model, the expression of IL-8 and MMP-2 increased by 24-fold and 2-fold, respectively, in real time RT-PCR compared to the absence of fibroblasts. Therefore, these results demonstrate the importance of fibroblast interaction to invasive capacity of melanoma in the 3D *in vitro* bioengineered tumor microenvironment.

In the **Chapter 4**, *in vitro* 3D cancer intravasation models were developed to observe the invasive capacity of melanoma cell spheroids co-cultured with the vascular-formed endothelial cell network. When the B16F1 patterned together with a vascular network of

human umbilical vein epithelial cells (HUVEC), spreading and progression were observed along the HUVEC network. The B16F1 cells over 80 μm distance from HUVEC remain in a compact spheroid shape, while B16F1 in the proximity of HUVEC aggressively changed their morphology and migrated. The mRNA expression levels of IL-6, MDR-1 and MMP-9 in B16F1 increased along with the distance from the HUVEC network, and these expressions were increased by 5, 3 and 2-fold in the B16F1 close to HUVEC (within 80 μm distance) as compared to that far from HUVEC (over 80 μm distance). Therefore, these results clearly suggested that malignancy of tumor cells is enhanced in proximity to vascular endothelial cells and leads to intravasation, than that of fibroblasts.

In the **Chapter 5**, a combined method using a magnetic capture column was developed for rapid and efficient isolation of CTCs, which were magnetically labeled with MCLs. In the capturing process, large volumes of blood containing magnetically labeled cancer cells were introduced into the column at a high flow rate to capture the cells, which were then flowed into the filter at a low flow rate. Our results show that the combined use of the column and filter decreased the required time for the spiked cancer cell capture, and the recovery rate of the spiked cancer cells from blood was significantly higher using the combination process (80.7%) than that using the filter alone (64.7%). Moreover, almost twice the number of CTCs could be captured from the blood of metastatic model mice by using the combination process. Therefore, the developed process would be useful for the rapid and efficient isolation of CTCs.

In the **Chapter 6**, a novel *ex vivo* culture method was developed for CTCs using a fibroblast feeder layer and a magnetic co-culture method. CTCs in the blood of metastatic model mice were labeled magnetically with MCLs. The magnetically labeled CTCs were

isolated by the combination process of a magnetic capture column and a size-selective capture filter device, shown in the **Chapter 5**. The isolated CTCs were forced to be positioned on a fibroblast feeder layer by magnetic force. As results, we observed the adhesion and proliferation of the CTCs in the condition with a fibroblast feeder layer and a magnetic force, whereas no adhesion and proliferation were observed without feeder layer. Subsequently, we cultured the CTCs and obtained three CTC-derived cells. Using the CTC-derived cells, we performed the phenotype-based analyses for investigating invasive- and drug resistant-abilities and found that the CTC-derived cells had higher malignancy than that of original cells. Thus, the developed method using a fibroblast layer would be a promising approach of *ex vivo* culture of CTCs for evaluating their phenotype-based malignancies for cancer therapy.

Finally, this thesis is considered to develop novel *in vitro* culture models for cancer research. I believe that these models will be utilized to clarify the mechanism of cancer malignant changes, such as invasiveness and drug resistance, and will be applied to drug screening tools.

List of publications for dissertation

1. Mina Okochi, Taku Matsumura, **Shuhei Yamamoto**, Eiji Nakayama, Kowichi Jimbow, Hiroyuki Honda: Cell Behavior Observation and Gene Expression Analysis of Melanoma Associated with Stromal Fibroblasts in a Three-Dimensional Magnetic Cell Culture Array. *Biotechnology Progress*, 29(1):135-142, 2013

2. **Shuhei Yamamoto**, Michael Masakuni Hotta, Mina Okochi, Hiroyuki Honda: Effect of Vascular Formed Endothelial Cell Network on the Invasive Capacity of Melanoma Using the *In Vitro* 3D Co-Culture Patterning Model. *PLoS One*, 9(7):e103502, 2014

3. **Shuhei Yamamoto**, Mina Okochi, Kowichi Jimbow, Hiroyuki Honda: Three-dimensional Magnetic Cell Array for Evaluation of Anti-proliferative Effects of Chemo-thermo Treatment on Cancer Spheroids. *Biotechnology and Bioprocess Engineering*, 20(3): 488-497, 2015

4. **Shuhei Yamamoto**, Jiahui Fei, Mina Okochi, Kazunori Shimizu, Akiko Yusa, Naoto Kondo, Hiroji Iwata, Hayao Nakanishi, Hiroyuki Honda: Efficient capturing of circulating tumor cells using a magnetic capture column and a size-selective filter. *Bioprocess and Biosystem Engineering*, 38(9):1693-1704. (2015)

Other publications

1. Akiko Yusa, Makoto Toneri, Taisuke Masuda, Seiji Ito, **Shuhei Yamamoto**, Mina Okochi, Naoto Kondo, Hiroji Iwata, Yasushi Yatabe, Yoshiyuki Ichinosawa, Seichin Kinuta, Eisaku Kondo, Hiroyuki Honda, Fumihito Arai, Hayao Nakanishi: Development of a New Rapid Isolation Device for Circulating Tumor Cells (CTCs) using 3D Palladium Filter and its Application for Genetic Analysis. *PLoS One*, 9(2), e88821, 2014

Books and Reviews

1. 山本修平,大河内美奈,本多裕之: 磁性粒子を使った細胞工学～細胞機能評価への応用～, 日本磁気学会誌まぐね 10 巻 3 号, 2015

Conferences

International 8 times, Domestic 23 times

(The international conferences related this thesis are described below)

1. Hiroyuki Honda, **Syuhei Yamamoto**, Mina Okochi, Kowichi Jimbow: Three-dimensional cell culture array using magnetic force-based cell patterning for analysis of the competitive effect of NPrCAP and heat treatments on B16F1 melanoma, *The 11th International Congress of Hyperthermic Oncology & The 29th Japanese Congress of Thermal Medicine*, Kyoto, Japan, August 28-31, p. 175, 2012 (Poster)
2. **Shuhei Yamamoto**, Mina Okochi, Hiroyuki Honda, Kowichi Jimbow: ANALYSIS OF THE CHEMO-THERMO SENSITIVITY ON B16F1 MELANOMA IN THREE-DIMENSIONAL CELL CULTURE ARRAY USING MAGNETIC FORCE-BASED CELL PATTERNING, *International Joint Symposium on Single-Cell Analysis*, Kyoto, Japan, November 27-28, p. 113, 2012 (Poster)
3. **Shuhei Yamamoto**, Mina Okochi, Hiroyuki Honda: Magnetic force-based 3D cell patterning for observation of invasive capacity of cancer cells co-cultured with vascular endothelial cell network, *The 20th Symposium of Young Asian Biochemical Engineers' Community*, Chiayi, Taiwan, November 6-8, p. 147, 2014 (Poster)
4. **Shuhei Yamamoto**, Mina Okochi, Hiroyuki Honda: Effect on invasive capacity of cancer cell spheroid co-cultured with vascular endothelial cell network using *in vitro* 3D

patterning model, *Micro and Nanotechnology in Medicine Conference 2014*, Turtle Bay, Hawaii, USA, December 8-12, p. 79, 2014 (Poster)

5. Kazunori Shimizu, **Shuhei Yamamoto**, Mina Okochi, Hiroyuki Honda: Magnetic Micropatterning of Different Types of Cells for Analyzing Their Interactions, *BMES 2015 (Annual Meeting of Biomedical Engineering Society)*, Tampa, Florida, USA, October 7-10, p.121, 2015 (Poster)
6. **Shuhei Yamamoto**, Kazunori Shimizu, Mina Okochi, Hiroyuki Honda: Magnetic Force-based Cellular Micropatterning for Analysis of Cell-cell Interactions, *Asian Congress on Biotechnology 2015*, Kuala Lumpur, Malaysia, November 15-19, p. 124, 2015 (Oral)
7. **Shuhei Yamamoto**, Jiahui Fei, Mina Okochi, Kazunori Shimizu, Akiko Yusa, Naoto Kondo, Hiroji Iwata, Hayao Nakanishi, Hiroyuki Honda: Efficient Capturing of Circulating Tumor Cells (CTCs) Using a Combined Method of a Size-selective Filter and a Magnetic Capture Column, *Asian Congress on Biotechnology 2015*, Kuala Lumpur, Malaysia, November 15-19, p.134, 2015 (Oral)
8. Mina Okochi, **Shuhei Yamamoto**, Hiroyuki Honda: In vitro 3D co-culture patterning model for evaluation of tumor cell malignancy, *The international chemical congress of pacific basin societies 2015*, Honolulu, Hawaii, USA, December 15-20, p.227, 2015 (Oral)

Award

1. 化学工学会 第 45 回秋期大会 バイオ部会優秀ポスター賞, 「磁気細胞パターニング法を用いたがん細胞の薬剤応答評価法の構築」, 岡山, 2013 年 9 月
2. 平成 26 年度 IGER 異分野融合研究コンテスト優秀賞「植物細胞による物質高生産のための培養生産技術の開発」, 愛知, 2014 年 9 月
3. IGER Annual Meeting 2014 Poster Award, 「*In vitro* co-culture model using magnetic force-based 3D cell patterning method for observation of invasive capacity of cancer cells to vascular endothelial cell network」, Aichi, 2015 年 1 月
4. IGER Annual Meeting 2015 Poster Award, 「Magnetic and size-selective separation for efficient capturing of circulating tumor cells (CTCs)」, Aichi, 2016 年 1 月

Acknowledgments

This study has been carried out in Bioprocess Engineering laboratory, Department of Biotechnology, Graduate School of Engineering, Nagoya University, Japan.

First of all, the author expresses his sincerest gratitude to his supervisor, Professor HONDA Hiroyuki, Department of Biotechnology, Graduate School of Engineering, Nagoya University, for his supreme leading, support and assistance for this research and his human empathy. The author has been received constant and warm encouragement from Professor HONDA and also has been given many opportunities to grow as a researcher by Professor HONDA.

The author expresses deep gratefulness to Professor NAKANO Hideo, Department of Bioengineering Sciences, Graduate School of Bioagricultural Science, Nagoya University, Professor IIJIMA Shinji, and Associate Professor SHIMIZU Kazunori, Department of Biotechnology, Graduate School of Engineering, Nagoya University, for their precise leading and a multiplicity of their thoughtful advises and encouragements. This research could never be completed without their helpful suggestions.

The author also expresses their gratitude to Professor OKOCHI Mina, Department of Chemical Engineering, Graduate School of Science and Engineering, Tokyo Institute of Technology, and Associate Professor KATO Ryuji and Assistant Professor KANIE Kei,

Department of Basic Medicinal Science, Graduate School of Pharmaceutical Sciences, Nagoya University, for many invaluable advices.

The author would like to express his gratitude to Professor NAKANISHI Hayao, Division of Oncological Pathology, Aichi Cancer Center Research Institute, for his grateful supporting of the animal experiments in Chapters 5 and 6.

The author appreciates deeply to the members of “nano” and “device” teams, Mr. KOIKE Shinji, Mr. MATSUMURA Taku, Mr. SAKAI Yuki, Ms. TESHIMA Midori, Ms. ARAI Sayuri, Mr. KAMIYA Tomohiro, Mr. NIWA Kousuke, Ms. UOI Sayaka, Mr. KOJIMA Reiji, Ms. FEI Jiahui, Mr. IMAIZUMI Yu, Ms. GENMA Riho, Mr. GOTO Yuki, and Ms. SAKIKAWA Chiho, and to all the members of Bioprocess Engineering laboratory for their creative discussions, warmhearted assistance, and valuable friendships. Especially, the author thanks to Dr. USHIDA Yasunori, Dr. SUGITA Tomoya and Dr. SASAKI Hiroto for their precise leading, thoughtful advises and many encouragements, in addition to sharing precious experiences and time in the laboratory together.

Finally, the author expresses the deepest appreciation to his parents, his family members, and all of people who have supported his life for devoting everything through the doctor course.

January, 2016, YAMAMOTO Shuhei